Coupled System Identification, Flight Controller Design, and Wind Sensing Using KHawk Flying-Wing UAS

Harold Patrick Flanagan

Submitted to the graduate degree program in Department of Aerospace Engineering and the Graduate Faculty of the University of Kansas in partial fulfillment of the requirements for the degree of Doctor of Philosophy comprehensive exam.

Committee members

Haiyang Chao, Chairperson

Craig McLaughlin, Member

Shawn Keshmiri, Member

Zhongquan Zheng, Member

Huazhen Fang, Member

Date defended:

The Dissertation Committee for Harold Patrick Flanagan certifies
that this is the approved version of the following dissertation :

Coupled System Identification, Flight Controller Design, and Wind Sensing Using KHawk Flying-Wing UAS

Haiyang Chao, Chairperson

Date approved: _____

Abstract

This dissertation focuses on new system and method development using KHawk flying-wing unmanned aircraft system (UAS) for system identification, controller design, and wind sensing applications. This dissertation attempts to provide a start to finish example for how to build and modify a low-cost remote controlled (R/C) aircraft for UAS research purposes, perform system identification to determine the dynamic aircraft model, design a robust lateral loop flight controller for disturbance rejection, estimate flow angles for stall detection, and measure wind data including both prevailing wind and turbulence. First, new design, building, and flight test procedures are provided for KHawk flying-wing UAS family including a series of small, low-cost, and durable UAS that can support atmospheric and aerospace researches. Next, a coupled system identification and robust controller design method is examined for the lateral loop of KHawk flying-wing UAS. A fractional order PID (FOPID) controller is also introduced and optimized for turbulence rejection using a genetic algorithm based multi-objective optimization approach. Then, a new stall detection method is introduced using a complimentary filter to determine the inertial angle of attack (AOA) of the UAS together with flight analysis of typical stall patterns of small flying-wing UAS. And finally, the developed KHawk flying wing UAS is used for prevailing wind and turbulence measurement while flying over a prescribed fire.

Acknowledgements

I would like to first thank my Ph.D. advisor Dr. Haiyang Chao for his guidance, knowledge, and great patience with me during this journey. Dr. Haiyang Chao's acceptance of me into this research program at the KU CUSL Lab has given me invaluable experience I plan to use for the rest of my life as an aerospace researcher and engineer. Furthermore, I would like to thank my committee members, Dr. Craig McLaughlin, Dr. Zhongquan Zheng, Dr. Shawn Keshmiri, and Dr. Huazhen Fang, for their inspiration and advice through my research period at KU.

I would like to thank my colleagues, collaborators, and fellow authors, Steven G. Hagerott, Dr. Pengzhi Tian, Saket Gowravaram, Jackson Hugh Goyer, and Justin Matt, for their assistance and support. Without this excellent team of colleges and collaborators, the research presented in this dissertation would not be possible. I would also like to thank all my friends I met through KU for their support in research, spirit, and encouragement throughout the years.

Research grants used for this research presented in this dissertation include the University of Kansas General Research Fund allocation 2221800 and USDA-NIFA Grant 2019-67021-28992, and NASA grant NNX14AF55A.

Finally, I would like to thank my loving family that has supported me through this time with their endless support and love. With all my love, thank you Mom and Dad.

Contents

List of Figures

List of Tables

Chapter 1

Introduction

1.1 Background and Motivation

In recent years, unmanned aircraft systems (UAS) have been increasingly used in challenging missions such as urban package delivery and disaster in-situ and remote sensing. However, it is very challenging to develop smart UAS to operate safely, efficiently, and robustly in these dynamically changing flow fields, partially due to the lack of high accuracy UAS dynamic models, intelligent sensing and estimation algorithms, and smart flight controllers.

Small remote controlled (R/C) aircraft provide cheap and useful test beds that can be easily purchased, built, modified, and flown by experienced or inexperienced R/C pilots. The availability and modifiability of these small R/C aircraft make them a popular choice for researchers across the globe. However, since small R/C aircraft are made predominantly by hobby enthusiasts and not for research purposes, small R/C aircraft generally do not have accurate dynamic models or instructions regarding how to tune the on-board flight controller. This means researchers will have to determine the dynamic models of their modified R/C aircraft and tune their controllers either though manual or theoretical means. Developing procedures for determining the dynamic models and tuning parameters for these small R/C aircraft could help researchers create safer UAS that can handle challenging environments such as disaster sites or urban environments where wind and turbulence are major flight risks. Multiple methods exist for determining the dynamic models of aircraft and for tuning their controllers. Methods for determining the dynamic models of aircraft range from wind tunnel testing based methods, to more advanced computational methods such as computational fluid dynamics (CFD). Controller tuning for classical proportional integral deriva-

tive (PID) controllers can likewise be determined through different means. This includes: manual tuning, Ziegler-Nichols method, genetic algorithms, and many more. The research presented in this dissertation attempts to develop a new procedure for modifying and developing a small UAS from R/C aircraft. This dissertation also provides new methods/algorithms and validations for sensing, estimation, system identification, and control of small UAS, including inertial angle of attack estimation for UAS stall/spin identification, UAS based fire wind sensing, coupled lateral loop system identification and controller design, and fractional order lateral controller design.

The motivations of this dissertation include:

- It is challenging to build or modify a low-cost R/C aircraft for research purposes that is durable and robust to handle payload and mission requirements.
- Low-cost UAS generally do not have known or comparable system dynamic models that can be used for controller design. Since low-cost UAS will be increasingly used in more dangerous air flow environments, the need for more robust and mission specific controllers are needed for safe UAS flight operations.
- Wind velocity profiles are also important to safe UAS flight since turbulence generated in challenging environments could results in loss of control or even destruction of the UAS. Methods for the identification of stall/spin are particularly important since stall/spins are a common issue for small UAS and little is studied regarding the mitigation of stall/spin for small UAS.

1.2 Main Contributions

The main contributions of this dissertation include:

1. Introduction of the KHawk UAS building procedure with instructions on how to modify a low-cost flying-wing UAS and create a research grade UAS based on mission specific research goals. The developed procedure can be used on a variety of small UAS for different research purposes.

2. Introduction of a new method for coupled lateral system identification and controller tuning of a small flying-wing UAS using a tuning rule based on multiple time and frequency domain control specifications. A low-cost method is introduced using widely available software and simple flight identification techniques to create a lateral dynamic model of a small UAS and robust controller for turbulence rejection. The proposed method can be easily adopted to system identification and controller design of other low-cost R/C aircraft.

3. Introduction and demonstration of a new genetic algorithm optimized fractional order controller (FOC) design for the lateral open loop dynamics of a flying-wing UAS. The FOC design is based on the classical PID controller structure with the addition of a fractional derivative (D) and fractional integral (I) component. This method allows for more manipulation of the controller design space and better closed loop controller performance. A genetic algorithm is used to determine optimized controller gains for different scenarios based on a user defined cost function.

4. A new stall detection algorithm based on inertial angle of attack estimated from inertial and air speed sensors together with detailed analysis of typical stall data for a flying-wing UAS. A complimentary filter is proposed to determine the inertial angle of attack (AOA) of a UAS during stall/spins scenarios. This method can be applied to other UAS with known coefficient of lift parameters.

5. Sensing and estimation of typical wind and turbulence generated by a prescribed fire using small UAS. Both UAS measured wind data and ground weather station wind measurements are compared including prevailing wind and turbulence (turbulent kinetic energy). The measured wind information and UAS response data create a foundation for future UAS employments in these challenging fire environments.

1.3 Dissertation Organization

Chapter 2 introduces the design of the KHawk UAS families including KHawk 55 UAS, KHawk 55 Stereo Vision UAS, KHawk Thermal Vision UAS, and KHawk Zephyr 3 UAS. Chapter 3 provides a new methodology for coupled system identification and lateral controller design for a small flying-wing UAS. Chapter 4 provides design and analysis of a fractional order controller for the lateral loop of a flying-wing UAS. Chapter 5 discusses the development of a complementary filter for angle of attack estimation which is used for stall/spin detection of a flying-wing UAS. Chapter 6 discusses UAS based fire wind sensing and reconstruction. Chapter 7 is the conclusion of the dissertation and discussion of future research.

Chapter 2

KHawk Flying-Wing UAS Platform

Abstract

A series of KHawk flying-wing UAS were designed, built, and flight tested to support different research topics including wind sensing, disaster remote sensing, aircraft system identification, and flight controller design. This chapter focuses on the general design and tuning procedure for the KHawk flying-wing UAS family as well as the specific design considerations for each UAS. The developed KHawk flying-wing UAS family include the KHawk 55, KHawk 55 Stereo Vision, KHawk Thermal Vision, and KHawk Zephyr 3. Finally, the obtained airborne data showed the effectiveness of the developed KHawk flying-wing UAS.

2.1 KHawk Flying-Wing UAS family

The KHawk flying-wing UAS family have been designed for different mission specific purposes ranging from aircraft guidance, navigation, and control, to disaster in-situ and remote sensing. The KHawk flying-wing UAS family were designed around several specific requirements:

1. The UAS needs to support both manual and autonomous research flights with associated sensing payloads. The UAS platform needs to be stable, repeatable, and robust to support scientific missions such as aircraft system identification and wind sensing.
2. Variations of the UAS can be created to support different payloads for various missions such as cameras for remote sensing and multi-hole probes for aerodynamic research and wind sensing.

3. The UAS should be low-cost and easy to maintain and operate.
4. The UAS should be able to handle challenging flight environments involving high winds (e.g. up to 15 mph prevailing wind), turbulence, and prescribed fires.

A total of four KHawk flying-wing UAS are discussed in this chapter and can be described as follows for their mission specific purposes:

1. The KHawk 55 UAS is the first iteration of the KHawk 55 UAS line and is the baseline model for the KHawk flying-wing family. The KHawk 55 UAS is used for stall/spin detection, AOA estimation, system identification, simulation validation, and controller design.
2. The KHawk 55 Stereo Vision UAS was created to accommodate two stereo vision cameras used for GPS-denied navigation. One major design requirement of the KHawk 55 Stereo Vision UAS is that the cameras need to remain as rigid as possible so that position and orientation of the cameras remained the same during the flight.
3. The KHawk Thermal Vision UAS was built around two cameras, one near infrared (NIR) and one thermal infrared for detection of fires. The UAS must also be able to carry the standard sensing suite (IMU/GPS) and a 5-hole probe for wind velocity measurement while flying around and above fires.
4. The KHawk Zephyr 3 UAS was created for disaster remote sensing missions with the addition of two modified GoPro cameras, one RGB and one NIR. It has been deployed multiple times for remote sensing over crop fields with hail damage and tornado damage.

2.2 UAS Airframes and Autopilots

2.2.1 UAS Airframe

A typical UAS used for research is either constructed from an off-the-shelf R/C aircraft kit or made from scratch. The basic construction and components of a UAS can be described as follows:

1. Airframe. The most common materials used for airframe are foam, wood, composites, and plastics.
2. Autopilot. An autopilot is used to perform autonomous flight.
3. Control surface. Ailerons, elevators, rudder, and/or elevons are usually used to control the orientation of the aircraft. The actuation of control surface can be performed by using a servo motor connected to a pushrod or a pull-pull cable.
4. Propulsion. Electric propulsion motors are most commonly used for small UAS but occasionally gas powered motors are used for larger UAS. The motor drives a propeller in either a pusher or puller configuration. An electronic speed controller (ESC) is needed to moderate the electricity and control the speed of the propulsion motor
5. R/C receiver. The R/C receiver collects information from the R/C transmitter and sends information to the autopilot.
6. Fuel. Batteries or some form of gas is usually used to power the aircraft.

2.2.2 UAS Autopilot

Autopilots for small UAS contain several major components and perform several functions necessary for manual and autonomous flight. The main components and functions of a small UAS are:

1. Sensing. Components related to sensing include accelerometers, gyros, magnetometers, Pitot tube, pressure sensor and GPS receiver.
2. Computation. A microcomputer capable of computing, processing, and storing the data.
3. Actuation. Servos and propulsion motor are used to actuate the controller surfaces and the engine.
4. Communication. RC transmitter and receiver are mostly needed for the safety link. For the data link, a pair of data modems are usually used to send orders and information back and forth between the aircraft and the ground station.

Two representative UAS autopilots are introduced briefly in the following sections.

2.2.2.1 Paparazzi Autopilot

The Paparazzi autopilot is an open-source UAS autopilot and can be used in unison with different hardware components and can also be modified using its open-source software. It is one of the main autopilots used in this dissertation since it is easily modifiable. Our customized Paparazzi Autopilot consists of the Paparazzi TWOG autopilot, Microstrain GX3 IMU, GumStix computer, Ublox LEA-6H GPS receiver, and a Digi 900 MHz modem to deliver the information to a ground station computer [2]. The ground control station (GCS) is used to deliver commands to the aircraft which can include way point changes, controller gain changes, and flight commands such as altitude changes or return to base. The GCS can also record certain parameters from the aircraft such as altitude, attitude, and controller commands. The Paparazzi autopilot is used for telemetry and control command generation of the KHawk 55 UAS and KHawk 55 Stereo Vision UAS.

2.2.2.2 Pixhawk Autopilot

The Pixhawk autopilot is another open source autopilot that can be easily used by researchers and hobbyists for a variety of different purposes. The Pixhawk autopilot contains its own integrated computer, sensors, data storage, and associated IOs. The Pixhawk firmware can also be easily updated and modified through the use of the open source ArduPilot software suite. ArduPilot also comes with a large support base of researchers and scientists across the world who are constantly updating and modifying the open source ArduPilot software. The Pixhawk autopilot is used on both the KHawk Thermal Vision UAS and KHawk Zephyr 3 UAS.

2.3 Design and Building Procedure for the KHawk Flying-Wing UAS

This section will discuss the design and building procedure for the KHawk flying-wing UAS. The KHawk 55 UAS is used as the main example. Similar design and building modifications are also

used on the other UAS mentioned in this chapter as the KHawk 55 UAS is commonly used as a test bed for different equipment and flight testing.

2.3.1 KHawk 55 UAS

The KHawk 55 UAS supports both manual remote controlled (RC) mode and autonomous mode. The airborne avionics includes a Microstrain GX3 IMU (specifications are shown Table 2.3), Paparazzi autopilot, a u-blox Lea-6H GPS receiver, a Digi Xtend 900 MHz data modem, a Gumstix computer, and an air data system. One of the two optional air data systems can be installed for air flow measurements including one low-cost Eagle Tree airspeed system (air speed only), and one Aeroprobe 5-hole air data system (airspeed, AOA, and AOS). The 5-hole pitot-tube setup is shown on the left of Fig. 2.2 with the EagleTree and custom 3D printed mount on the right. All the sensor data is logged onboard the aircraft including inertial data (100Hz), GPS data (4 Hz), air flow data (10Hz for EagleTree sensor or 100 Hz for Aeroprobe sensor). Detailed specifications of the 5-hole pitot-tube and Eagle Tree pitot-tube are shown in Table 2.2. It is worth mentioning that the Aeroprobe 5-hole pitot-tube has an airspeed range of 8-45 m/s and AOA/AOS range of $\pm$ 20 degrees. In other words, the Aeroprobe pitot-tube will not report a meaningful value when operating outside of the calibrated range.

Table 2.1: KHawk 55 UAS specifications

UAS Parameter	**Specifications**
Take-off Weight	~5.5 to 6.7 lbs
Max Payload	up to 1 lb
Material	EPO Foam, Carbon Spar
Wingspan	55 inches
Control Mode	Elevons
Engine	Pusher Brushless Motor
Endurance	~45 minutes
Cruise Speed	18 m/s
Take-off	Bungee

Figure 2.1: The CUSL KHawk 55 UAS (top) and KHawk Thermal Vision UAS (bottom).

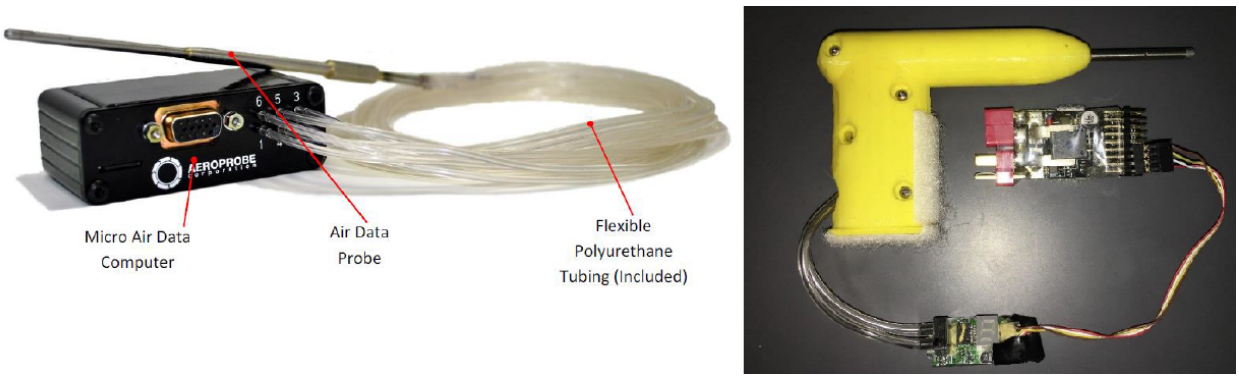

Figure 2.2: 5-hole Aeroprobe (left) and EagleTree Probe (right).

Table 2.2: Specifications for KHawk 55 air data systems

UAS Parameter	EagleTree Specifications	Aeroprobe Specifications
Measurements	V_a	$V_a/\alpha/\beta$
Max Update Rate	50 Hz	100 Hz
Physical Interface	SPI	Serial
Airspeed Range	9~350 MPH (4~156 m/s)	8~45 m/s
Airspeed Accuracy	N/A	1 m/s
Airspeed Resolution	1 MPH (0.45 m/s)	0.25 m/s
α/β Range	N/A	-20° ~20°
α/β Accuracy	N/A	1°
α/β Resolution	N/A	0.1°

Table 2.3: Microstrain GX3 IMU specifications

Parameter	**Meas. Range**	**Non-linearity**	**Init. Bias Error**	**Noise Den.**	**Data Output Rate**
Accelerometer	±5 g (standard)	±0.1% fs	±0.002 g	$80\mu g/\sqrt{Hz}$	1 ~1000 Hz
Gyroscope	±300°/sec (standard)	±0.03% fs	±0.25°/sec	$0.03^\circ/\text{sec}/\sqrt{Hz}$	1 ~1000 Hz
Magnetometer	±1.25 Gauss	±0.4% fs	±0.003 Gauss	100 μGauss/$\sqrt{Hz}$	1 ~1000 Hz
Parameter	**Heading Range**	**Static Accuracy**	**Dynamic Accuracy**	**Resolution**	**Data Output Rate**
Attitude	360°	±0.5°	±2°	$< 0.01^\circ$	1 ~500 Hz

2.3.2 Building Procedure

This section will discuss the design and building procedure for the KHawk 55 UAS. Similar approaches are also used on the other UAS mentioned in this chapter. The entire building procedure and all modifications can be found in the CUSL's KHawk 55 building procedure [3]. The main modifications regarding the design and building consideration of the KHawk 55 UAS will be discussed here briefly. The KHawk 55 UAS is built from a RiteWing Zephyr 2 flying-wing kit and modified to carry any supporting payload. The design procedure can be described as follows:

1. Determine the UAS specifications including payload, endurance, and desired flight speed.
2. Select the payload location based on equipment size, sensing performance, and best location for CG.
3. Determine the best autopilot for mission requirements, GPS receiver, and communication system (R/C receiver, and ground station hardware).

4. Select aircraft actuation and motor. This includes the thrust motor, electric speed controller (ESC), batteries, and servos.

Once the basic design considerations have been determined, the UAS building and testing procedures are as follows:

1. The UAS structural rigidity and strength should meet requirements for mission specific requirements. The rigidity of the UAS should be strong enough so that interaction between the autopilot and UAS do not cause flutter during flight.
2. The actuator and controller surfaces should be able to handle repeatable use and temperature variations. If the actuator/control surface of the aircraft fails, the destruction of the UAS will likely occur in an uncontrollable manner.
3. Servos and motor components should be secured using multiple back-up methods for safety (multiple hinges and reinforced joints using wood and composites), and to insure minimal vibration from outside influences including wind.
4. Avionics and their configuration should be checked to confirm consistent reliability.
5. The CG should be placed following factory recommendations and be checked through ground testing before flight.
6. All systems should be checked in unison to confirm UAS flight worthiness.

The first step of UAS building is to join the wings of the aircraft together using the carbon spars provided and fiberglass to reinforce the wing shown in Fig. 2.3. Once the wings have been joined, a tow hook is mounted beneath the aircraft in front of the center of gravity by about 4 inches from the leading edge, which is selected for structural strength in front of the CG. Positioning the tow hook in front of the CG is necessary for launch stability. The second step is to install the control surfaces for the UAS. The ailerons are attached using pivot hinges for the KHawk 55 UAS, this is to create a secure elevon attachment that is repeatable, and the engine mount is created using sheet metal which is riveted together. The assembled piece is then epoxied into rear engine location on the wing shown in Fig. 2.4.

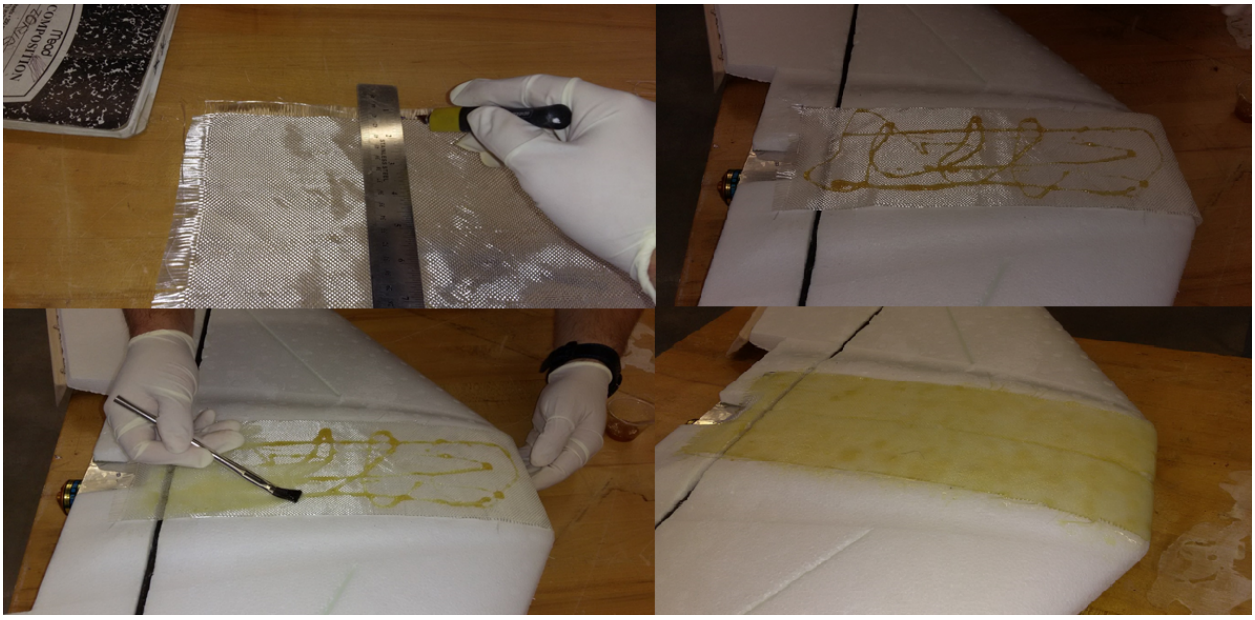

Figure 2.3: Fiberglassing the wing.

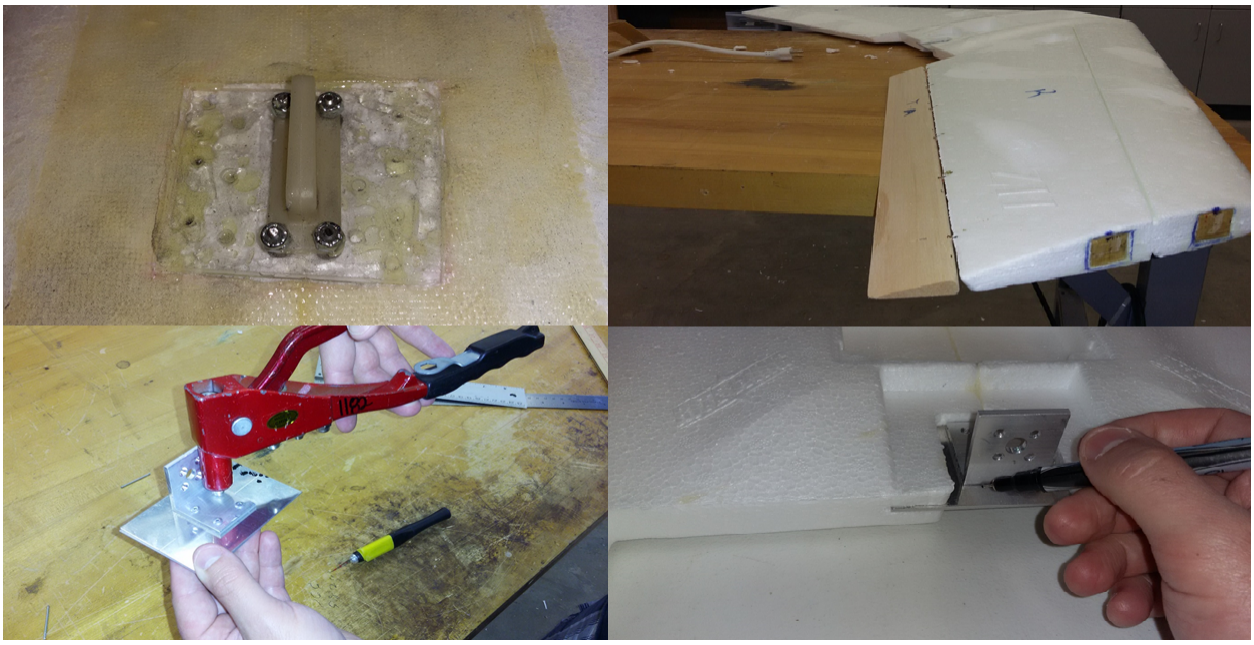

Figure 2.4: Mounting different components.

The third step is to install the servos. Typical servo mounting locations for small UAS are preselected by the factory for a standard servo size for the UAS. If no location is preselected, the position for mounting the servo should be in a structurally strong place on the aircraft, and should provide the majority of its power and torque where the maximum forces on the aileron/ele-

vator/rudder/elevon are applied. The servo mounting location for the RiteWing Zephyr 2 is pre-cut from the factory and the servo is mounted near the center of the aircraft. Fig. 2.5 shows the servo mounted onto plywood that is inserted into the wing with epoxy, and the metal pushrod with a carbon tube glued over the metal rod for more rigidity and strength. The glue is simply used to keep the carbon tube in place over the metal rod to avoid it from moving or vibrating during flight.

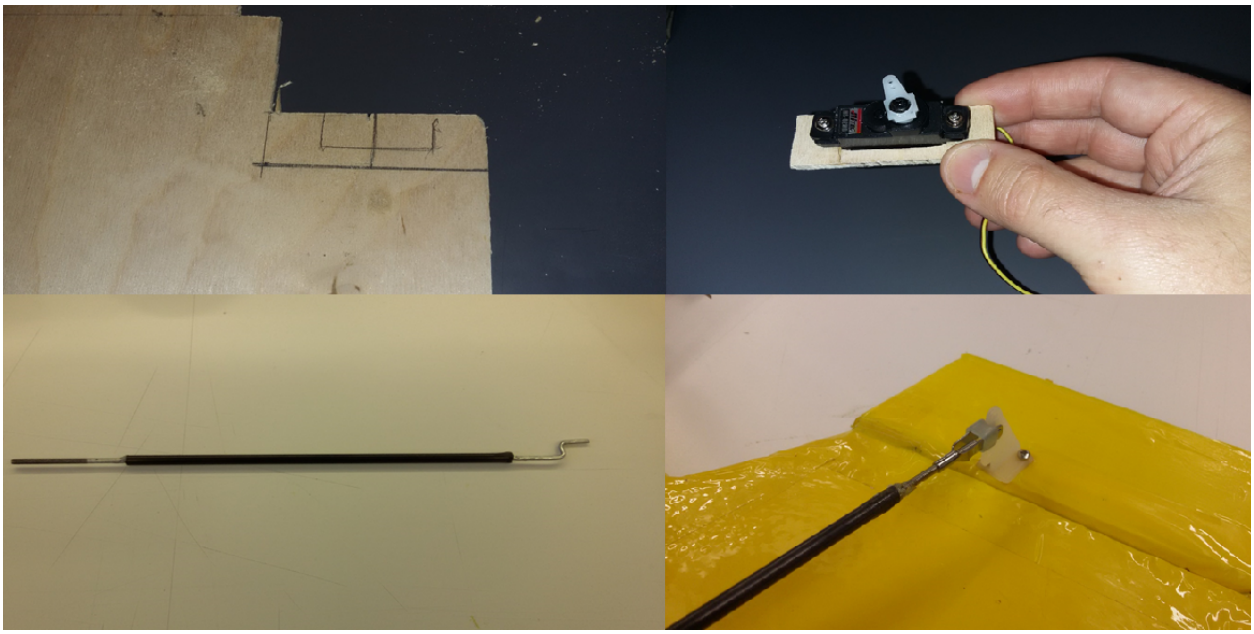

Figure 2.5: Servo mounting and pushrod assembly.

The fourth step is to install the avionics. The avionics configuration is selected to provide the mission specific data for the UAS, and placement of each component is key for the proper data acquisition. Installation of the IMU should be as close to the CG as possible and along body axis lines. In the case of the Pixhawk autopilot, the Pixhawk autopilot should be placed at the CG and along body axis lines since it contains an integrated IMU. The modem antenna should be placed in a location away from any electronics that could cause interference and in a position that can be accessed by the ground station no matter what orientation the aircraft is in. The modem antenna is usually attached to the wingtip. The GPS receiver should also be placed in a location with minimal interference.

The fifth step is to check the CG of the UAS. Fig. 2.6 shows the process of laying out all the

parts on the aircraft so that the CG location is correct and the process of cutting out and tacking the equipment into place before covering. Next, the wing is covered in MonoKote by starting at the extremities of the wing and working towards the center with an iron or heat gun to apply the MonoKote neatly over the wing. Lastly, the plane is given a final CG test by placing it on a CG apparatus so that it can be adjusted using small lead weights and made safe for flight.

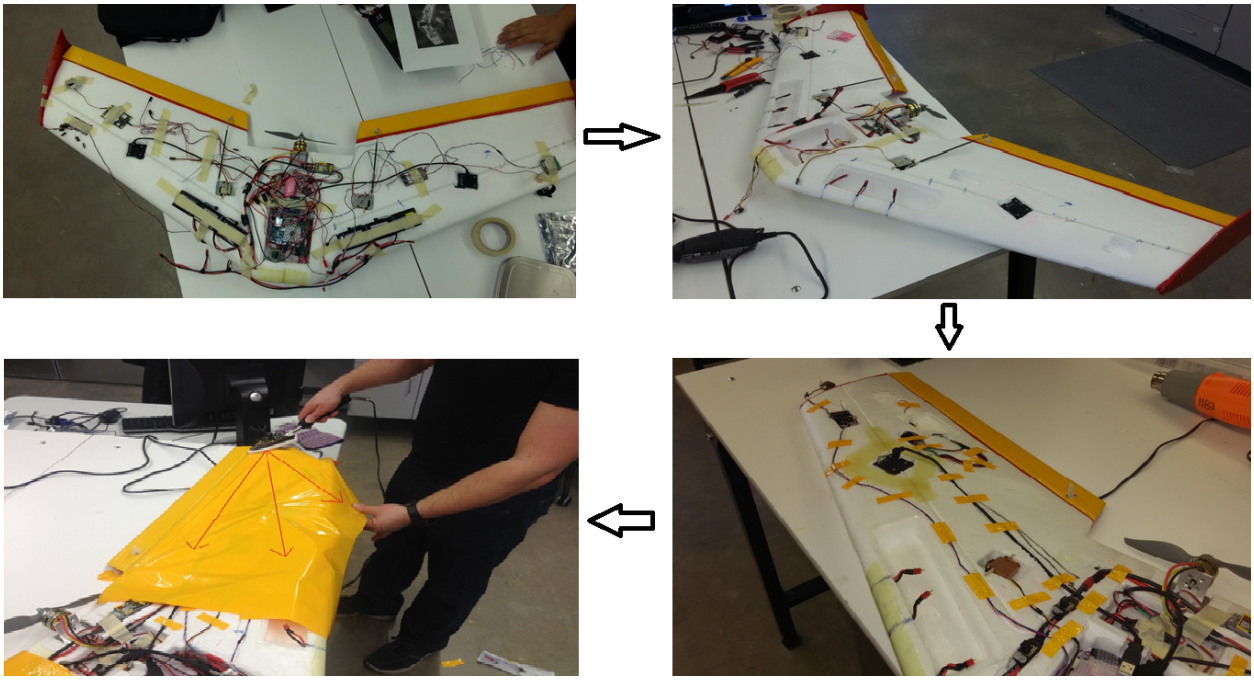

Figure 2.6: Cutting out equipment locations and covering.

The last step is to configure the avionics for the ground test and flight test. R/C receiver binding and a final avionics check should be performed to insure the correct calibration of all components including the correct directional movement of the servos and proper ESC calibration. ESC calibration is necessary so that the RPM, voltage, and amperage of the motor can be analyzed post flight so the thrust can be calculated and any motor issues can be troubleshooted. ESC calibrations should be performed prior to flight and should be done as per the ESC and electric motor's manual. The orientation and position of the aircraft should also be checked pre-flight to confirm reasonable IMU and GPS accuracy, and the data link between the ground station and R/C receiver should also be checked for proper communication range over the specified communication radius.

The building procedures discussed in this section are used on the other aircraft mentioned in

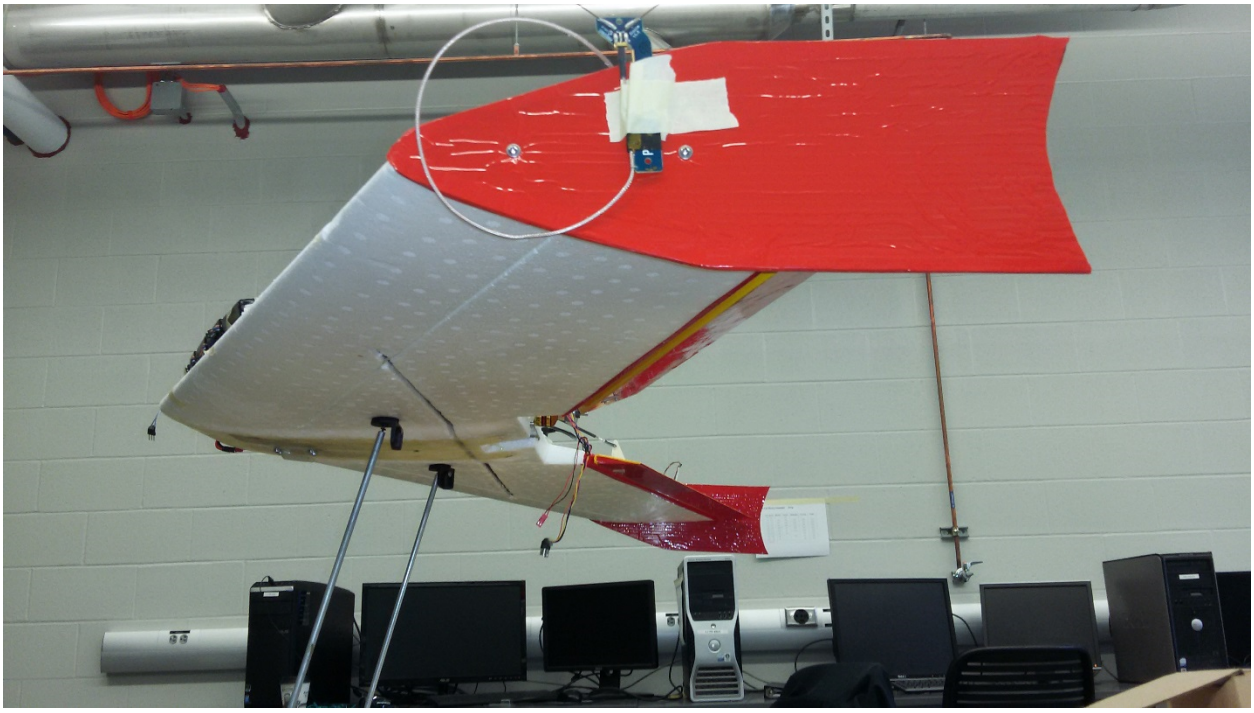

Figure 2.7: Final CG test.

this chapter, and are considered to be the standard for small flying-wing UAS building procedures by the CUSL lab.

2.3.3 KHawk Zephyr 3

The KHawk Zephyr 3 (shown in Fig. 2.8) is a different platform built from the RiteWing Zephyr 3 kit, and was created to use and test the Pixhawk controller for the KHawk UAS fleet and for the purpose of remote sensing. The KHawk Zephyr 3 UAS is also a flying-wing UAS with a smaller airframe, lighter payload capabilities, and shorter range. The main sensing payload for the KHawk Zephyr 3 are two modified Peau GoPro cameras for including a red green blue (RGB) camera and near infrared (NIR) camera.

Figure 2.8: KHawk Zephyr 3 UAS (left) and the sensing cameras (right).

Table 2.4: KHawk Zephyr 3 specifications

UAS Parameter	**Specifications**
Take-off Weight	~4.1 lbs
Max Payload	1 lb
Material	EPO Foam, Square Carbon Spar Reinforcement
Wingspan	47 inches
Control Mode	Elevons
Engine	Pusher Brushless Motor
Endurance	~30 minutes
Cruise Speed	16 m/s
Take-off	Bungee

2.4 Customized Payload Design and Integration

In addition to the main airframe, customized mounts are designed to support associated payloads on the KHawk 55 UAS, the KHawk Thermal Vision UAS, and the KHawk 55 Stereo Vision UAS.

2.4.1 KHawk 55 UAS 5-Hole Pitot Tube Mount and Sliding Camera Door

The main custom designed part for the KHawk 55 UAS and KHawk Thermal Vision UAS is the 5-hole pitot tube mount, which can be used on other KHawk UAS. The 5-hole pitot tube mount was designed using SolidWorks and created using a 3D printer. The assembled version of the 5-hole pitot tube mount design is shown in Fig. 2.9 and the disassembled version is shown in Fig. 2.10. The 5-hole pitot tube fits into the middle insert which orients it in its upright position. The insert

is then placed into the front of the mount until a snug fit is achieved, then the front insert is placed into the rear portion of the mount. The final printed version is shown in Fig. 2.11.

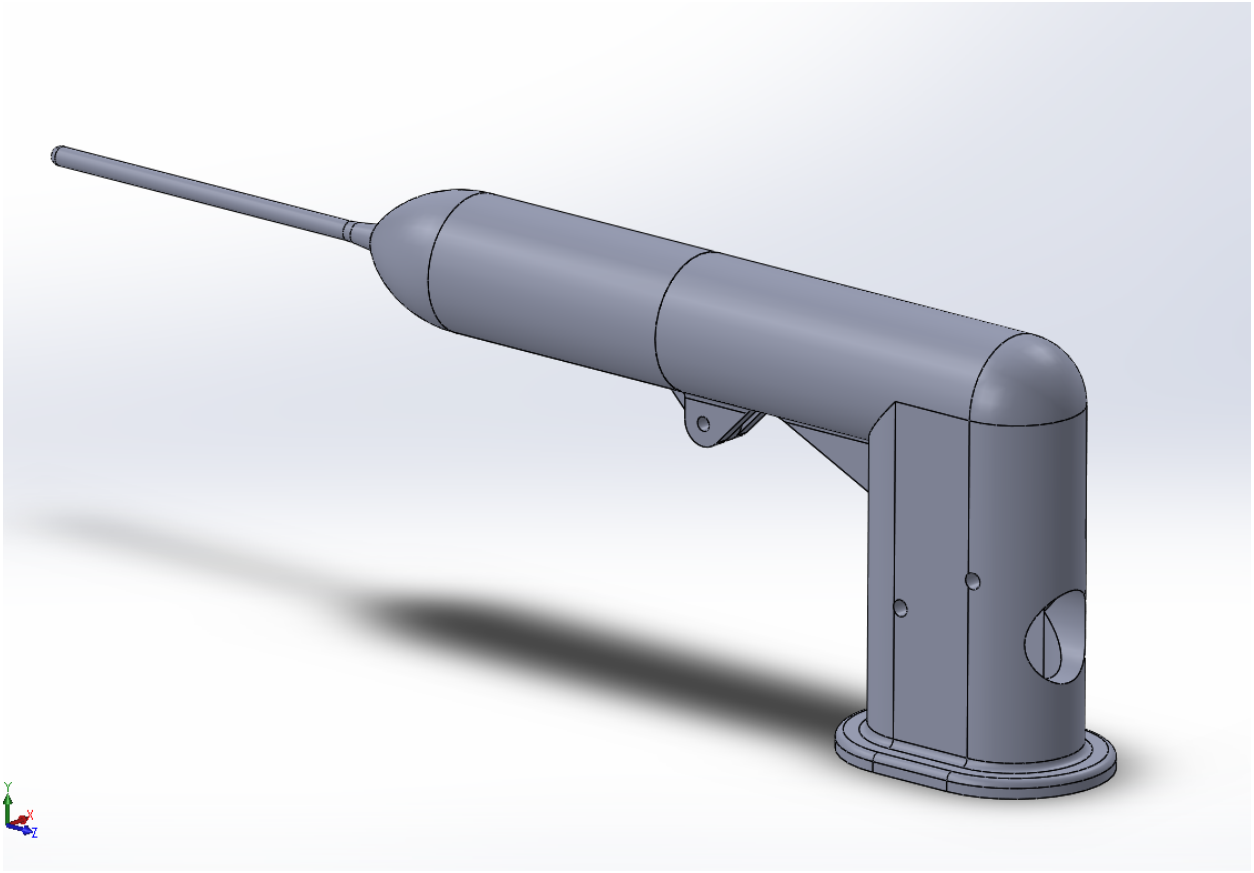

Figure 2.9: 5-hole probe mount assembled.

The KHawk Thermal Vision UAS (shown in Fig. 2.1) was created for the purpose of monitoring wildfires and wind measurements. The required payloads include a Pixhawk Cube autopilot, a GPS receiver, a FLIR Vue Pro R thermal camera, and a 5-hole pitot tube for airflow measurements. The building procedure for this aircraft is similar to the KHawk 55 UAS, with slight modifications to house the thermal camera including a sliding camera door to protect it during takeoff and landings. This sliding door is shown in Fig.2.12 and is constructed from fiberglass and is activated via a servo motor through the R/C link of the transmitter.

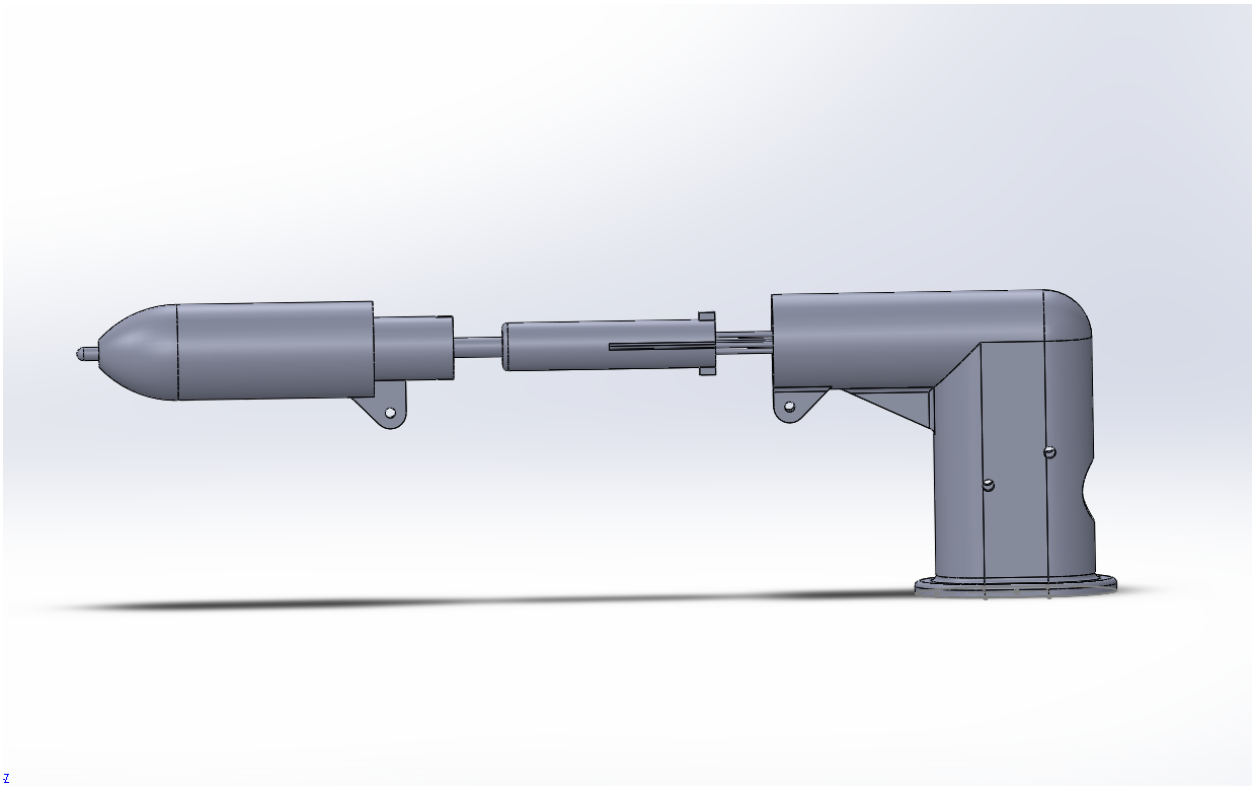

Figure 2.10: 5-hole probe mount disassembled.

Figure 2.11: 5-hole pitot tube mount fully assembled with 5-hole pitot tube installed.

Figure 2.12: Sliding door to protect the FLir Vue Pro R thermal vision camera.

2.4.2 KHawk 55 Stereo Vision Rigid Mounting System

The KHawk 55 stereo vision UAS was developed to support two stereo cameras in unison for GPS denied navigation. The design considerations for this aircraft included modifications to the air-frame structure for rigidity, and a 3D printed camera mount to insure proper placement of each camera for navigation purposes. The KHawk 55 Stereo Vision UAS uses the Paparazzi autopilot and same equipment as the KHawk 55 UAS with the addition of a NovAtel GPS receiver, and an ODROID computer for the purpose of image data acquisition and computation.

The major building modifications for the KHawk 55 Stereo Vision UAS involves the installation of the stereo vision cameras and the carbon mounting spar they are attached to. The fully assembled part is shown in Fig. 2.13 and the camera mount assembly is shown glued into the car-

bon spar shown in Fig. 2.14. The carbon spar used is a 3/4" inch square carbon spar that increases the rigidity of the wing and keeps the stereo vision cameras in alignment with the IMU so depth and distance calculations can be made. The carbon spar is mounted along the lateral direction of the aircraft through the CG location and is glued in place using epoxy. Fiberglass spars on both the top and bottom of the aircraft are cut for the camera installation and are reinforced using fiberglass strips, shown in Fig. 2.15.

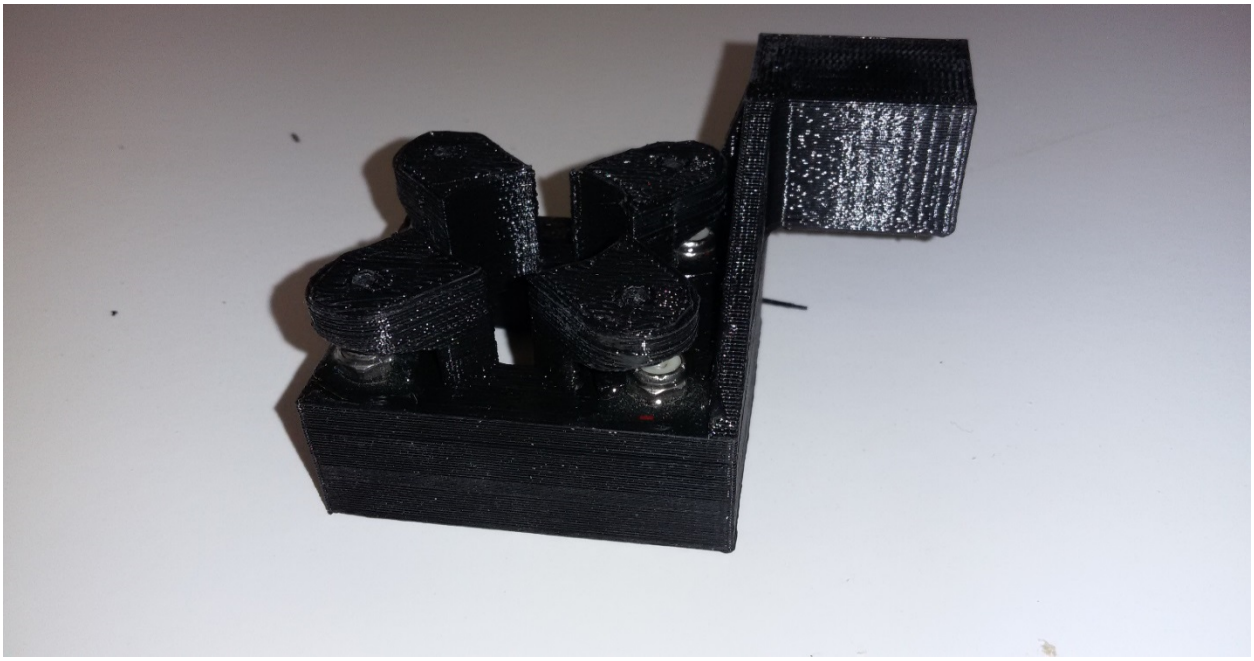

Figure 2.13: Assembled camera mount.

The KHawk 55 Stereo Vision UAS uses two stereo vision cameras which are housed inside of a 3D printed part that is meant to keep the camera position rigid and protected. A 3D assembly of the printed part is shown in Fig. 2.16. The assembly is then glued together with the top part being removable to access the camera inside and the bottom is glued onto the main middle part. The bottom portion has feet so a panel of glass can be screwed onto it for the purpose of camera lens protection.

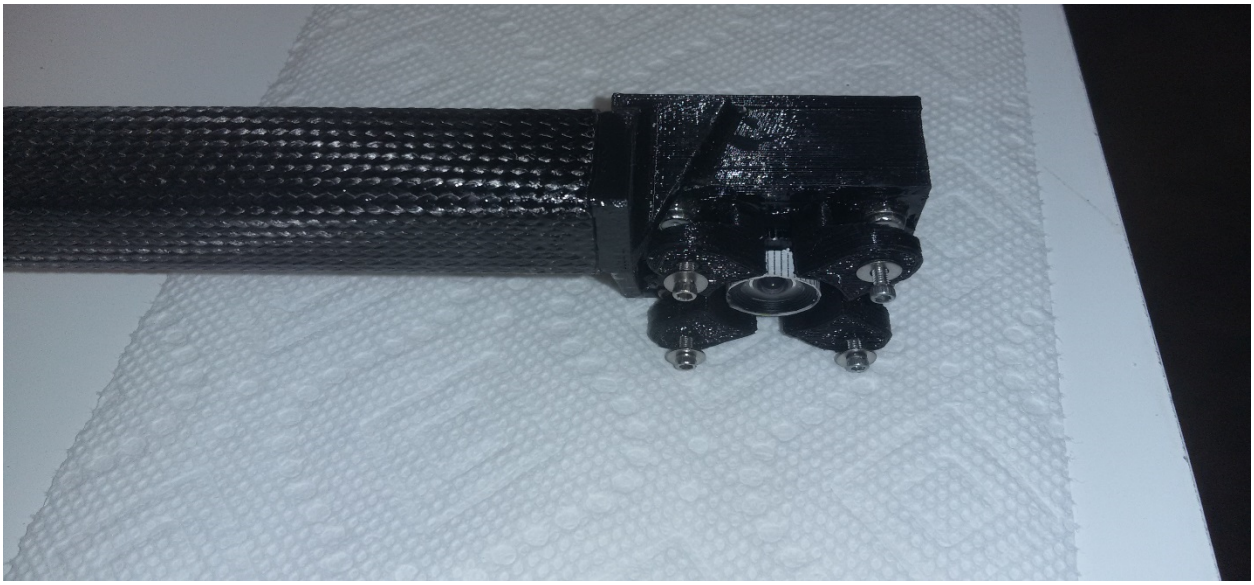

Figure 2.14: Camera mount glued to spar with camera installed.

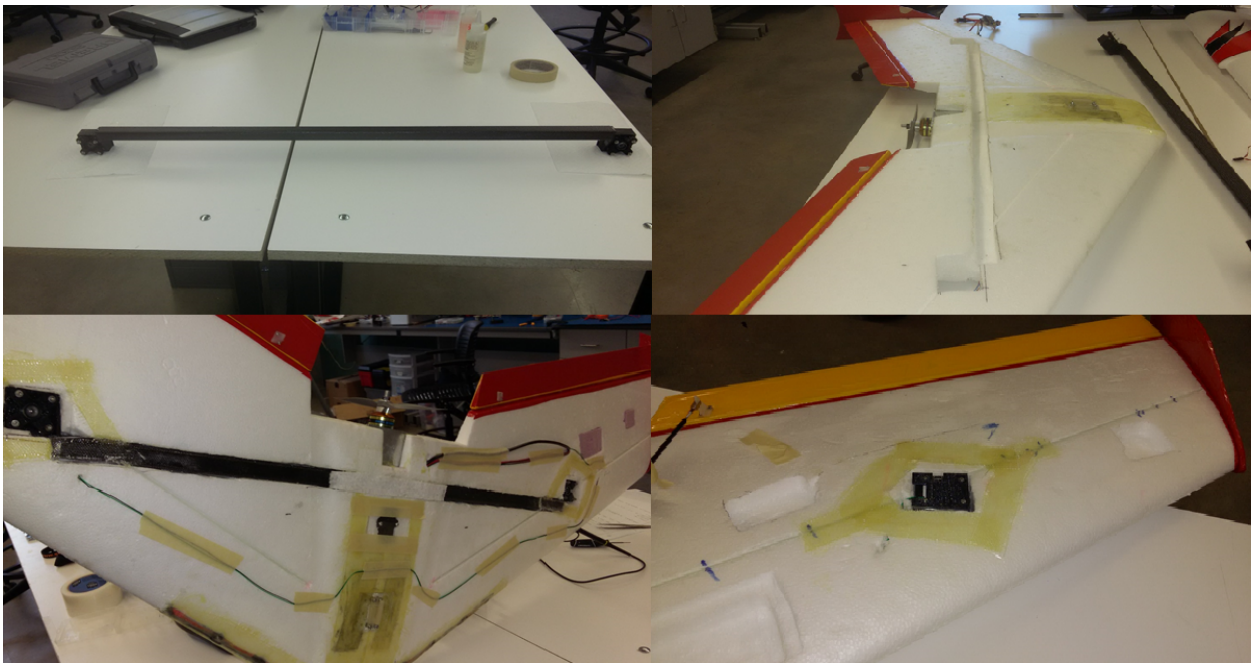

Figure 2.15: Carbon spar assembly and mounting.

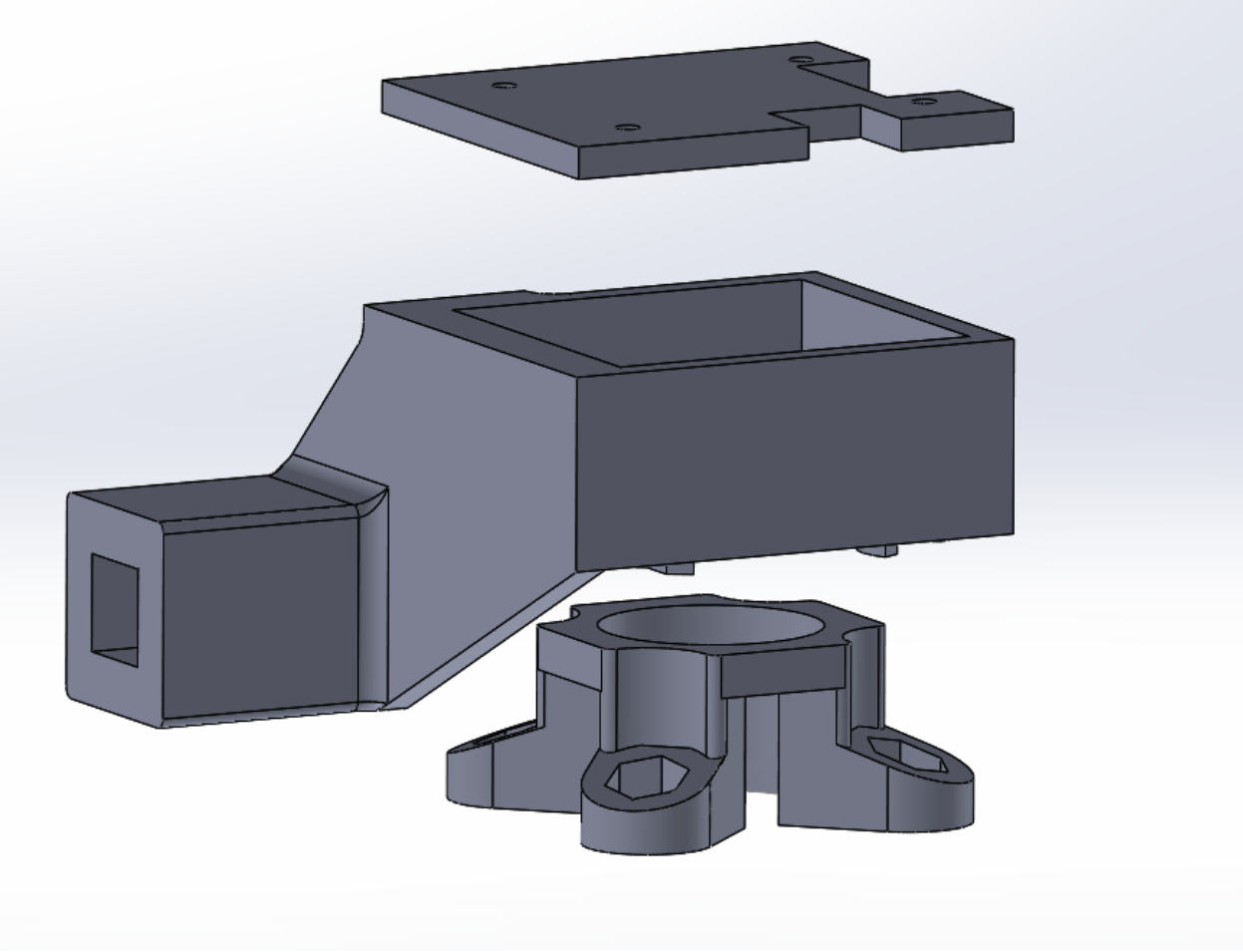

Figure 2.16: Right camera mount assembly.

2.5 Flight Tuning and Validation

2.5.1 Flight Tuning

After the UAS has been built and ground tested, the next step is flight tuning. This includes aircraft mechanical trimming and flight controller tuning. The procedure can be described as follows.

1. Initial trimming. The objective is to make sure the aircraft is trimmed to fly straight and level. The servo arms need to be repositioned to account for any trim added during the flight. This is so that no manual trim (from the transmitter) is needed which could cause confusion to aircraft system identification and the autopilot flight controllers.
2. After the trimming of the UAS, the next step is to determine the cruise speed for the aircraft.

The aircraft is set through a series of maneuvers including: straight and level flight, right and left turns, and right and left circles. These maneuvers are suggested to be performed at the same altitude in order to determine if the aircraft can maintain its altitude.

3. Trim the aircraft again after the new trim velocity has been determined, and readjust the servo arm so that no manual trim is needed.

4. Controller tuning should be performed if the UAS is going to be used in autonomous mode. It should also be tuned either manually or automatically for the purpose of getting a baseline (or legacy) controller. Depending on the flight controller, the Paparazzi or Pixhawk autopilot, the initial controller tuning can be performed in two different ways:

   (a) Manual tuning can be used on the Paparazzi UAS initially before the system dynamic model is known. Manual tuning is performed by using step inputs and doublets that command the aircraft to desired roll and pitch angles in Auto1 mode and then by adjusting the proportional (P) gain until oscillation occurs [4]. The oscillation is then tuned out using the derivative (D) gain until the aircraft is stable and can produce a step or doublet response with minimal oscillations and minimal overshoot. This process of tuning the P and D gains can continue until a satisfactory result is reached. The integral (I) gain is added last for the purpose of reducing steady state error and is usually small.

   (b) Automated tuning is another method to determine the controller gains. For the Pixhawk autopilot, the aircraft is rolled left and right first for about 20 times and then pitched up and down continuously for another 20 times (similar to 20 doublets commands). This allows the Pixhawk to determine a gain set for the aircraft that produce a desirable response in terms of rise time, overshoot, and overall stability [5].

5. Additional tuning after the inner loop controller has been determined should include mission specific tuning involving the ability of the aircraft to follow flight paths relative to the mission. This could include following flight lines for remote sensing. The plane may need to fly at a certain altitude to maximize swath coverage and resolution.

2.5.2 Validation of KHawk UAS Platform

This section is for the purpose of showing the success of the KHawk UAS building, modification, and tuning procedure, through flight validation. Fig. 2.17 shows automated flight data from the KHawk 55 Thermal Vision UAS during a test to simulate a fireline surveillance flight, where the aircraft flies back and forth over a controlled burn field fire. As can be seen from the figure, the aircraft successfully maintained the desired altitude while tracking a straight line. The desired versus true flight path of the KHawk 55 Thermal Vision UAS is shown in Fig. 2.18.

2.6 Conclusion and Future Works

The KHawk UAS building, modification, part design, testing, tuning, and flight procedures are presented in detail in this chapter. The procedures have successfully been used by the CUSL lab to produce flight worthy UAS capable of performing mission related goals in challenging weather conditions. These procedures can also be applied to other small foam UAS and petentially even larger UAS

Future works regarding this procedure include 1) other types of UAS such as quadrotors, helicopters, VTOL UAS, and fully composite UAS, 2) mission specific UAS meant to handle high temperatures from fires, and 3) flexible aircraft to support research on aircraft structure controller coupling.

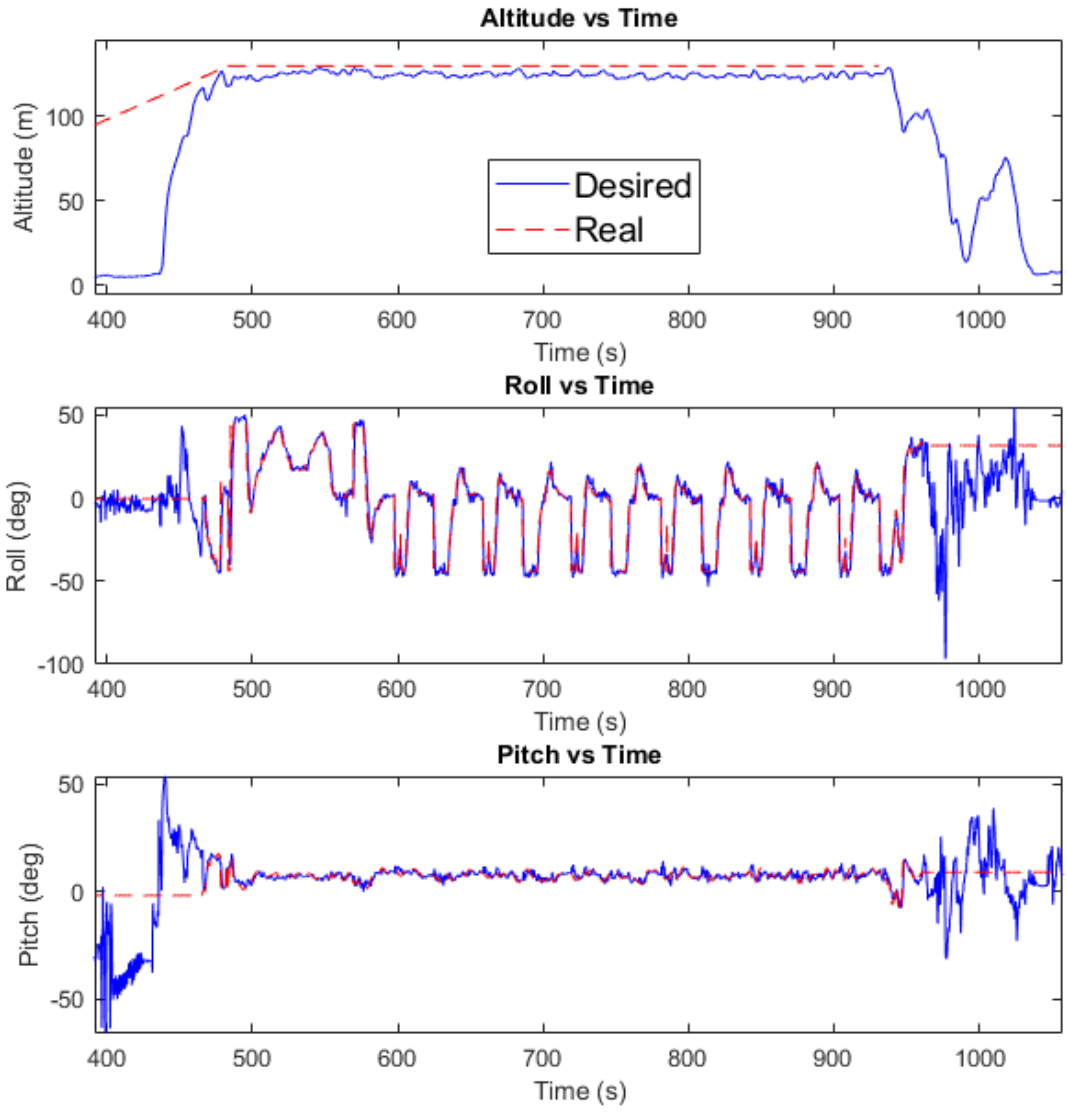

Figure 2.17: Automated flight from KHawk 55 Thermal Vision UAS.

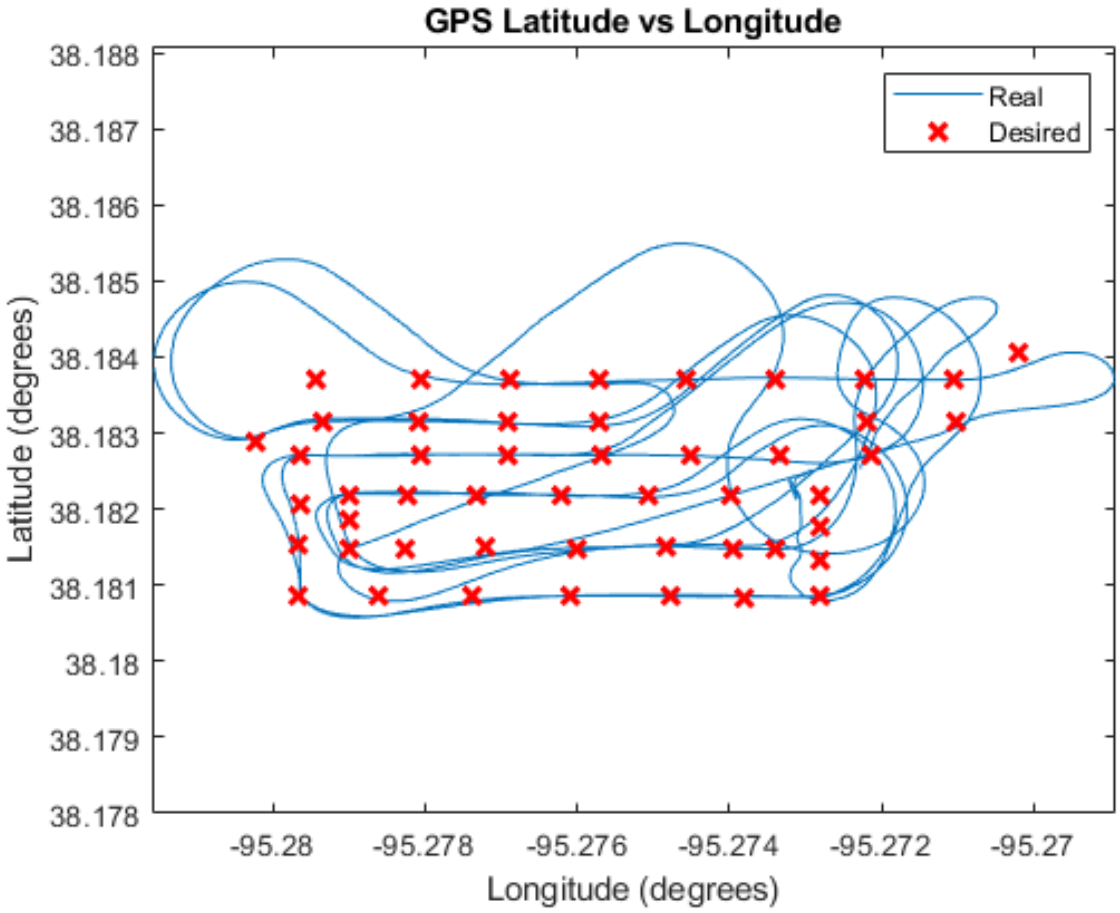

Figure 2.18: Desired GPS position of the aircraft vs real flight path.

Chapter 3

Coupled Lateral System Identification and Roll Controller Design

Abstract

System identification and model based controller design is an increasingly important area for UAS research. As UAS are used in more challenging turbulent conditions, it is critical to have accurate system identification, controller design, and controller validation for improved aircraft safety, robustness, and efficiency. The roll loop of a flying-wing UAS is examined in this chapter including lateral system identification, controller design, and controller validation. This chapter also introduces a new procedure for utilizing frequency domain analysis to identify and validate the lateral directional models and roll controller design of a UAS, and determine gain sets using a graph based approach to meet controller design objectives such as: gain/phase margin, crossover frequency, disturbance rejection bandwidth, and disturbance rejection peak. Accurate roll attitude tracking performance is achieved in turbulent conditions, which is shown in both simulation and flight results. Additionally, good agreement is observed between simulated roll controller performance and UAS flight test results, which showed the effectiveness of the overall system identification and control design practice.

3.1 Introduction

Unmanned aircraft systems (UAS) are increasingly used for different applications by academia, industries, and the military over the past several decades [6], including aircraft guidance, navigation, control [7], atmospheric measurements, autonomy, remote sensing, etc. Many UAS are deployed in challenging conditions such as high winds and turbulence, which could result in poor mission performance or even the destruction of the UAS if the controller is not well designed and validated. For instance, UAS based wildfire monitoring missions [8] or volcanic monitoring missions [9] would require a controller capable of dealing with large variations in turbulence as the UAS flies in the vicinity of the fire or smoke generated from the fire. Similarly, micro aerial vehicles (MAV) may need fast acting controllers and sensors in order to safely navigate around buildings and obstacles in cities due to the presence of structure generated turbulence [10; 11].

While controller performance is an extremely important issue, handling qualities and controller design specifications are not well defined especially for small UAS ($<$ 55 lbs). Currently, military standards exist for piloted aircraft [12] and few research exists regarding the categorization and handling quality evaluation process for UAS [13]. Froude scaling methods can sometimes be used to determine UAS handling qualities by scaling down full-scale aircraft design specifications [14]. Previous research on UAS stability attempted to apply military standards to UAS, and quantify the stability of the system without sacrificing controller performance [15; 16]. However, little information is available regarding stability specifications for UAS controller design, which is extremely important since UAS are being used more extensively in turbulent flight scenarios around populated areas.

The robustness of the controller is largely dependent on the correct gains selected for modeling uncertainties, measurement noises, and environmental disturbances, which can be obtained through experimental tuning (trial and error) or via model based gain selection approaches. Many classical controller design techniques have been used on the attitude tracking problem of manned aircraft and unmanned aircraft for gust rejection [17]. Pole placement is a classical technique for the controller design, but poses problems for systems with high order models and nontrivial delays

[18]. The rigorous amount of analysis required for traditional full-scale fly-by-wire aircraft can be tedious and may not be as applicable for UAS which have simpler certification and fault tolerance requirements [19; 20]. Recently, open source autopilots such as the ArduPilot software support automatic tuning of the inner-loop controller gains by performing 20-30 sine wave inputs in series of the desired attitude command. However, a stable initial guess of the controller gains is needed to start the process, and further manual fine tuning is needed for best performance [4; 5; 21]. In addition, the performance of a flight tuned controller cannot be predicted or certified for challenging flight conditions without further system modeling and validation work.

System identification techniques have been widely used to determine unmanned and manned aircraft models for motion simulation, flight controller design [22; 23], and even turbulence model generation [24]. The controller parameters can be determined through comprehensive simulation and flight test analysis using time and frequency domain methods. It is worth emphasizing that frequency domain data from flight tests can be analyzed to get critical controller design parameters such as gain margin and phase margin (GM/PM) and the disturbance rejection bandwidth and disturbance rejection peak (DRB/DRP), which can be compared to predicted aircraft responses using earlier identified models. The difference between simulated and real aircraft responses under the same controller can be further used to determine the most accurate aircraft model for lateral controller design [14].

This chapter introduces a new method for coupled lateral system identification and controller tuning of a small flying-wing UAS, which is difficult to model due to the lack of rudder and the simplicity of the platform in its structure and aerodynamics. The second major contribution of this chapter is the introduction of a multi-objective graph-based roll controller tuning rule in consideration of multiple time and frequency domain control objectives including roll tracking performance as well as stability and disturbance rejection requirements. Our multi-objective tuning procedure fills in the gap for fine tuning of small UAS equipped with an open source autopilot. Lastly, detailed simulation and flight test validations were performed using the KHawk 55 UAS platform including suggested procedures for small UAS system identification, acquired SISO and

SIMO lateral dynamic UAS model, and detailed analysis on controller performance.

This chapter follows the outline below: Sec. 3.2 is the problem statement. Sec. 3.3 describes the aircraft lateral directional dynamic model. Sec. 3.4 introduces UAS roll controller specifications and gain selection optimization. Sec 3.5 discusses system identification for the KHawk 55 UAS. Sec. 3.6 covers initial gain selection for system controller validation and simulation based controller fine tuning. Sec. 3.7 provides analysis of flight data for both the initial and final gain sets. Sec. 3.8 provides discussion and conclusions for the chapter.

3.2 Problem Statement

This chapter focuses on the design and tuning of a roll tracking controller through system identification and model based analysis, simulation, and flight validation. The roll tracking controller in this chapter uses a PD (proportional and derivative) type controller for faster aircraft response. Note that similar analysis can be performed on PID controllers as well. As a rule of thumb, a small integral gain can be added to the controller to correct for steady state error after the PD controller has been designed [18]. The primary elements of the roll controller are:

- control input to the ailerons via servo command,
- desired command for roll angle or bank angle,
- system states such as roll angle, roll rate, side velocity, and yaw rate.

The controller design objectives for a full-scale aircraft usually involve time domain and frequency domain requirements. These requirements are generally based on military standards, civilian standards [19], or internal company handling quality requirements. It is worth emphasizing that UAS currently do not have such standard requirements. This chapter focuses on incorporating stability and disturbance rejection requirements to small flying-wing UAS including GM/PM, crossover frequency (ω_{cr}), and DRB/DRP, which quantify the controller's ability to reject disturbances to the system. The roll controller design can be summarized as three subsections: aircraft system identification, controller optimization and analysis, and experimental validations. The chal-

lenges for model based roll controller design and tuning include:

- few literature for system identification can be found on the modeling of small UAS, especially small rudderless UAS,
- missing standards for UAS controller specifications and certifications,
- uncertainties in UAS hardware and software such as servo installation, servo response uncertainty, IMU alignment, sensor accuracy, and processor timing accuracy,
- wind and turbulence impact on small UAS.

Fig. 3.1 shows the flow chart for the system identification and model selection, controller design, flight validation, and controller finalization. Once the system identification and model selection have been determined, the initial controller can be designed using the selected model. The flight validation involves performing a set of maneuvers to generate the frequency response of the closed loop system which can then be compared to the simulated frequency response to determine which model has the best accuracy. If the results agree, then the finalization of the controller can be completed.

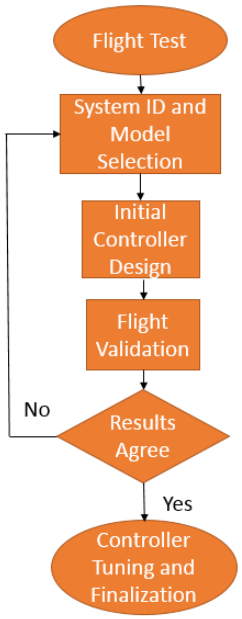

Figure 3.1: Controller tuning and analysis flow chart.

3.3 Aircraft Lateral Directional Dynamic Model

Lateral aircraft dynamics can be represented using different models. A nonlinear 6-degrees of freedom (6-DOF) model provides the most accurate model to represent aircraft dynamics but requires considerably more effort for system identification. Three models are used in this chapter: a first order system, high order system, and state space model, to represent the aircraft's lateral dynamics and for later controller design. The simplest model is the first order plus time delay model and can be described as:

$$\frac{p}{\delta_a} = \frac{L_{\delta_a} e^{-\tau_d s}}{s - L_p}, \tau_r = \frac{1}{-L_p}, \text{ and } K_{ail} = \frac{L_{\delta_a}}{-L_p}, \tag{3.1}$$

where τ_r is the roll mode constant, τ_d is the time delay constant, and K_{ail} is the aileron gain or the roll rate per aileron deflection angle. The first order plus time delay model is the simplest model used in this chapter and should be considered as an extreme case given that it does not take into account the Dutch roll mode or spiral mode. If the Dutch roll mode interacts heavily with the roll mode due to low damping, the first order plus time delay approximation may not accurately represent the aircraft's roll dynamics [25]. Other than the first order model, a single input single output (SISO) model can also be identified using a high order transfer function [25].

$$\frac{p}{\delta_a} = \frac{L_{\delta_a} s(s^2 + 2\zeta_{n_\phi}\omega_{n_\phi} s + \omega_{n_\phi}^2) e^{-\tau_d s}}{(s + 1/\tau_s)(s + 1/\tau_r)(s^2 + 2\zeta_{dr}\omega_{n_{dr}} s + \omega_{n_{dr}}^2)} \tag{3.2}$$

The SISO high order parameters are the roll mode constant (τ_r), spiral mode constant (τ_s), Dutch roll mode damping and natural frequency (ζ_{dr} and $\omega_{n_{dr}}$), and the Dutch roll coupling zeros damping and natural frequency (ζ_{n_ϕ} and ω_{n_ϕ}). Aside from the SISO models, the lateral dynamics of an aircraft can also be represented by a single-input multi-output (SIMO) model around the trim point for a rudderless flying wing aircraft. Two different state space models can be set up including the classical form ($\dot{x} = Ax + Bu$) and the advanced form that considers the turbulence impact on the aircraft. The latter form includes a turbulence component shown in equation (3.3) [26; 27; 28].

$$\dot{x} = Ax + Bu + Tw_g \tag{3.3}$$

Equation (3.4) shows the full state space equation where v is the lateral directional airspeed, p and r are roll and yaw rate, ϕ is the roll angle, U_0 and W_0 is the cruise speed along body x and z directions, Θ_0 is the steady state pitch angle, and τ_d is the time delay for the system. Y, L, and N are stability and control parameters, and v_g, p_g, and r_g are turbulence velocities.

$$\begin{bmatrix} \dot{v} \\ \dot{p} \\ \dot{r} \\ \dot{\phi} \end{bmatrix} = \begin{bmatrix} Y_v & Y_p + W_0 & Y_r - U_0 & gcos(\Theta_0) \\ L_v & L_p & L_r & 0 \\ N_v & N_p & N_r & 0 \\ 0 & 1 & tan(\Theta_0) & 0 \end{bmatrix} \begin{bmatrix} v \\ p \\ r \\ \phi \end{bmatrix} + \begin{bmatrix} Y_{\delta_a} \\ L_{\delta_a} \\ N_{\delta_a} \\ 0 \end{bmatrix} \delta_a(t - \tau_d) + \begin{bmatrix} -Y_v & 0 & 0 \\ -L_v & -L_p & -L_r \\ -N_v & -N_p & -N_r \\ 0 & 0 & 0 \end{bmatrix} \begin{bmatrix} v_g \\ p_g \\ r_g \end{bmatrix} \tag{3.4}$$

The above lateral dynamic models can be determined through flight tests using frequency sweeps (or "chirp") techniques [25; 29]. The details will be explained in Sec. 1.6.

3.4 Roll Attitude Controller Design

Once the system model is obtained, gain selection is the next step for the roll controller design. This chapter proposes a new graph-based gain selection method (KHawk tuning rule) using multi-objective optimization in consideration of time domain and frequency domain controller specifications. The designed controller can achieve good roll tracking performance while meeting stability and disturbance rejection requirements. It is worth emphasizing that little literature exists on stability and disturbance analysis for attitude tracking controllers of small UAS and open source UAS autopilots rely on the end user for manual fine tuning [4; 5]. Our tuning rule extends the works of [25; 18] and fills in the gap for model based controller design for small UAS, which supports different models including first order, high order, and state space.

3.4.1 System Diagram for Controller Design and Analysis

The overall system diagram for controller design and analysis is showed in Fig. 3.2. Note that the proposed structure can support either first order SISO, high order SISO, or state space SIMO models without losing generality for the roll model. Additionally, the time delay includes the actuator dynamics as well as the avionics system delay. The combined control objectives of stability, tracking, and robustness can be analyzed from three loops shown in Fig. 3.2.

- Roll angle tracking loop, with the objective to track desired roll angle.
- Actuator broken loop, with the objective to analyze the controller stability and robustness under actuator disturbance such as turbulence.
- Measurement disturbance rejection loop, with the objective to analyze the controller robustness under measurement disturbance such as measurement error, system delay, or turbulence.

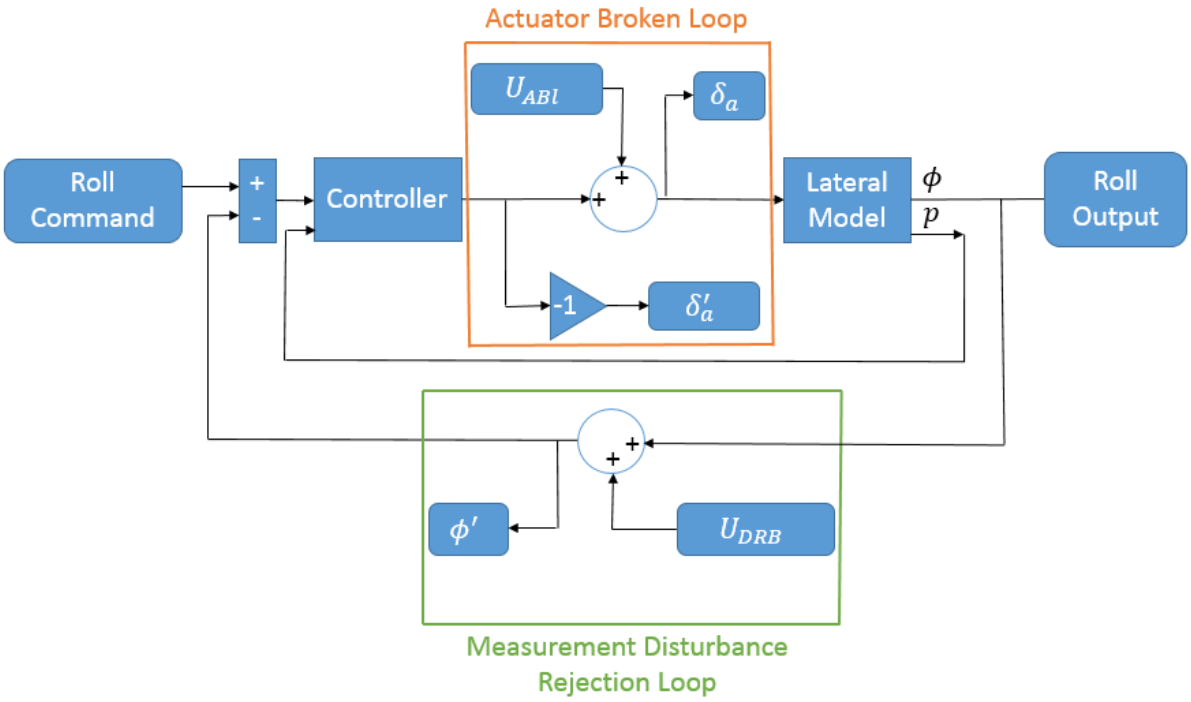

Figure 3.2: Lateral control system structure.

Both time domain and frequency domain analysis will be performed on the roll tracking loop, and frequency domain analysis is focused on the two broken loops. Especially, the actuator broken

loop is investigated to determine control system behavior under different turbulence conditions (such as gust generated actuator disturbances) and to confirm the loop gain and phase margins. One extra advantage of this analysis is its ability to examine the aircraft's system time delay by comparing flight data to the identified model. The obtained broken loop flight data can be compared with simulated aircraft responses for the determination of the system time delay constant. In the coming subsection, multiple controller specifications from the above three loops will be introduced in detail.

3.4.2 Controller Specification and Multi-Objective Optimization

The roll controller specifications are first introduced and then the optimization strategy is provided in this subsection. The related controller can be summarized as the following:

- Roll tracking specifications
  - Rise time and settling time describe the controller's transient tracking ability and can be set as a small value for small UASs.
  - Damping (ζ) describes the system oscillatory behavior and is usually set between 0.6 and 1 for good tracking and to prevent large overshoot from turbulence interaction.
- Actuator broken loop specifications
  - GM/PM describes the stability of the aircraft. The smaller the GM/PM, the closer to instability the aircraft gets.
  - ω_c describes the control surface actuator activity. Higher crossover frequency corresponds to faster actuator response and better rejection of turbulence.
- Measurement disturbance rejection loop specifications
  - DRB describes the system's response to turbulence and the rate at which the aircraft returns to trim and is located at the -3 dB crossing of the disturbance rejection loop magnitude. The higher the DRB, the faster the aircraft will return to trim.
  - DRP is the largest peak of the disturbance rejection loop magnitude and describes the

disturbance frequency that most effects the aircraft (greatest load impact from turbulence).

The KHawk 55 multi-objective optimization procedure can be described as the following:

- Identify and select model(s) to represent the system. Tuning can be completed using first order, high order, or state space models.
- Determine mission related criteria for gain selection.
  - Turbulence rejection: controller should provide large w_c and DRB while maintaining a reasonable damping ratio and DRP.
  - Stability: controller should be well within the allowable gain/phase margins.
  - Tracking: controller should have the rise time and settling time be within reasonable ranges, and ζ should be 0.6 or above.
- Constrain gain selection by choosing boundaries for each specification.
- Select gain set based on desired performance criteria and lowest RMS error (turbulence rejection) for roll tracking within design parameter ranges.

Detailed design specifications with their respective constraints are shown in Table 3.1, which is similar to manned aircraft [18].

Table 3.1: Design specification constraints

Specification	Constraint
Gain Margin	Stability
Phase Margin	Stability
Crossover Frequency	Stability/Objective
Disturbance Rej. Bandwidth	Quality/Objective
Disturbance Rej. Peak	Quality
Damp. from Overshoot	Quality/Tracking
Rise Time	Quality/Tracking
Settling Time	Quality/Tracking

3.4.3 Controller Analysis and Specification Calculation

Controller analysis, including the determination of different specifications from analyzed results or simulation data, is a key step for the overall controller design. Two different approaches are used in this chapter: data driven analysis and analytical method based analysis. Data driven analysis involves the estimation of the actuator broken loop and measurement disturbance rejection loop specifications using simulation data. The analytical method involves utilizing the identified system model to calculate the actuator broken loop and measurement disturbance rejection loop specifications. The data driven analysis has wider applications because it is independent of the system model.

3.4.3.1 Data Driven Analysis

Data driven analysis can be performed using lateral controller simulations or flight test data with different programs such as Matlab/Simulink, CIFER [25], or CONDUIT [30]. Matlab/Simulink can be used with its control design frequency response estimation tool to determine the broken loop specifications. The system structure for both cases is shown in Fig. 3.2. The generalized actuator disturbance equations for the system are shown below in equations (3.5-3.6).

$$\frac{\delta_a^{'}}{\delta_a} = \frac{(K_d s + K_p)G(s)}{s} \tag{3.5}$$

$$\frac{\phi^{'}}{U_{DRB}} = \frac{s(K_d G(s)+1)}{s(K_d G(s)+1)+K_p G(s)} \tag{3.6}$$

where G(s) is the generalized roll model (δ_a/p) which can be a first order or high order model and K_p and K_d are the proportional and derivative gains. The broken loop at the aileron chirp is added to obtain the δ_a and $\delta_a^{'}$ so that a comparison can be made between the command and the command effected from a system disturbance. Given $\delta_a^{'}/\delta_a$ and $\phi^{'}/U_{DRB}$ data from simulation or flight tests, the controller specifications (GM/PM, ω_c, DRB, DRP) can then be calculated and compared with the design objective.

3.4.3.2 Analytical Method

If the aircraft's roll mode is not influenced heavily by the dutch roll mode, the first order plus time delay model may prove sufficient which is shown in the equations below.

$$\frac{\delta_a^{'}}{\delta_a} = \frac{(K_d s + Kp) L_{\delta_a} e^{-as}}{s(s - L_p)} \tag{3.7}$$

$$\frac{\phi^{'}}{DRB_{Chirp}} = \frac{s(s - L_p + K_d L_{\delta_a} e^{-as})}{s^2 - (L_p - K_d L_{\delta_a} e^{-as})s + K_p L_{\delta_a} e^{-as}} \tag{3.8}$$

The broken loop equation can be further decomposed to calculate the magnitude and phase of the system so that the GM/PM can be calculated.

$$|M_{br}(jw)| = \frac{L_{\delta_a}\sqrt{K_d^2 w^2 + K_p^2}}{w\sqrt{w^2 + L_p^2}} \tag{3.9}$$

$$\angle P_{br}(jw) = \arctan(\frac{K_d w}{K_p}) - aw - \arctan(\frac{w}{-L_p}) - 90^o \tag{3.10}$$

The GM/PM should be kept within the specified ranges based on stability requirements, which will be explained in detail in Sec. 1.6.

3.5 KHawk 55 UAS System Identification

The KHawk 55 UAS was used for flight data collection and system identification. The UAS's lateral models are determined using frequency domain system identification under nominal flight conditions.

3.5.1 System Identification

3.5.1.1 Flight Test Procedure

The system identification flight was performed by commanding a frequency sweep or “chirp” to the ailerons causing the aircraft to oscillate in roll at a progressively increasing frequency [25]. This allows for identification of the aircraft modes in the frequency domain by exciting the aircraft across its modal frequency range.

The following steps are suggested for effective generation of small UAS system identification data set:

1. Frequency range selection. The frequency range selected for the "chirp" of a small flying-wing UAS is suggested to include sufficient low range frequencies (about 0.25 rad/s) and sufficient high range frequencies (up to about 30 rad/s). The longer the sweep can be performed the more information the "chirp" data will have.
2. Velocity and roll magnitude consideration. The velocity should be maintained as a constant, or as close as it allows. The roll magnitude for the "chirp" should provide a good signal to noise ratio (SNR) so that the sweep data can be distinguished from turbulence and wind effects, but not so aggressive that non-linearity is reached (large variations in velocity and pitch).
3. Excitation type selection. Both manual and automated chirp inputs can be used for system identification. Manual chirps were used in this chapter because of the simple implementation, wide low frequency range, incorporation of pilot compensation to stay on trim, and broad spectral content. A manual chirp input and roll rate response is shown in Fig. 3.3.
4. Nominal pitch. For this chapter, the nominal pitch angle was Θ_0 = 6 degrees and was chosen from straight and level flight and was comparable to the average Θ_0 for four separate manual sweeps.
5. Data quality check of p, r, and ay. The quality of the system ID data set can be usually checked during or right after the flight test by looking at the magnitude and frequency changes.
6. Validation. Doublet inputs can be utilized in the time domain to verify the state space model

in comparison to real flight data.

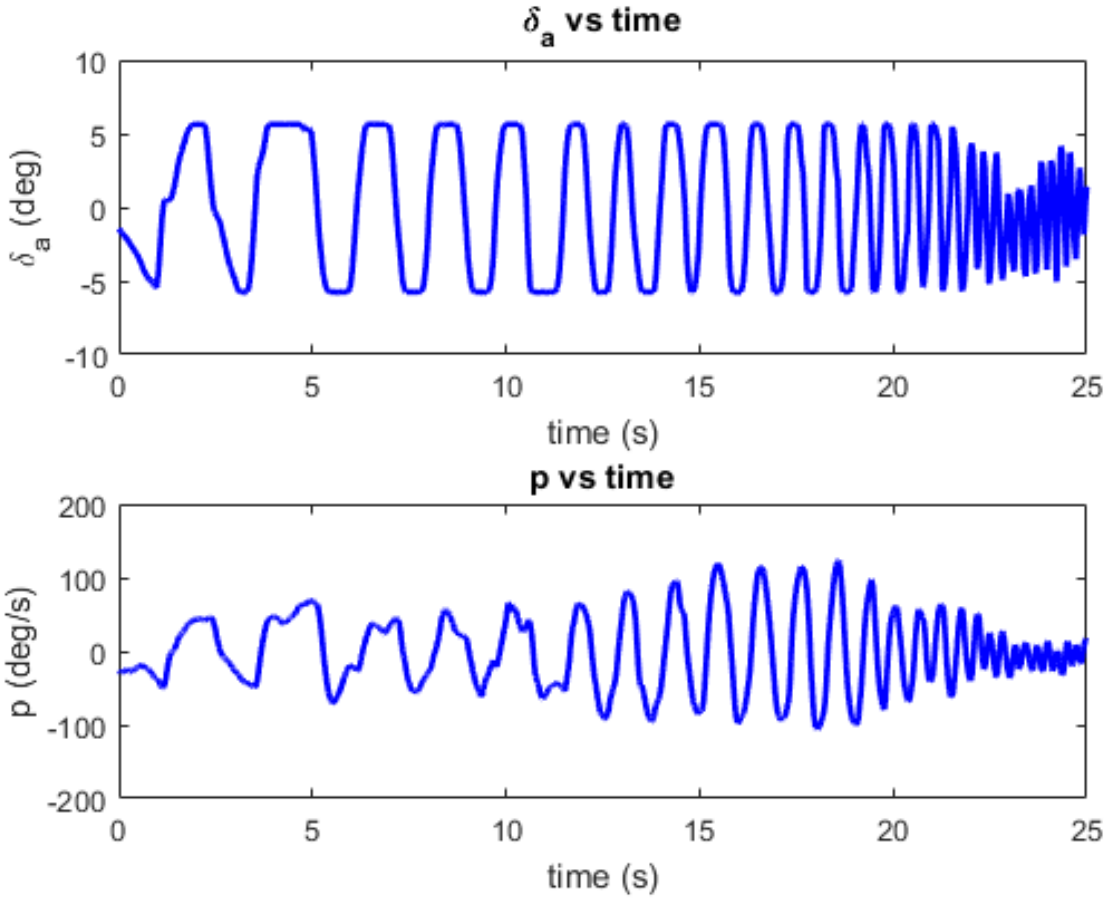

Figure 3.3: Aileron sweep generated from manual input.

3.5.1.2 CIFER System Identification Analysis

The system identification was performed using the software application CIFER (Comprehensive Identification from Frequency Responses) free student version [25]. CIFER incorporates several modules for the frequency response transformation, transfer function fit, and state space model identification and verification. The FRESPID module in CIFER was used to combine multiple chirps into a single record. It also is used to transform the time-domain data into the frequency domain using a chirp-z algorithm. The COMPOSITE module was then used to apply a multi-windowing techniques to yield a MIMO database of high bandwidth and high coherence. NAVFIT

was used for transfer function fitting from the frequency responses while DERIVID was used to perform the state space model determination.

Four chirps and one doublet were collected and used. The flight data were recorded at 100 Hz (except for the command aileron position which was recorded at 20 Hz) including the aircraft body rotation rates, accelerations, Euler angles, and airspeed. Note that since the aileron command was recorded, the identified models include the servo dynamics and communication delay, which is typically lumped as a pure time delay. The 1^{st} order roll approximation NAVFIT results are illustrated in Fig. 3.4 and provided below in equation (3.11).

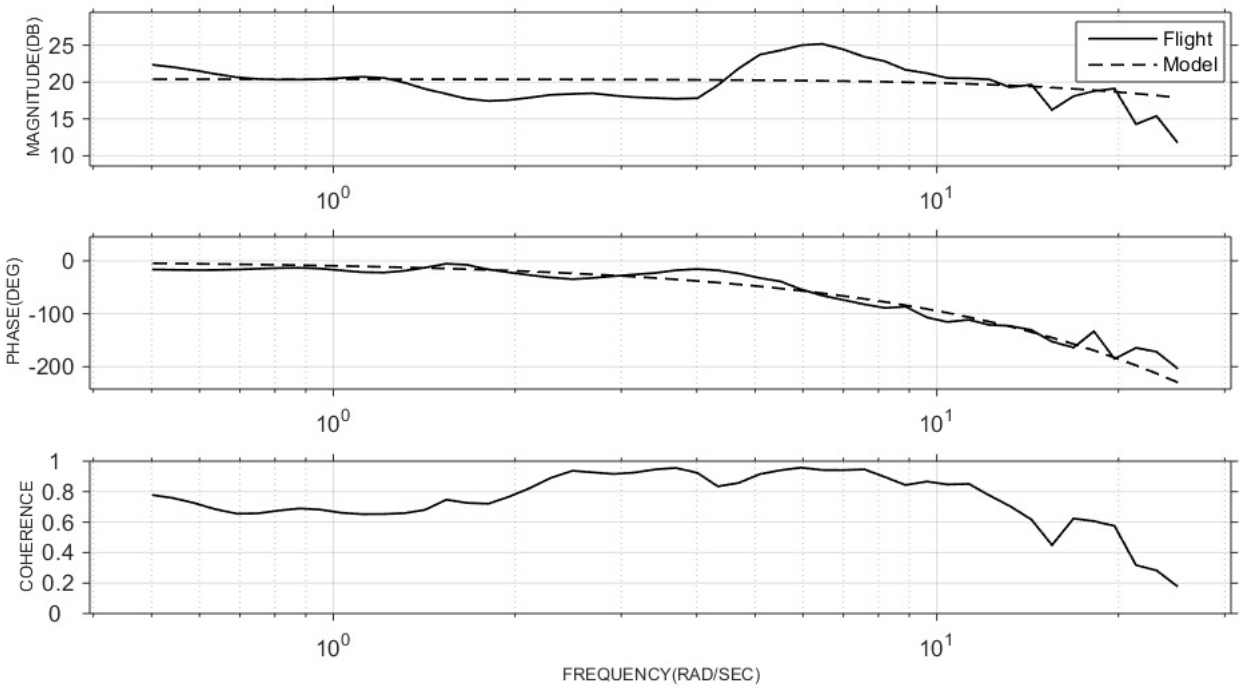

Figure 3.4: Roll rate response 1^{st} order model matching (J=113).

$$\frac{p}{\delta_a} = \frac{297.5e^{-0.131s}}{s+28.46}. \tag{3.11}$$

The first order equation is both the simplest and easiest equation to calculate. However, the equation only focuses on the roll mode and not the Dutch roll or spiral mode, which will make controller tuning more challenging for this airframe because the KHawk 55 UAS has a lightly damped Dutch roll mode. The included coherence plot shown in Fig. 3.4 indicates the fraction of

the response which is linearly related to the input. A coherence of one represents a perfect match while a coherence greater than 0.6 is considered adequate for system identification [25]. From this figure, one can see good coherence across a wide frequency range, indicating that the data is adequate for system identification. However, the coherence value drops under 0.6 for frequencies above 15 rad/s. The cost function (J) for this fit was 113. This is a measurement of the accuracy of the fit for the model, where costs below 100 are considered a good fit and costs below 50 are excellent. Given this high cost, the high order (3rd/4th) roll rate SISO transfer function, which includes the coupled Dutch roll mode, was identified.

To support the identification of both the high order SISO model and the state space model, the body axis side acceleration was reconstructed in the time domain from the recorded parameters using the following [25]:

$$\dot{v} = a_y - U_0 r + W_0 p + g cos(\Theta_0)\phi. \tag{3.12}$$

The use of body axis side acceleration ($\dot{v}$) is used in aircraft identification as this parameter can be accurately reconstructed from available parameters and readily integrated in the frequency domain to yield the body axis side velocity (v) which is related to the aerodynamic sideslip angle via:

$$\beta \approx v/U_0. \tag{3.13}$$

The body axis acceleration signal was reconstructed as shown above, transformed into a frequency response, and then integrated to yield the response and Dutch roll mode identification [25] shown in Fig. 3.5. The frequency range of this fit was reduced to minimize the impact of other zeros in the aileron to side velocity (βU_0) response fit. Note that this is conventionally done with the rudder to sideslip response. However, for the KHawk 55 UAS, only aileron controls are available. With the Dutch roll mode identified from the aileron to sideslip response and constrained [25], the remaining parameters from the high order SISO aileron to roll rate response were identified with a very low cost fit ($J = 19.2$). The results of this identification are illustrated in Fig. 3.6 and provided

below.

$$\frac{p}{\delta_a} = \frac{143.3s(s^2+2(0.23)4.16s+4.16^2)e^{-0.114s}}{(s-1/9.98)(s+1/0.103)(s^2+2(0.22)5.05s+5.05^2)} \tag{3.14}$$

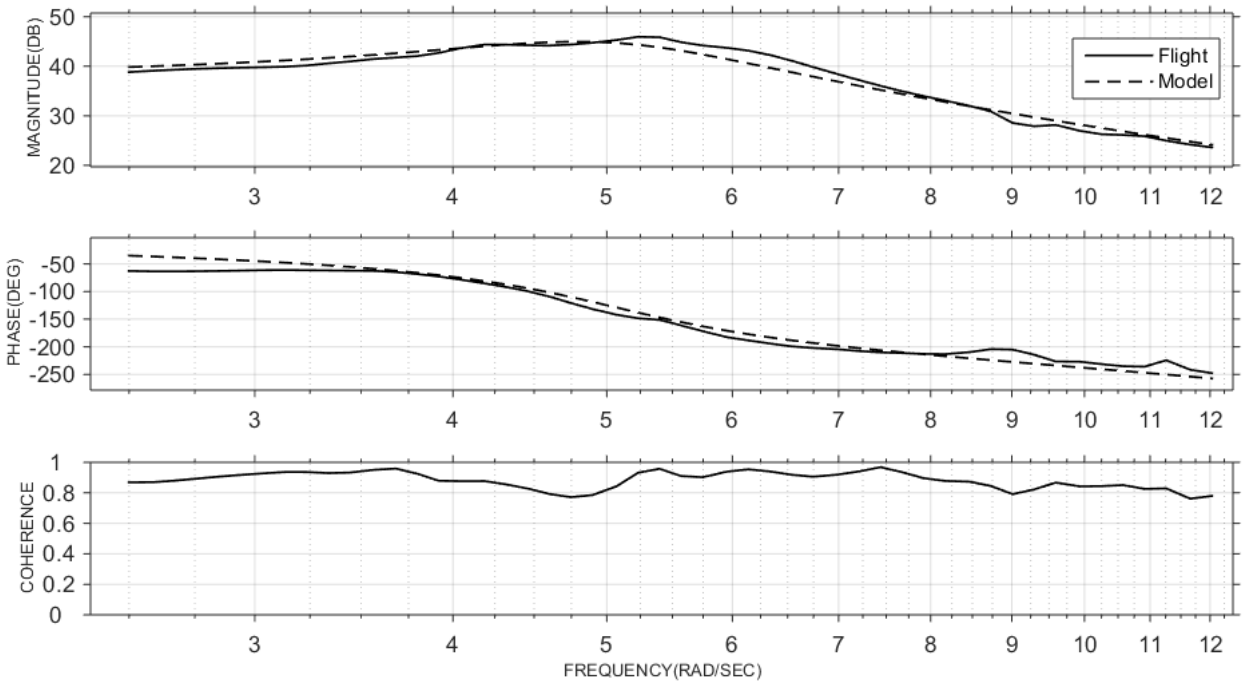

Figure 3.5: Side velocity (v) response 2^{nd} order Dutch roll model matching (J=75.5).

The final identification task performed was the state space model identification using CIFER's DERIVID module. The fitting of the responses to the state space model ensures that the identified model is constrained to the expected physics for an aircraft 3-DOF model captured in the state space structure shown in Section III. This identification process performs a simultaneous fit of the model to the frequency responses from the measured roll rate, yaw rate, lateral acceleration, and reconstructed side acceleration as outlined in [25] and demonstrated in [29]. For each of the frequency responses, the frequency range of the fit is tailored to match the range consistent with good coherence. This process includes utilizing a set of output equations to translate the states into the measured quantities, roll rate, yaw rate, and lateral acceleration, which ensures consistency between the states and the measurements. For this aircraft, no sensor location offsets were employed. As in the NAVFIT cases, only aileron frequency responses were available.

The results of this identification are shown in Fig. 3.7-3.8 and equation (3.15). For brevity,

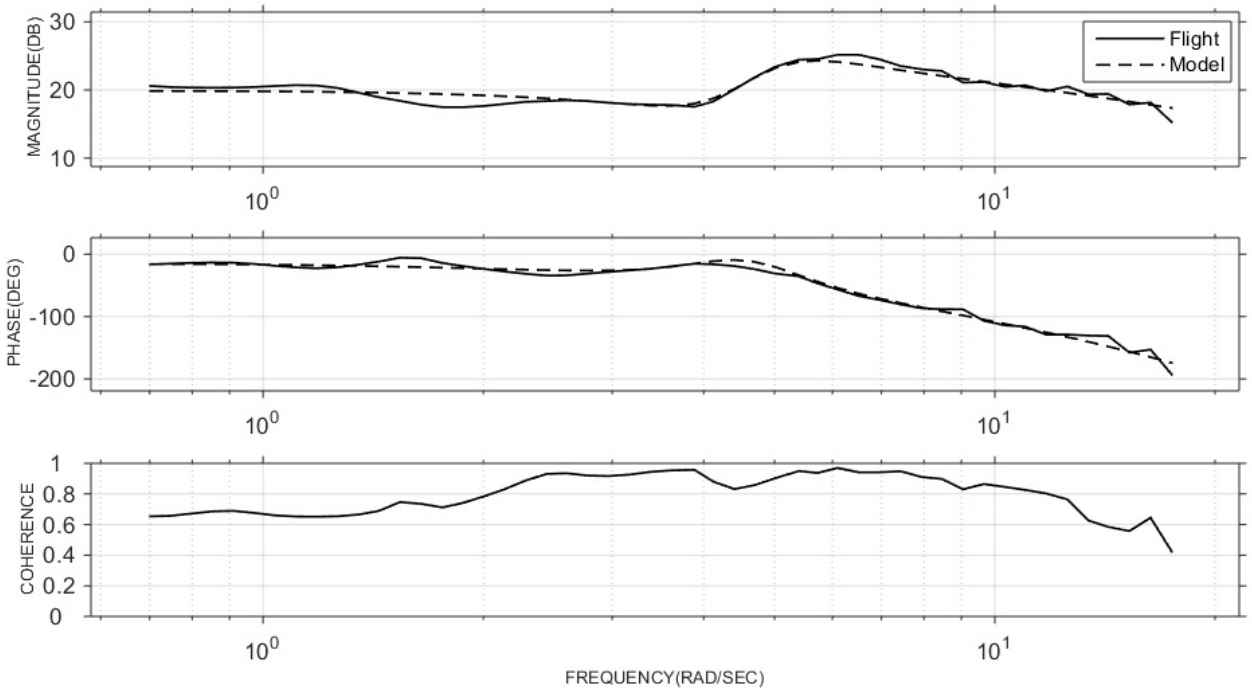

Figure 3.6: Roll rate response 4^{th} order model matching ($J = 13.4$).

the yaw rate figure was excluded. However, the cost is provided in the tabulation of results. The overall cost ($J = 28.14$) is low and indicates an excellent fit. The Cramér-Rao bounds and insensitivities meet the guidelines from [25] and indicate a highly accurate model with high confidence. The model structure outlined in Table 3.2 yielded the best balance for cost, Cramér-Rao bounds, and insensitivities. The high order roll response transfer function shown in equation (3.16) was extracted from the identified state space model and shows good modal agreement with that identified from NAVFIT. One will notice in the roll rate response of Fig. 3.6 that there is a high frequency ($>$10 rad/s) gain rise of approximately +2dB that is not captured by the model. The low overall cost means this model can support flight control design, but consideration of this gain difference should be included in the roll autopilot gain margin requirements.

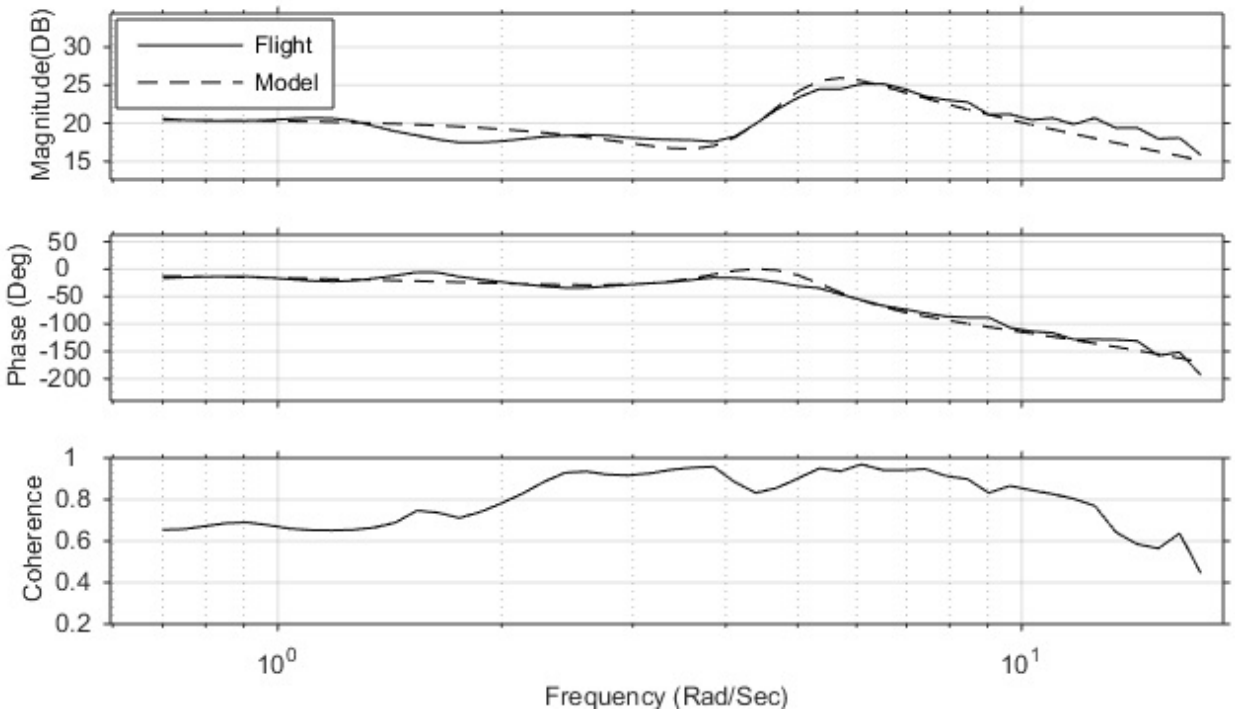

Figure 3.7: Roll rate response state space model matching ($J = 37.4$).

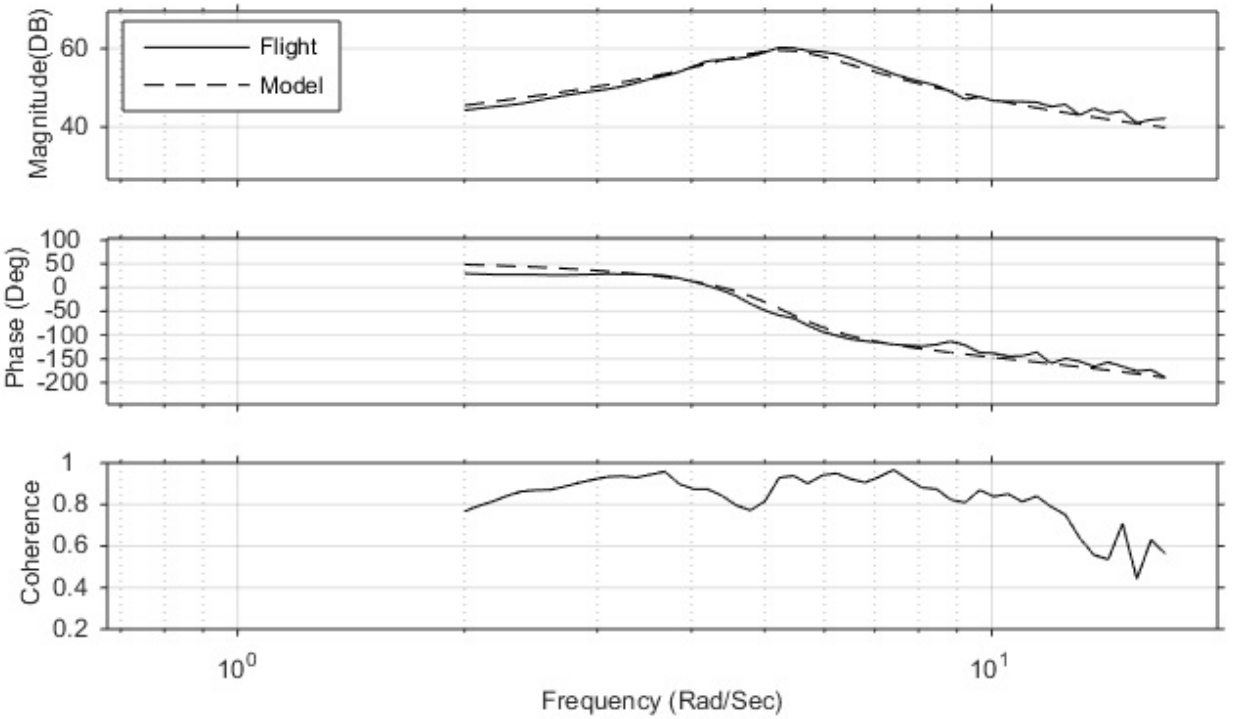

Figure 3.8: $\dot{v}$ response state space model matching ($J = 54.5$).

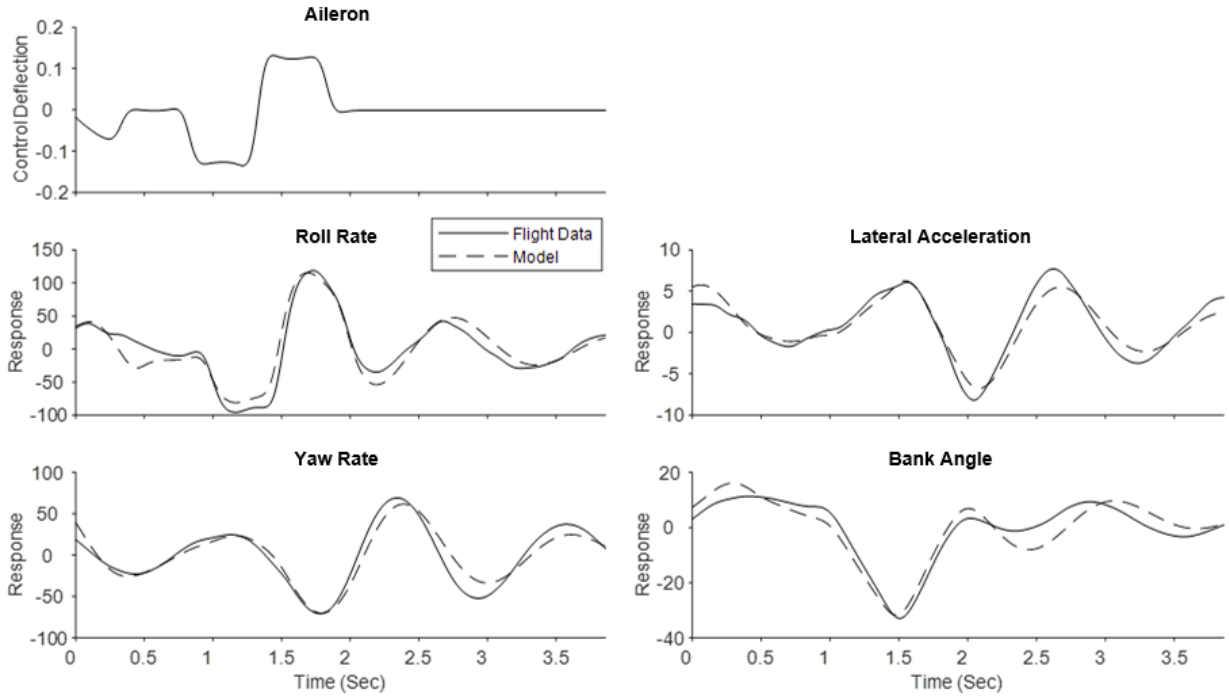

Figure 3.9: Time response state space model verification.

$$\begin{bmatrix} \dot{v} \\ \dot{p} \\ \dot{r} \\ \dot{\phi} \end{bmatrix} = \begin{bmatrix} -0.40 & 6.97 & -56.18 & 32.00 \\ -0.64 & -7.55 & 3.28 & 0 \\ 0.32 & -1.20 & -1.13 & 0 \\ 0 & 1 & 0.11 & 0 \end{bmatrix} \begin{bmatrix} v \\ p \\ r \\ \phi \end{bmatrix} + \begin{bmatrix} 0 \\ 119.7 \\ 0 \\ 0 \end{bmatrix} \delta_a(t-0.10) \tag{3.15}$$

$$\frac{p}{\delta_a} = \frac{119.7s(s^2+2(0.198)4.32s+4.32^2)e^{-0.1s}}{(s-1/9.62)(s+1/0.13)(s^2+2(0.15)5.22s+5.22^2)} \tag{3.16}$$

Finally, the flight test data is compared with the simulation data generated using the identified SS model, shown in Fig. 3.9. Good matches can be observed for the measurements. The frequency domain comparisons of the flight data, first order system, high order system, and state space model are shown in Fig. 3.10.

Table 3.2: State space parameters

Parameter	Value	Cramér-Rao, %	Insensitivity, %
L_p	-7.55	10.16	1.46
L_r	3.28	19.34	5.94
L_v	-0.64	10.77	2.50
N_p	-1.198	8.16	1.89
N_r	-1.13	16.89	3.50
N_v	0.32	4.08	1.02
Y_p	0.97	12.69	3.85
Y_r	0.92	24.29	6.81
Y_v	-0.40	6.18	1.54
L_{δ_a}	119.7	7.02	1.02
τ_{delay}	0.10 s	4.95	1.66
U_0	57.10 ft/s	NA	NA
W_0	6.00 ft/s	NA	NA

*Y_{δ_a} was dropped during model structure determination

3.6 Controller Optimization and Analysis

This section describes the process for controller gain determination based on the identified models and controller design specifications. A two-step process is performed with the first step focusing on the initial controller gain selection and model validation, and the second step focusing on analysis based controller gain finalization.

3.6.1 Initial Controller Gain Selection and Model Validation

The initial gain set was selected for comparing the flight data of the closed loop system with the simulated data using the identified high order or state space models. The controller objective is to keep the GM/PM within a stable range while maximizing the ω_c and DRB for better turbulence rejection. This was to create a fast acting controller that would reject turbulence and provide a stable gain set for frequency domain analysis. Constraints for each controller specification in Table 3.1 are empirically selected based on experimental flight data from the KHawk 55 UAS. The selected specifications are shown in Table 4.1. Note that these specifications can be potentially

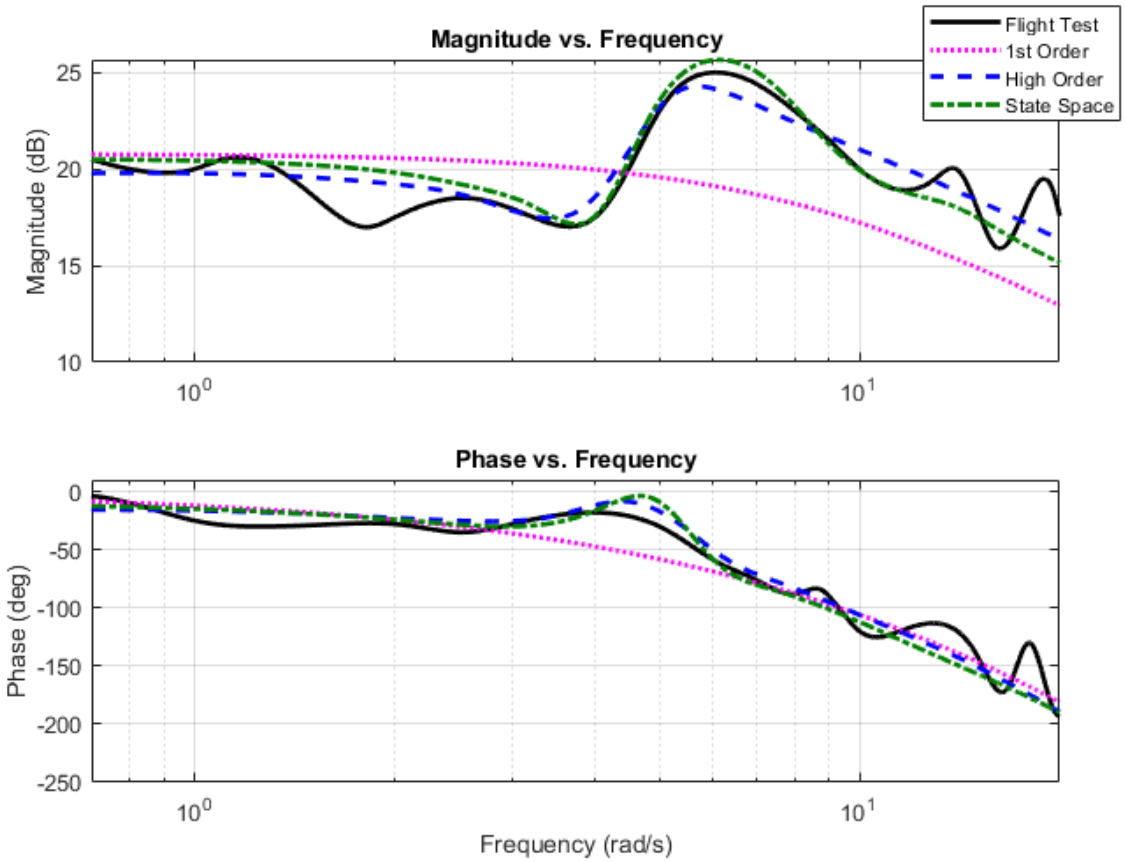

Figure 3.10: Open loop model comparisons.

extended to small UAS with a similar weight and wingspan.

Table 3.3: Controller design specification ranges for KHawk 55 UAS

Domain	Loop	Specification	Range
Time	Roll Tracking Loop	Rise Time	$0.2 < t_r < 0.7$ s
		Damp. from Overshoot	$\zeta > 0.60$
		Settling Time	$t_s < 4$ s
Freq.	Actuator Broken Loop	Gain Margin	GM > 5.5 dB
		Phase Margin	PM > 45 deg.
		Crossover Frequency	$2.25 < \omega_{cr} < 9$ rad/s
	Meas. Dist. Rej. Loop	Dist. Rej. Bandwidth	DRB > 1.2 rad/s
		Dist. Rej. Peak	DRP < 5.5 dB

Given the desired controller specifications, gains can be iteratively simulated until a desirable gain set has been chosen. The initial gain chosen for controller optimization is shown in Fig. 3.11 ($K_p = 0.42$, $K_d = 0.046$). The calculated controller parameters for other PD gains using the state

space model are also shown in Fig. 3.11. The gain and phase margin graphs show that the initial gain set is within the stable bounds (Table 4.1). The ω_c, DRB, and DRP for the initial gain set are also within the allowable ranges. The gain set was chosen to have a large ω_c and DRB but sacrifices some damping performance for a larger ω_c and DRB.

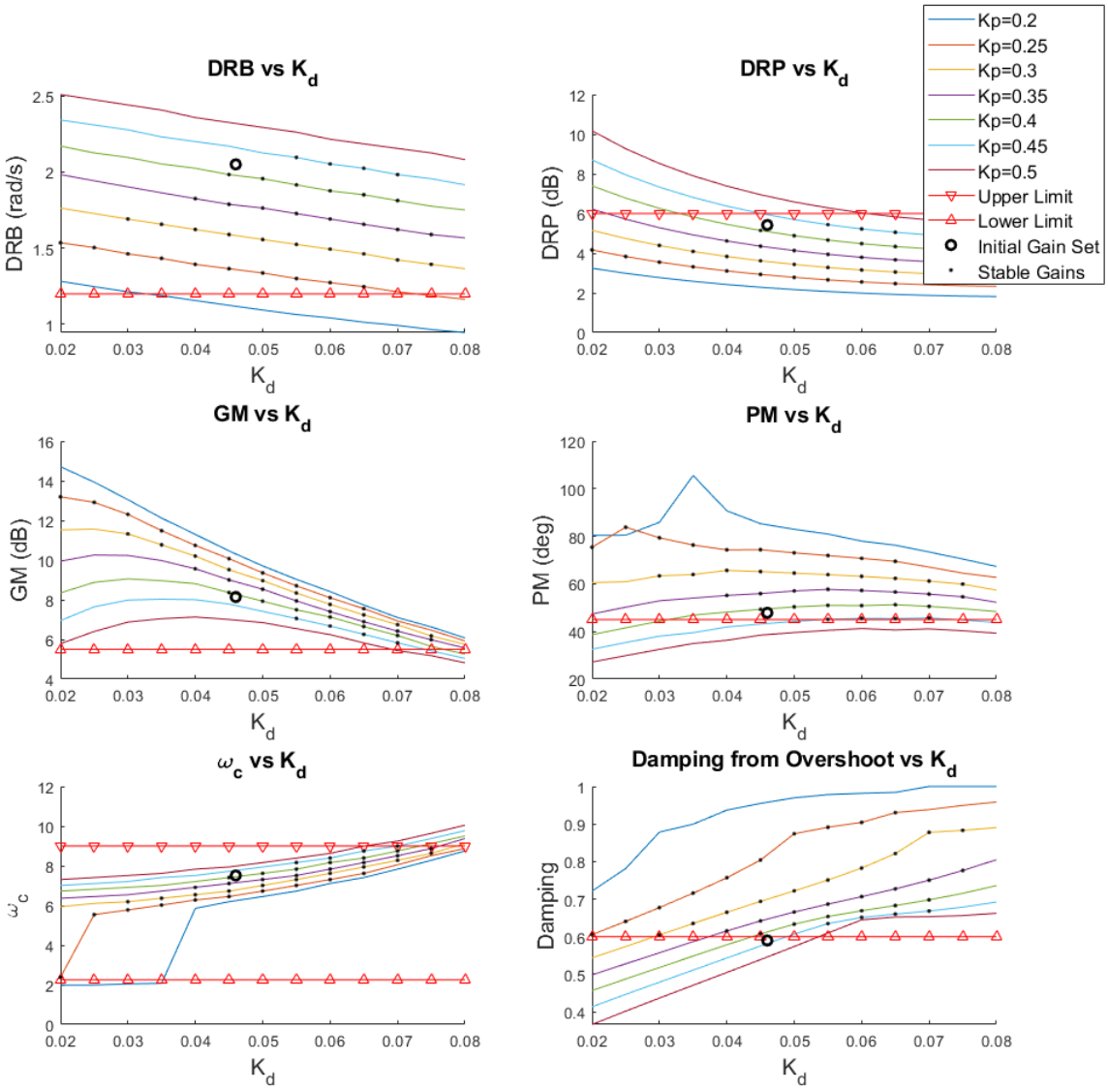

Figure 3.11: Design parameters for different PD gains using the state space model.

The gain set is first analyzed in simulation using frequency and time domain data with both state space and high order models. The frequency and time domain results for the selected gain set using the two different models are shown in Table 3.4. Both models show similar results with

slight variations in design parameters. The gain/phase margins can be visualized in the Nichols margins plots showed in Fig. 3.12.

Table 3.4: Simulation results from high order and state space models using the initial gain set

Model	DRB (rad/s)	DRP (dB)	Response Time (s)	ω_{cr}	GM (dB)	PM (deg)
High Order	2.05	5.44	0.31	7.81	6.89	51.96
State Space	2.05	5.42	0.31	7.62	8.11	47.58

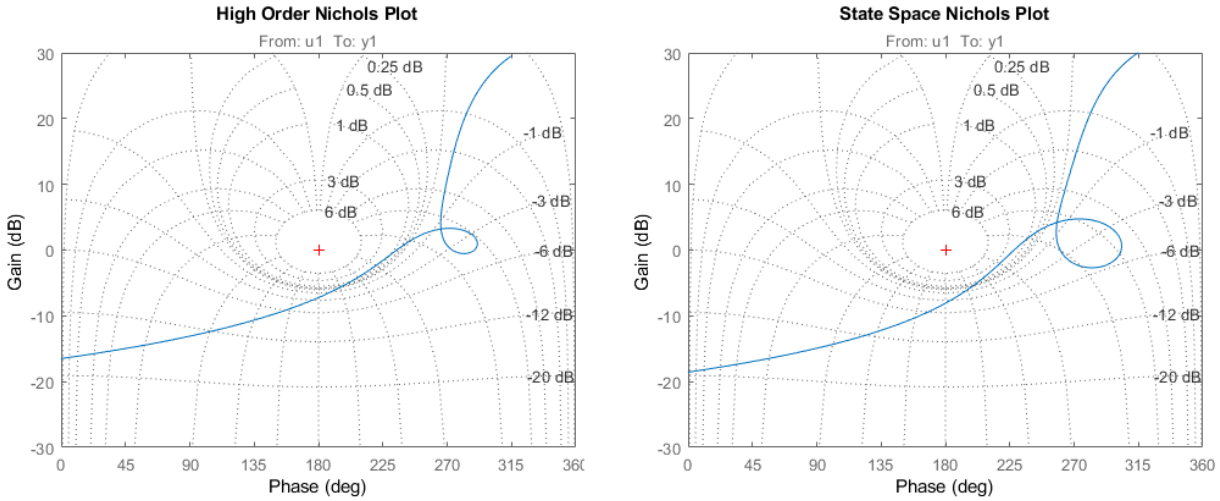

Figure 3.12: Nichols margins plots for calculated PD controller (initial gain set).

3.6.2 Analysis Based Controller Gain Finalization

After the simulation and flight validation of the initial gain set, the next step is to finalize the controller gain. Given the close matching for the state space model (as shown in Sec. 7.A Table 3.8), it is used for the controller gain selection. Three final gain sets are selected (legacy, conservative, and aggressive) for simulation and flight comparison of turbulence rejection. The legacy controller was determined through manual tuning and has a low ω_c, low DRB, and moderate damping. The

conservative controller has a moderate ω_c, moderate DRB, and moderate damping. The aggressive controller has a high ω_c, high DRB, and moderate damping. These gain sets were chosen to have good stability while maintaining a consistent damping ratio. This was to ensure that as the ω_c and DRB were increased, the overshoot from the damping would not negatively interact with the turbulence by providing more overshoot.

Gains are shown in Table 3.5 with their respective damping ratio, ω_c, and DRB. In addition, the three selected gain sets are tested using the state space model to simulate the turbulence rejection performance. The Dryden model is used to simulate wind turbulence, and the plot of the wind turbulence effect on the KHawk 55 UAS is shown in Fig. 3.14 for straight and level flight. Note that the legacy gain set appears to reject turbulence less than the other two. This is due to the ω_c and DRB being higher for the conservative and aggressive gain sets. The RMS error for each gain set during a 20-second zero roll tracking test is shown in Table 3.6 and the RMS error versus K_p and K_d can be visualized from the plot in Fig. 3.13. The yellow edge color denotes the desired gain set region based on the chosen design parameters shown in Fig. 3.11. The red region shows gains with a DRB greater than 2 rad/s, and the black region shows gains with a GM/PM greater than 6.5 dB/55 degrees, and a rise time greater than 0.4 seconds. These ranges where chosen to help limit the ranges of the conservative and aggressive gain sets based on user preference (turbulence rejection). The user's selection of this multi-objective graph-based tuning method can further constrain gain parameters based on the desired controller's mission purpose. For instance, if the user's UAS is to be used for mapping or remote sensing with downward facing cameras on calm days, the user may choose to constrain the gain set to have a slower rise time and higher damping for a smoother flight. For this chapter, different gains could have been chosen within the regions but were chosen towards the top of the graph to aid in better turbulence rejection performance.

The multi-objective tuning method proposed in this chapter is designed around the KHawk 55 UAS platform. However, the multi-objective graph-based tuning rule presented here should provide relatively close stability margin ranges for similar aircraft. The stability margin ranges were determined primarily from flight data but are also constrained based on other parameters like

the overshoot and DRB. It should be noted that stability design parameter ranges of other small fixed-wing UAS may vary slightly. This can be determined through flight test by trying different gain sets, and by setting personalized controller parameter ranges such as rise time, settling time, and overshoot. Also, the stability of the aircraft is heavily dependent on the flight velocity. A flight envelope with a large velocity range can be stable at one velocity using the selected gain set but unstable at another. If the selected gain set is tuned at cruise velocity and is near the limit of its stable margins, an increase in speed could result in those stability margins decreasing resulting in a more unstable controller. This should be taken into consideration by the user of this multi-objective graph-based tuning rule.

Table 3.5: Controller gain sets for simulation

Gain set	K_p	K_d	GM	PM	ζ	ω_{cr}	DRB
Legacy	0.29	0.032	11.29	65.92	0.62	6.20	1.63
Conservative	0.35	0.06	7.40	57.22	0.70	7.83	1.69
Aggressive	0.45	0.06	6.68	45.53	0.65	8.39	2.05

Table 3.6: Roll tracking RMS error for simulated turbulence rejection.

Gain set	Legacy	Conservative	Aggressive
RMS error (deg)	1.22	0.99	0.91

3.7 UAS Flight Validation

UAS flight tests were performed on two separate days for initial system and controller validation, and final controller validation in turbulent conditions.

3.7.1 Initial System and Controller Validation Flight Test

The initial gain set was tested on a calm to moderately windy day using the KHawk 55 UAS by flying step responses and frequency sweeps implemented as disturbances into the control system

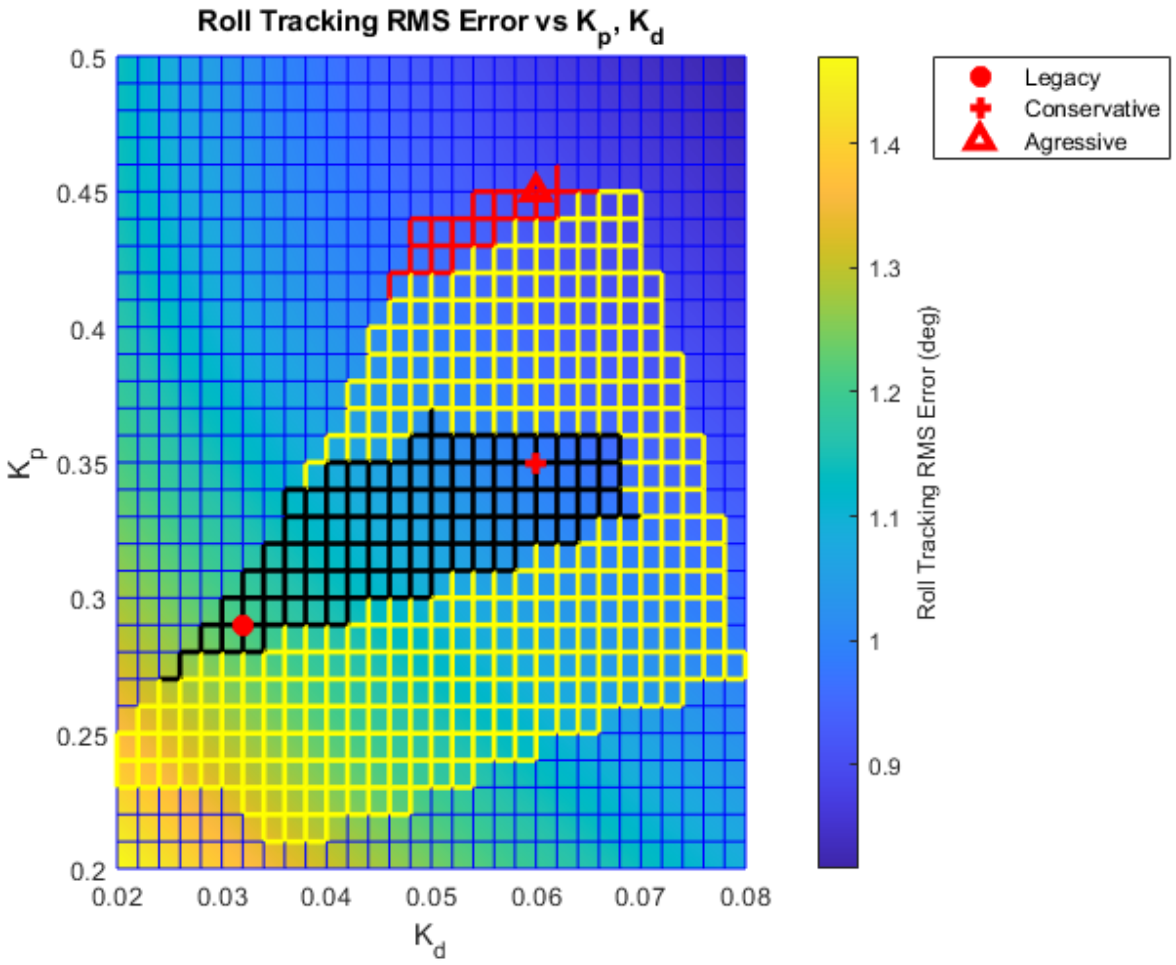

Figure 3.13: RMS error vs K_p and K_d. Yellow region denotes controller design space.

as shown in Fig. 3.2. The step response was set to track 20 degrees roll for the initial gain set as shown in Fig. 3.15. It can be observed that both the high order and state space models accurately depicts the step performance of the closed loop system. The frequency sweeps were performed for the actuator broken loop and measurement disturbance rejection loop for analysis. An example of the frequency sweep data for the actuator broken loop analysis is shown in Fig. 3.16. Two sets of sweeps for each gain and scenario (actuator broken loop and measurement disturbance rejection loop) were flown so that an average could be calculated. The coherence plot of the broken loop flight data for the initial gain set is shown in Fig. 3.17. It can be observed that the data is trustworthy for disturbance frequencies ranging from 1 to 20 rad/s.

Fig. 3.18 shows an example of the time domain data for the DRB analysis. Fig. 3.19 shows

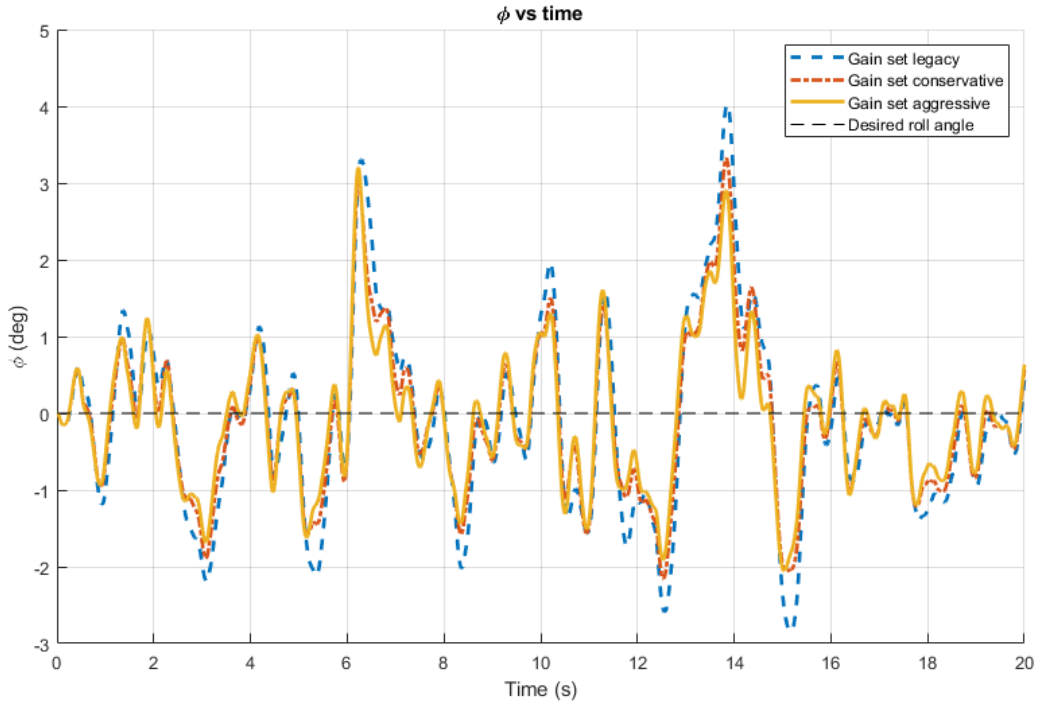

Figure 3.14: Effect of Dryden turbulence simulation on KHawk 55 UAS roll angle.

the coherence for the flight data analysis and the frequency domain results. In summary, both the high order and state space model showed good results for the DRB and DRP in comparison with flight test results. Key specifications for each gain set (e.g. DRB, DRP) are identified from flight test data and shown in Table 3.7. The difference for the identified specifications obtained from simulated and flight data are further calculated and shown in Table 3.8. In summary, the controllers using high order and state space models showed good consistency between simulated and flight test results for the initial gain set.

Table 3.7: Trial results for flight test

Gain set	DRB (rad/s)	DRP (dB)	Response Time (s)	Over-shoot (%)	ω_{cr}	GM (dB)	PM (deg)
Initial	2.38	5.05	0.29	7.25	7.81	7.63	49.78

The error comparison between the two identified high order SISO and state space SIMO mod-

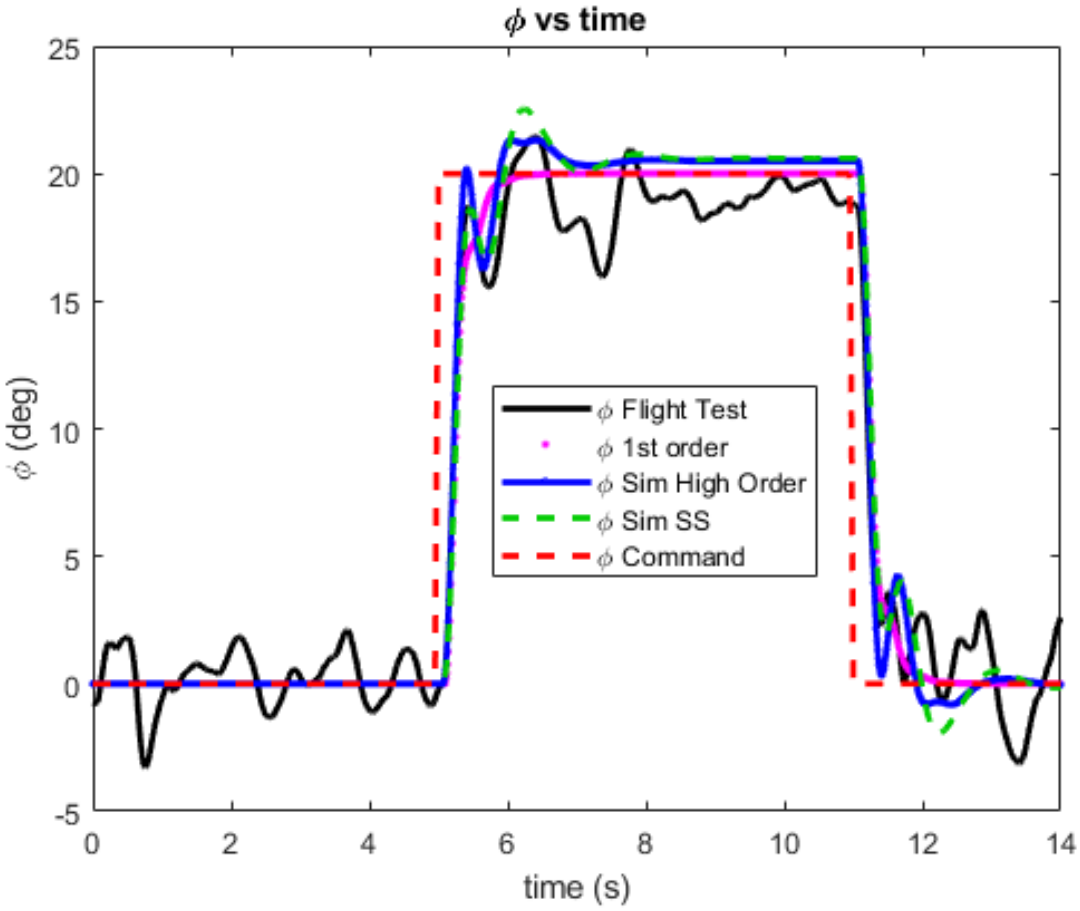

Figure 3.15: Step response for the initial gain set.

Table 3.8: Percent error results for initial gain set using high order and state space models

Model	DRB	DRP	Response Time	ω_{cr}	GM	PM
High Order	13.75 %	7.82 %	6.90 %	0 %	9.72 %	4.38 %
State Space	13.75 %	7.36 %	6.90 %	1.33 %	6.26 %	4.42 %

els showed good consistency. The percent errors in Table 3.8 showed slightly better agreement between flight data and simulated closed loop response using the state space model for the initial gain set. In summary, both models provided close estimates of the aircraft responses when compared with flight test data.

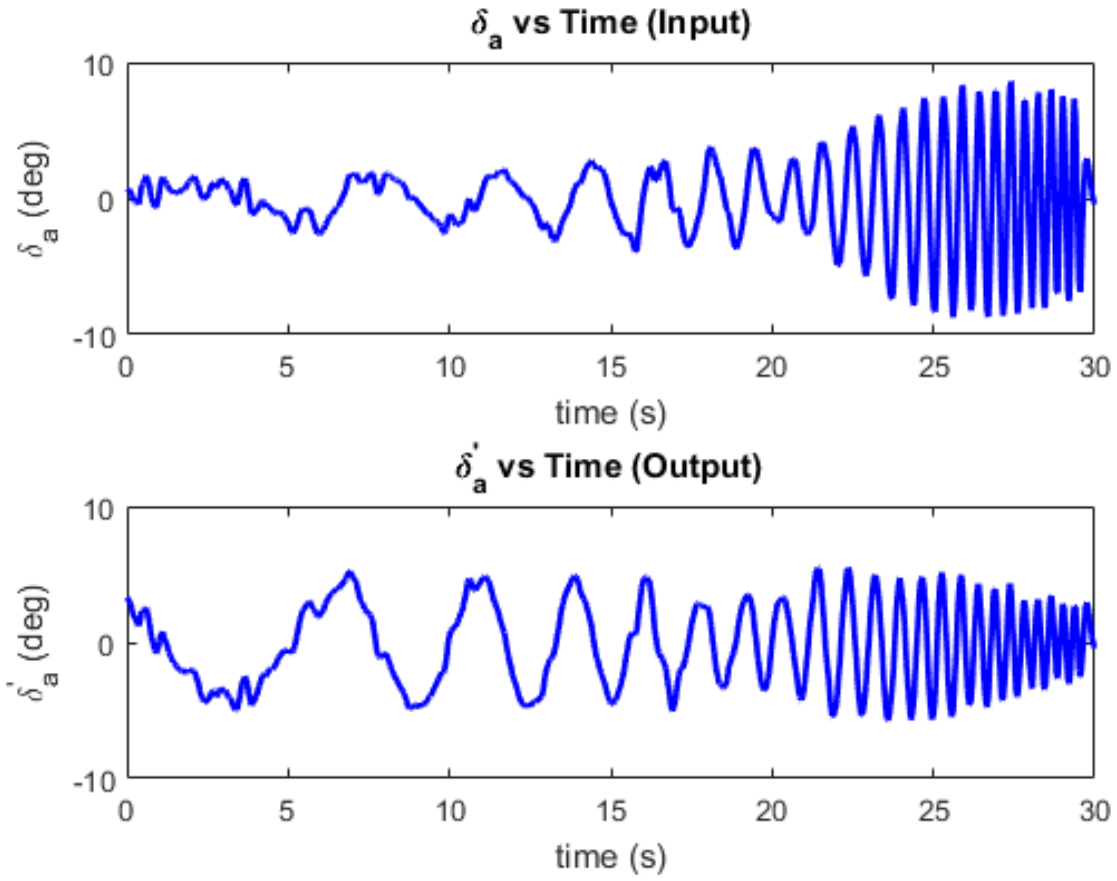

Figure 3.16: Input vs output time domain data for actuator broken loop.

3.7.2 Final Controller Validation in Turbulence

The turbulence rejection flight test consisted of flying the three gain sets shown in Table 3.5 during mildly windy conditions (wind was 2.7 to 4.5 m/s) two times during one flight. The KHawk 55 was flown in a racetrack pattern with the plane facing into the wind for each straight and level pass. The gain set was changed after every straight and level roll tracking pass so that the gains could be tested as close to each other as possible. This was to ensure that the wind and turbulence conditions would be comparable for each tested gain set. Trial data from the two flight tests are shown in Fig. 3.20 and Fig. 3.21. The RMS error for each flight test is shown in Table 3.9. It can be observed that as the gain sets damping and ω_c are increased, the tracking accuracy improves. However, increasing these parameters beyond a certain point will cause the damping ratio to go

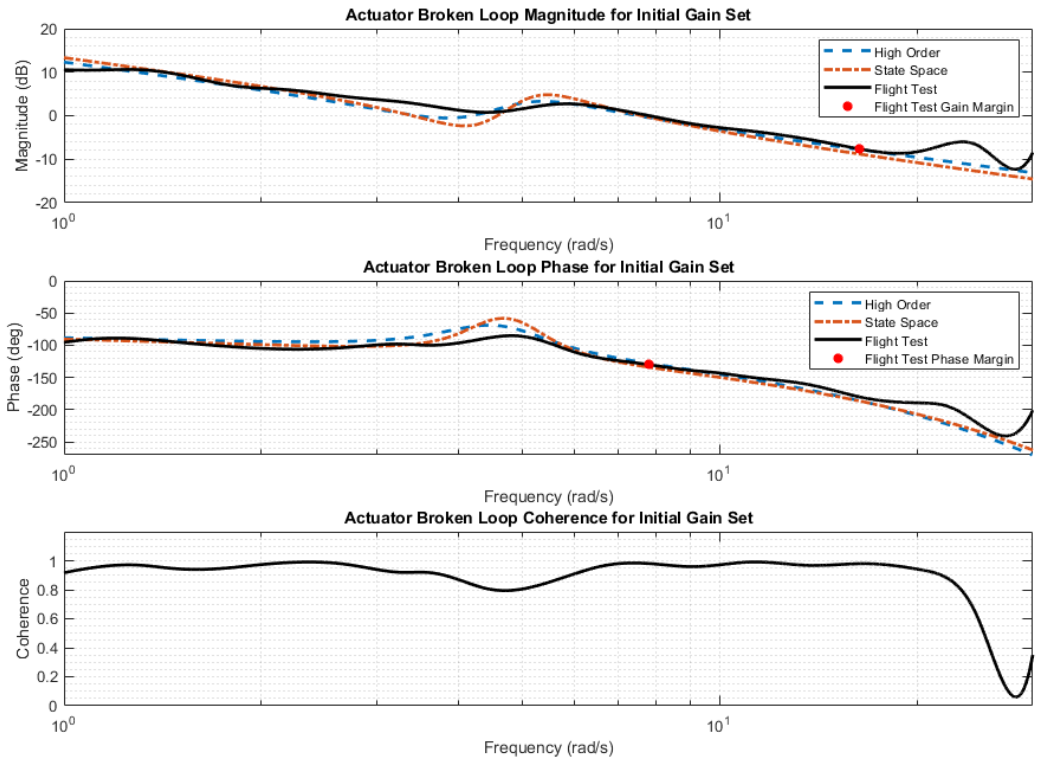

Figure 3.17: Gain/phase margin comparison using initial gain set (flight test vs. simulation data).

down and the instability of the system to rise. This can be controlled through the constraining of the gain and phase margins as well as the damping ratio.

Table 3.9: Roll tracking RMS error for flight test 1 and 2

Gain set	Test 1 (deg)	Test 2 (deg)
Legacy	2.30	2.02
Conservative	1.81	1.44
Aggressive	1.56	1.09

In summary, the designed controller performed similarly in simulation and in real flights. Some of the differences between the real flight data and high order and state space models for GM/PM and DRB/DRP, could be due to variations in cruise velocity and Θ_0 with the real flight data. As mentioned in section V.B.1., choosing the correct Θ_0 is important to calculating the state space

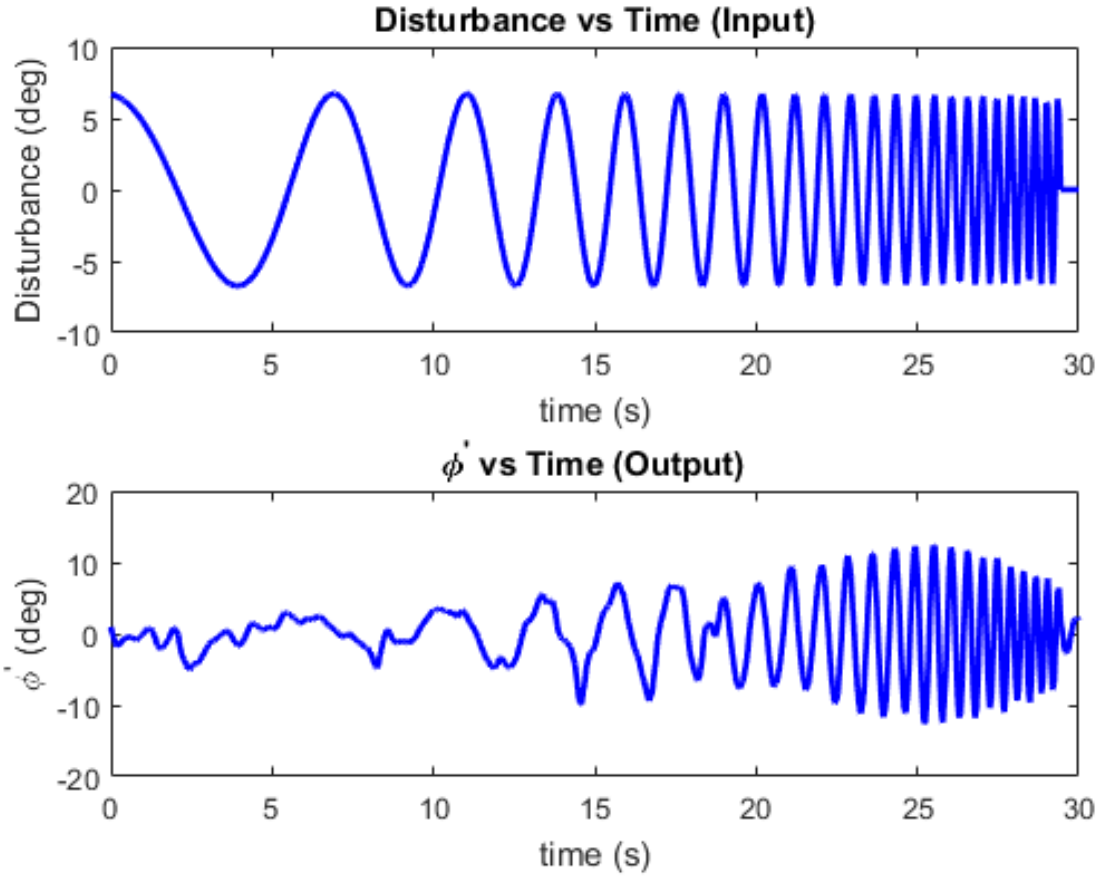

Figure 3.18: Input vs output time domain data for the DRB.

variables but it is also important to maintain a consistent cruise speed to keep the Θ_0 constant. The broken loop flight data had some variations in cruise speed resulting in a higher velocity for the sweeps by as much as 3 m/s. This is probably why the high order and state space models appear slightly different from the real flight data in Fig. 3.17. If the broken loop flight tests had better consistent cruise velocity and Θ_0, results would likely be closer.

3.8 Discussion and Conclusion

In this chapter, a coupled system identification and controller design framework is proposed for the roll tracking control problem. A new KHawk 55 tuning rule is proposed based mostly on frequency response requirements and certain time domain requirements for stability and performance

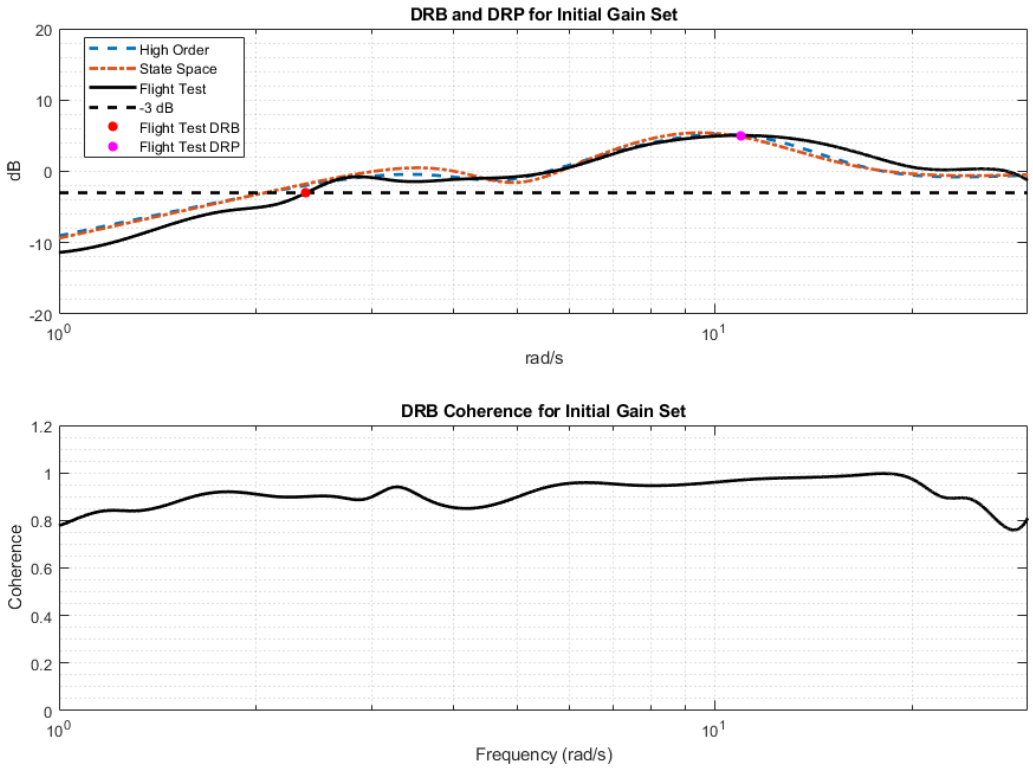

Figure 3.19: DRB/DRP comparison using initial gain set (flight test vs. simulation data).

purposes. Detailed flight data analysis showed the effectiveness of the proposed method in identifying the lateral dynamic model and validating the design of the KHawk 55's roll controller. Some of the differences between the real flight data and high order and state space models for GM/PM and DRB/DRP, could be due to variations in cruise velocity and Θ_0 with the real flight data.

In conclusion, the methods presented in this chapter for a coupled system identification and multi-objective graph-based tuning rule allowed for the successful creation of turbulence rejecting controllers that had similar controller specification values and turbulence rejecting qualities as the simulated controllers using the same gain sets. Furthermore, the coupled system identification and multi-objective graph-based tuning rule allowed for good estimation of the controller's stability ranges before flight testing the controller. This ability to predict the controller's specifications and stability ranges before flight, removes the hazardous nature of guessing a stable gain set through manual tuning and can allows for safer gain selection for unique flight scenarios such as high

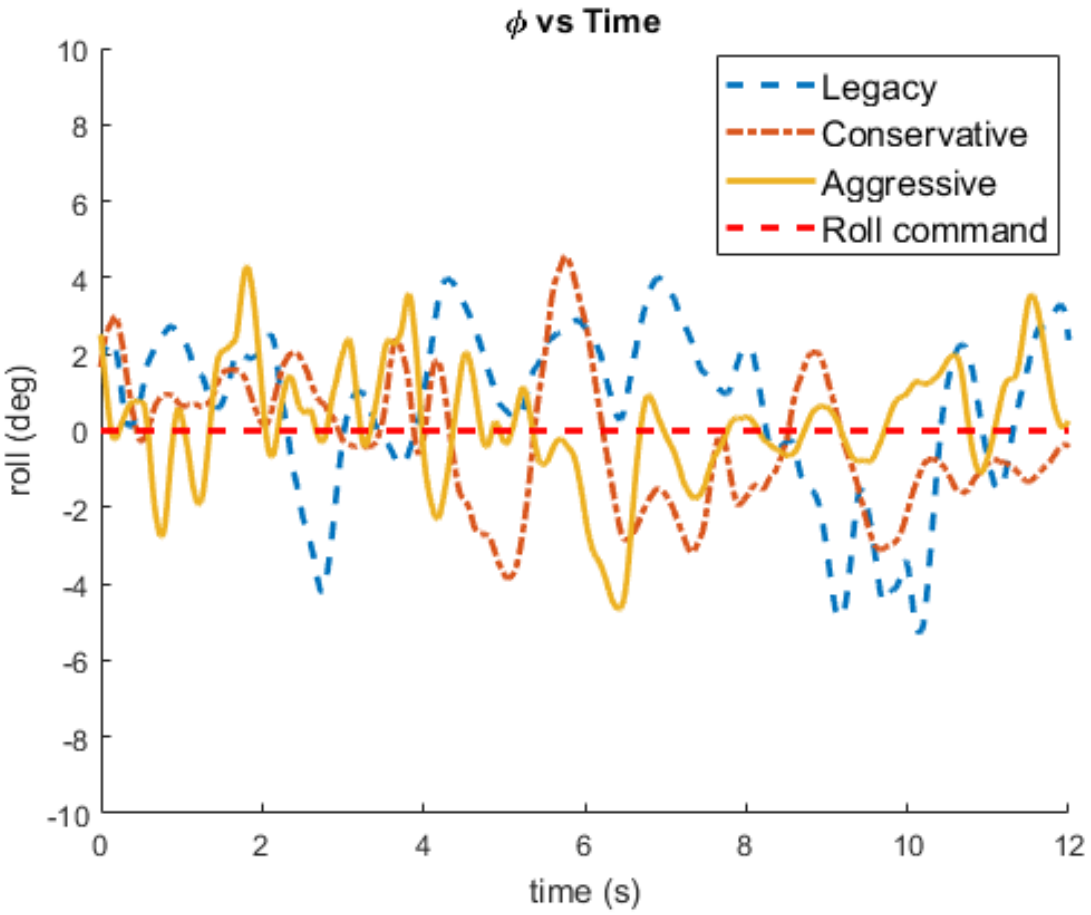

Figure 3.20: Gain trial 1 for turbulence rejection.

turbulence flight.

Potential future research directions include UAS flight controller tuning under different turbulence conditions such as fire turbulence, and adding an extra feedback loop of sideslip angle to improve the roll and yaw coupling.

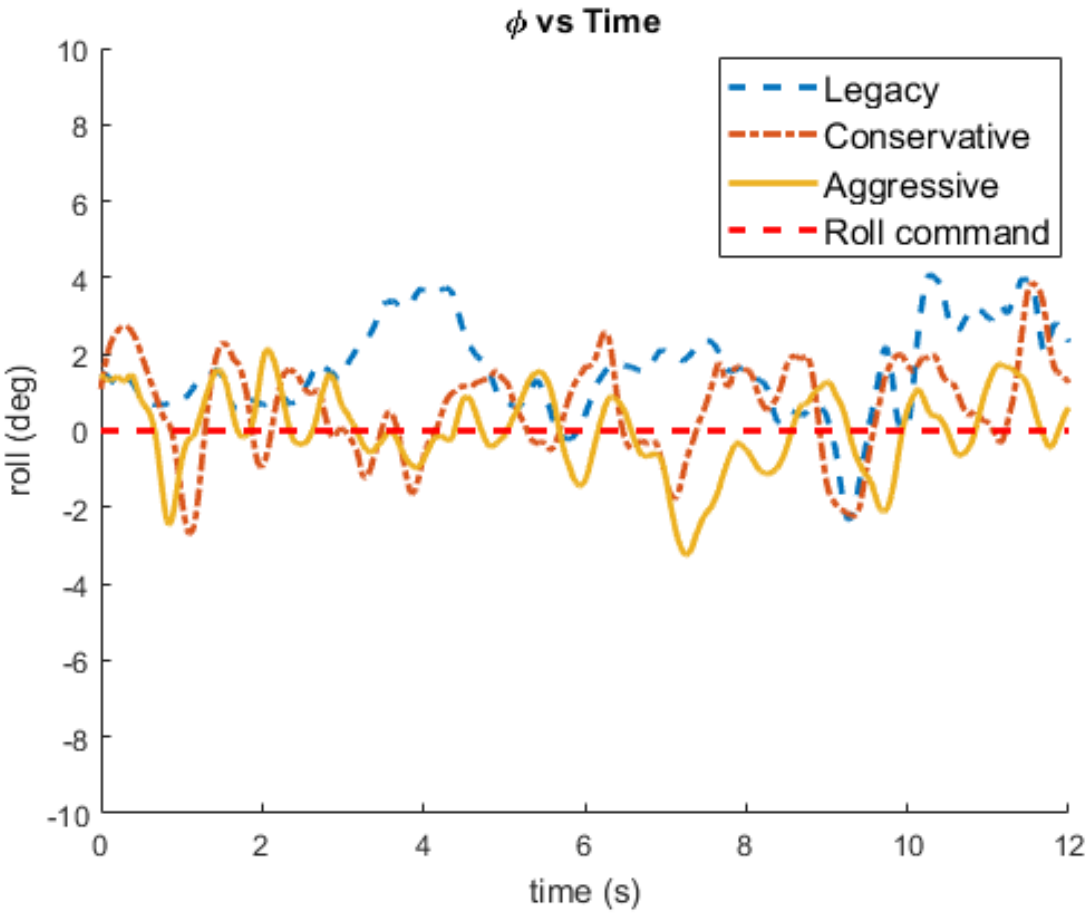

Figure 3.21: Gain trial 2 for turbulence rejection.

Chapter 4

Lateral Fractional Order Controller Design and Tuning

Abstract

Stable and robust flight controllers are critical to Unmanned Aircraft Systems (UASs) especially for demanding missions in strong turbulence. This chapter introduces a new fractional order controller (FOC) design and tuning method for roll tracking of a flying-wing UAS. The proposed FOC is designed based on the open loop lateral dynamics of the KHawk 55 UAS. Multiple control objectives are considered including Gain Margin (GM), Phase Margin (PM), Disturbance Rejection Bandwidth (DRB), Disturbance Rejection Peak (DRP), overshoot percent (O%), and settling time (t_s), etc. The controllers are tuned and optimized using a genetic algorithm. The proposed fractional order controller is validated in simulation using a high-order lateral dynamic model, which was identified from the KHawk 55 UAS. The developed fractional order controller showed better performance in multiple scenarios with different specification requirements when compared with the classical PID controller.

4.1 Introduction

Unmanned aircraft systems (UASs) are increasingly being used in challenging missions such as storm meteorological measurements, wildfire surveillance [8], volcanic activity monitoring [31], and urban air mobility, where unpredictable and strong turbulence may be encountered. Most UASs use the classical proportional, integral, and derivative (PID) controllers for flight stabilization [7; 6; 4; 32]. Researchers have also used more advanced controllers such as the H_∞ controller

or linear quadratic regulator (LQR) [33]. New advancements in avionics hardware, improved aircraft dynamic models, and better sensors for wind estimation, make it possible to develop more robust controllers capable of aiding UASs in navigating challenging turbulent environments [34; 35].

Advanced controllers such as Fractional Order Controllers (FOCs) utilize fractional calculus to increase the design space compared to integer order PID controllers. The increased design space allows for more flexibility in controller tuning and in theory can produce a more robust controller with greater stability and more accurate tracking. A Fractional Order Proportional and Integral (FOPI) lateral controller was shown to have a better roll tracking performance than an integer order PI controller using a cascaded controller structure for a small flying-wing UAS [36]. Other research showed better FOPI controller performance than a traditional PID controller tuned by modified Ziegler-Nichols rule for a quad-copter VTOL UAS [37]. FOC also allows for greater flexibility in loop shaping in consideration of controller robustness specifications from the frequency domain. FOCs have been designed and compared with an H infinity controller for active magnetic bearing systems [38]. However, few works can be found on FOC flight controller design using both time domain and frequency domain specifications.

Controller robustness analysis of the broken loop (at actuator) and the disturbance rejection loop (at sensor feedback) has been widely used on manned aircraft [18]. Specifications from the broken loop include gain margin (GM), phase margin (PM), and the crossover frequency (ω_c). The GM and PM relate to the stability of the controller and their limits can be empirically determined [18]. The disturbance rejection loop provides information on the aircraft response to disturbances. In this chapter, the disturbance rejection loop shows the effect of roll angle disturbances on the lateral controller. The disturbance rejection bandwidth (DRB) and disturbance rejection peak (DRP) describe the ride quality and performance of the controller. The DRB relates to the speed at which the controller can correct for a disturbance and the DRP represents the largest response in magnitude to the disturbance [39; 40; 41; 18]. These specifications can be potentially used in fractional order flight controller design.

This chapter introduces a new FOPID based lateral loop flight controller design and tuning

method. The gain optimization is achieved using a genetic algorithm, based on control stability and performance requirements in both time domain and frequency domain for a small flying-wing UAS. The main contribution of this chapter is the introduction and demonstration of a GA optimized FOC for the lateral open loop dynamics of a flying-wing UAS. This chapter presents the first FOC design over the high order open-loop lateral dynamics of a fixed-wing aircraft. The GA based optimization is accomplished by the introduction of a multi-objective cost function that includes aircraft stability margins and turbulence rejection parameters for controller gain determination. The cost function can also be adjusted based on specific UAS mission requirements.

This chapter is organized as the following. Sec. 4.2 focuses on the problem statement and aircraft lateral dynamic model. Then, FOC basics are introduced in Sec. 4.3. Sec. 4.4 discusses FOPID controller design and tuning. The KHawk UAS platform and the associated model are explained in Sec. 4.5. And the controller simulation, tuning, and analysis results are presented in Sec. 4.6. Finally, the conclusion is made in Sec. 4.7.

4.2 Problem Statement

This chapter focuses on the roll tracking control problem for a fixed-wing UAS. Different lateral dynamic models can be identified and used for control of manned and unmanned aircraft. This chapter uses a 4th order single-input single-output (SISO) δ_a–p model for controller design, tuning, and analysis [14; 25].

$$\frac{p}{\delta_a} = \frac{L_{\delta_a} s(s^2 + 2\zeta_\phi \omega_{n_\phi} s + \omega_{n_\phi}^2) e^{-\tau_d s}}{(s + 1/\tau_s)(s + 1/\tau_r)(s^2 + 2\zeta_{dr}\omega_{n_{dr}} s + \omega_{n_{dr}}^2)}, \tag{4.1}$$

where τ_r is the roll mode constant, τ_s is the spiral mode constant, τ_d is the time delay constant, ζ_{dr} and $\omega_{n_{dr}}$ are the Dutch roll mode damping ratio and natural frequency, and ζ_ϕ and ω_{n_ϕ} are the Dutch roll coupling zeros damping ratio and natural frequency. The p to ϕ conversion is shown in

equation (4.2) for the final roll attitude tracking problem.

$$\frac{\phi}{\delta_a} = \frac{1}{s} \quad \frac{p}{\delta_a}. \tag{4.2}$$

This SISO model structure is selected due to its accurate representation of the UAS lateral loop dynamics around the cruise trim point. Good agreement between the model and flight data has been observed [42].

Multiple control objectives will be considered for our controller design, including:

- time domain specifications such as rise time, overshoot, settling time, roll tracking error in turbulence, actuator root mean square (RMS), etc;
- frequency domain specifications such as gain margin, phase margin, cross-over frequency, disturbance rejection bandwidth, disturbance rejection peak, etc.

Detailed specifications will be explained in Sec IV.

4.3 Fractional Order Controller Basics

Fractional order calculus is a process of differentiation or integration of a non-integer fundamental operator ${}_aD_t^r$, where r is the order of the operation and can be a complex number [43], and a and t are the limits of the operation. The operator is described in equation (4.3).

$${}_aD_t^r = \begin{cases} d^r/dt^r & Re(r) > 0, \\ 1 & Re(r) = 0, \\ \int_a^t (dt)^{-r} & Re(r) < 1. \end{cases} \tag{4.3}$$

4.3.1 Definition of Fractional Differentiation and Integration

There are several definitions for fractional operators, including the Riemann-Liouville (RL) definition, the Caputo definition, and the Grünwald-Letnikov definition. The RL definition is one of the more commonly used definitions and is shown in equation (4.4) [44; 45].

$$ {}_aD_t^r f(t) = \frac{1}{\Gamma(n-1)} \frac{d^n}{dt^n} \int_a^t \frac{f(\tau)}{(t-\tau)^{r-n+1}} d\tau. \tag{4.4} $$

The integral is given for $(n-1 < r < n)$ and Γ is the gamma function. The Laplace transform for the RL fractional derivative is shown in equation (4.5).

$$ \int_0^\infty e^{-st} {}_0D_t^r f(t) dt = s^r F(s) - \sum_{k=0}^{n-1} s^k {}_0D_t^{r-k-1} f(t) \Big|_{t=0}, \tag{4.5} $$

where s denotes the Laplace transform variable.

4.3.2 Oustaloup Approximation

There exist different methods to convert a fractional order Laplace transform equation into an integer order Laplace transform equation, for system or controller implementation purposes. The approximation used in this chapter is the Oustaloup approximation [46]. The Oustaloup approximation for a fractional order function s^r is given below, and is defined for a frequency range from ω_b to ω_h.

$$ G_{approx}(s) = V \prod_{k=-N}^{N} \frac{s + \omega_k^{'}}{s + \omega_k}. \tag{4.6} $$

N is a user specified integer number relating to the order of the approximated Laplace equation $(2N+1)$. The poles, zeros, and gains can be determined from the following equations:

$$ \omega_k^{'} = \omega_b \left(\frac{\omega_h}{\omega_b}\right)^{\frac{k+N+\frac{1}{2}(1-r)}{2N+1}}, \tag{4.7} $$

$$ \omega_k = \omega_b \left(\frac{\omega_h}{\omega_b}\right)^{\frac{k+N+\frac{1}{2}(1+r)}{2N+1}}, \tag{4.8} $$

$$ V = \left(\frac{\omega_h}{\omega_b}\right)^{-\frac{r}{2}} \prod_{k=-N}^{N} \frac{\omega_k}{\omega_k^{'}}. \tag{4.9} $$

4.4 Design and Tuning of Fractional Order Controller

This chapter examines the performance of a lateral fractional order flight controller for a small UAS, and provides a detailed comparison with a classical PID controller. The lateral controller is the inner-loop portion of the autopilot that deals with the roll tracking control of the aircraft. It requires stability and robust considerations such as turbulence rejection. The FOPID controller specifications used in this chapter follow a "KHawk tuning rule" proposed for integer order controller design [47; 42].

4.4.1 FOPID Structure

The general FOPID controller structure is shown below in equation (4.10).

$$C(s) = K_p + K_d s^{\alpha} + \frac{K_i}{s^{\lambda}}. \tag{4.10}$$

Because the controller for the KHawk 55 UAS in this chapter uses the roll rate feedback for the derivative portion, a different controller structure is used in this chapter. This FOPID controller structure is shown in equation (4.11).

$$C(s) = K_p + K_d s(s^{\mu}) + \frac{K_i}{s^{\lambda}}, \quad \mu = \alpha - 1. \tag{4.11}$$

Note that the derivative fractional order portion is placed in the roll rate feedback loop.

4.4.2 Gain Selection and Multi-Objective Optimization

The basic lateral controller system structure is shown in Fig. 3.2, including the lateral dynamics model, the actuator broken loop, and the measurement disturbance rejection loop. The controller specifications used for the KHawk tuning rule are shown in Table 4.1, which includes multiple objectives from time domain and frequency domain. Optimization algorithms such as the Genetic algorithm can be used to find the optimal gain set that meets all the specifications. The controller

specifications can be chosen empirically based on flight data or through other literary research [39]. For example, the limits for stability margins can be empirically determined. As the GM/PM values become smaller, fluctuations in airspeed and the wind can potentially result in more instability.

Table 4.1: Controller design specification

Specification	Range
Rise Time	$0.2 < t_r < 0.7$ s
Overshoot	O $< 10\%$
Gain Margin	GM > 5 dB
Phase Margin	PM > 40 deg.
Disturbance Rej. Bandwidth	DRB > 1 rad/s
Disturbance Rej. Peak	DRP < 5.5 dB

4.5 UAS Platform and Model

The KHawk 55 UAS was used for the model-based controller design and for simulation validation.

4.5.1 KHawk 55 Lateral Dynamic Model

A high order SISO model will be used in this chapter for FOPID controller design and is shown in equation (4.12). The model was identified using frequency domain methods through the CIFER commercial software [25]. A good match between the identified model and UAS flight data can be observed during a doublet aileron maneuver, shown in Fig. 4.1. Detailed system identification analysis regarding the KHawk 55 UAS can be found in [47; 42].

$$\frac{p}{\delta_a} = \frac{143.3s(s^2+2(0.23)4.16s+4.16^2)e^{-0.114s}}{(s-1/9.98)(s+1/0.103)(s^2+2(0.22)5.05s+5.05^2)}. \tag{4.12}$$

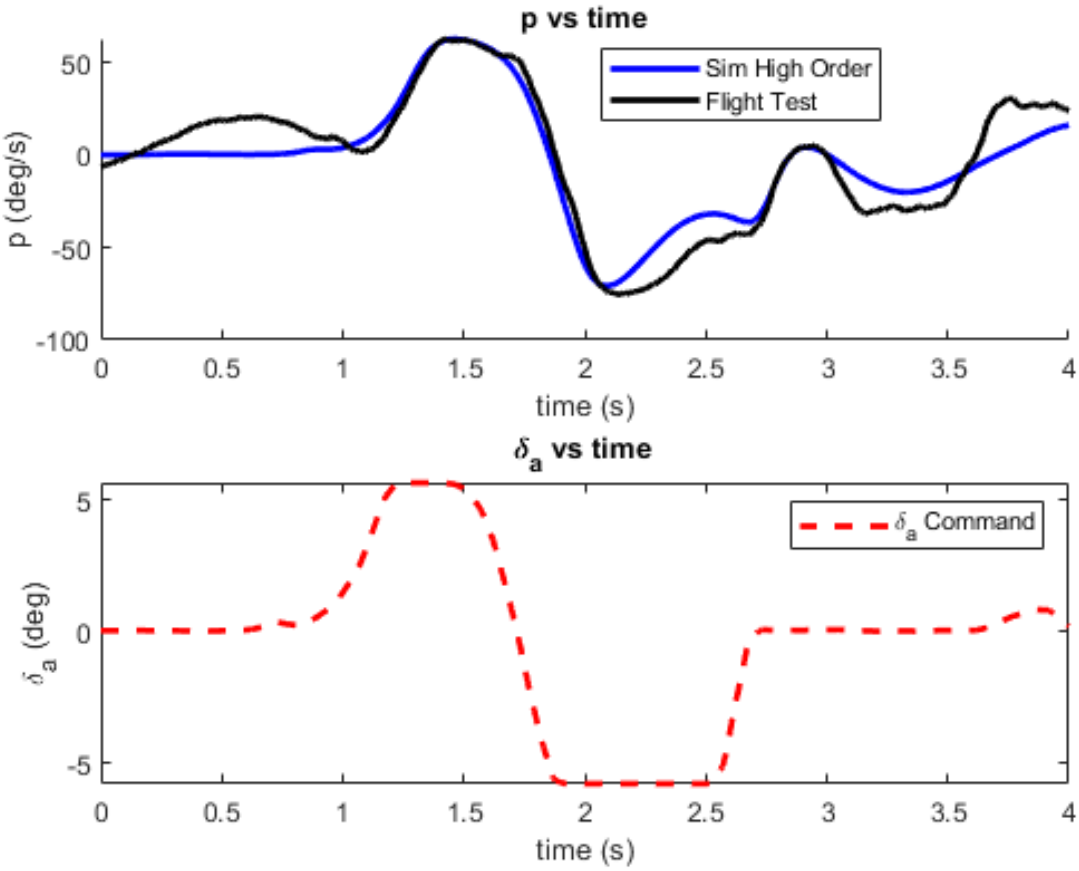

Figure 4.1: Flight data vs prediction from the high order lateral model during a doublet response.

4.6 Controller Simulation, Tuning, and Analysis

The controllers utilized for comparison in this chapter are a PID controller and a FOPID controller that are optimized using the same controller specifications given in Table 4.1, with the addition of turbulence rejection metrics. The optimization strategy is achieved using a genetic algorithm for both the classical PID controller and the FOPID controller.

4.6.1 Genetic Algorithm based Optimization

A GA is an evolutionary algorithm for optimizing unconstrained and constrained problems. The GA uses bio-inspired operators that include crossover, mutation, and selection [48]. The GA starts an iteration by creating a parent calculation with the given variables and creates children and mu-

tations from the initial calculation. As this process continues, the weight of the cost function is driven down till it no longer exceeds the function tolerance. This chapter utilizes a new cost function involving multiple controller specifications shown in Table 4.1.

4.6.1.1 Cost Function

Controller gain selection is achieved using the GA with a cost function that penalizes controller gains that exceed stability margin constraints and other constraints as chosen by the user. Hard constraints include stability margin constraints such as GM/PM, and time domain constraints such as overshoot (O%). Other constraints can include DRB/DRP, rise time, settling time, and tracking error for controller performance, as well as turbulence RMS error for controller robustness. For this chapter, the cost penalty for GM/PM increases when 5.5 dB and 45 degrees are exceeded, otherwise the cost is simply constant. If the GM/PM exceed 5 dB and 40 degrees, the penalty becomes very large penalizing the cost function. This is shown in the piecewise functions below.

$$GM_{penalty} = \begin{cases} (\frac{GM_{min}}{GM})^2 & GM < 5.5\ dB, \\ 1 & GM \geq 5.5\ dB, \\ 100 & GM < 5.0\ dB, \end{cases} \tag{4.13}$$

$$PM_{penalty} = \begin{cases} (\frac{PM_{min}}{PM})^2 & PM < 45\ deg, \\ 1 & PM \geq 45\ deg, \\ 100 & PM < 40\ deg. \end{cases} \tag{4.14}$$

For the best controller performance of the KHawk 55 UAS, the GM/PM values should be approximately 5.5 dB and 45 degrees. However, they can be lower (such as 5 dB and 40 degrees) but the stable flight range might be limited. The users can adjust the penalty weights based on knowledge of the system dynamics. An example case for the overshoot is given as the following.

$$O\%_{penalty} = \begin{cases} \frac{O\%}{O\%_{max}} & O\% > 10\ \%, \\ 1 & O\% \leq 10\ \%. \end{cases} \tag{4.15}$$

Another example of a cost function in consideration of roll tracking RMS error in turbulence is given below in equation (4.16). The RMS error is quadrupled to drive the gains to a smaller RMS error and 1 is added to the RMS error so that it is equal to 1 when no turbulence is present (all values are normalized around 1). This cost function with multiple constraints is shown in Fig. 4.2 with their corresponding penalty weights.

$$Cost = GM_{penalty} + PM_{penalty} + O\%_{penalty} + (1 + RMS)^4. \tag{4.16}$$

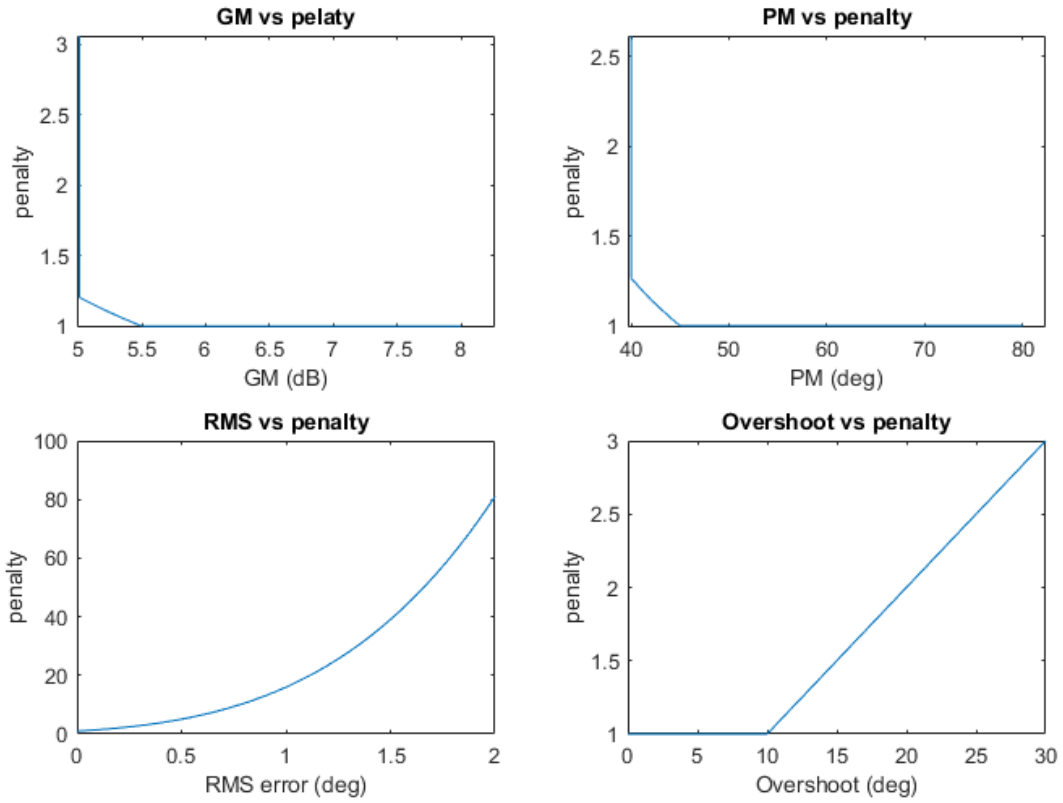

Figure 4.2: Cost function constraints and penalties.

4.6.2 Fractional Order Controller Analysis

The GAs for the high order FOPID and classical PID controller were run using cost functions specifically designed for different mission requirements and the constraint specifications shown in

Table 4.1.

4.6.2.1 Case 1: Improved Roll Tracking Performance

Case 1 is solely to analyze which controller is better for turbulence rejection while maintaining good stability requirements. Overshoot is allowed to exceed 10% with an added penalty as shown in equation (4.15). For case 1, both the FOPID and PID controllers have zero I gains since this slows the turbulence rejection response of the controller. The controller gains for both the FOPID and PID controllers are shown in Table 4.2 and are derived using the GA and the cost function shown in equation (4.16).

Table 4.2: Case 1 gain sets for PID and FOPID

Controller	K_p	K_d	K_i	μ	λ
FOPID	0.611	0.046	0	0.256	0
PID	0.461	0.063	0	0	0

The approximated fractional derivative Laplace equation is shown in equation (4.17), and is implemented through the modified Oustaloup approximation [49; 36]. The frequency range chosen for the controller is selected based on the KHawk UAS dynamics. The N integer representing the controller order is also manually chosen, but could alternatively be chosen using the genetic algorithm.

$$G_{approx} = s^{\mu} = \frac{31.82s^5 + 4118s^4 + 65040s^3 + 42450s^2 + 1000s}{6.696s^5 + 1284s^4 + 42870s^3 + 64780s^2 + 3685s + 8.147}. \tag{4.17}$$

The Bode plot of the FOPID and PID controllers are shown in Fig. 4.3. The specifications for each controller are shown in Table 4.3 including the crossover frequency (ω_c). The step response of the two controllers are shown in Fig. 4.4. The Bode plots showing the two controllers' GM/PM and DRB/DRP are depicted in Figs. 4.5 and 4.6.

The FOPID controller shows greater stability in terms of PM than the PID controller, as well as higher DRB and lower DRP. The decrease in DRP is important since it refers to a decrease in

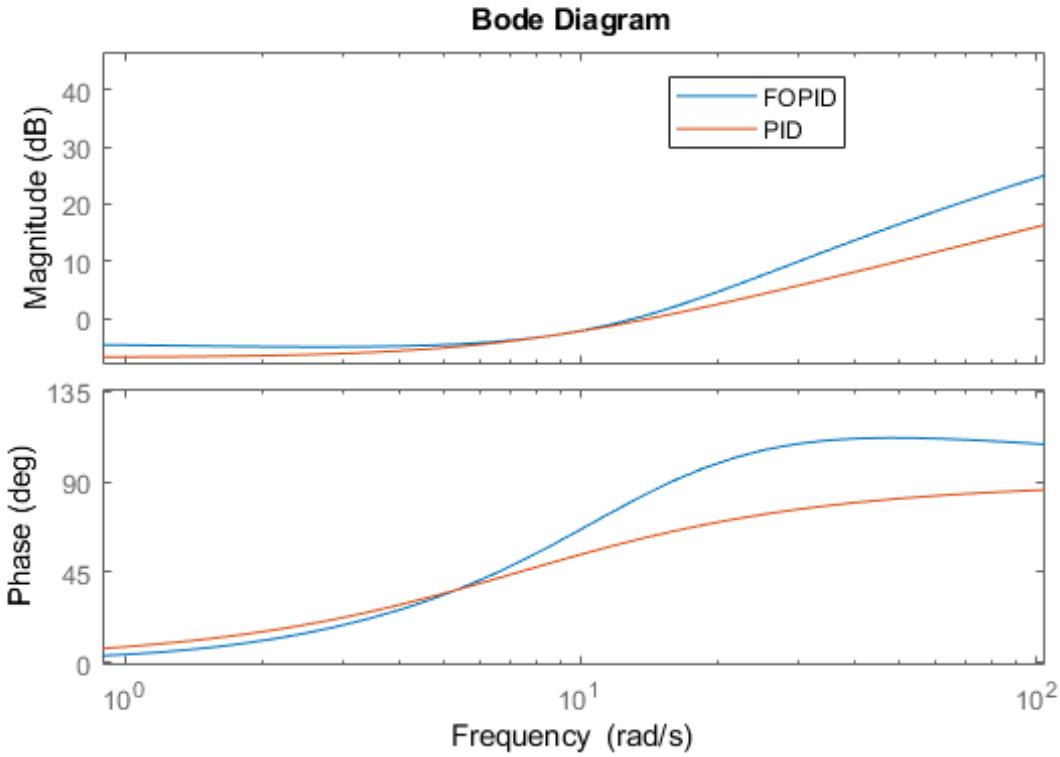

Figure 4.3: Bode diagram of the controllers.

Table 4.3: Case 1 controller specifications

Frac**Gain**	**GM (dB)**	**PM (deg)**	ω_c **(rad/s)**	**O%**	**DRB (rad/s)**	**DRP (dB)**
FOPID	5.00	55.64	8.87	12.47	2.26	4.72
PID	5.00	45.40	8.87	8.31	2.10	5.33

sensitivity from disturbances influencing the aircraft's roll angle. A lower DRP will result in less roll tracking error during encounters of turbulence in specific frequency ranges. This is evident in Fig. 4.6 at around the 10.5-14 rad/s frequency range. The step response, broken loop response, and disturbance rejection response are shown in Fig. 4.4-4.6.

The high order SISO lateral dynamic model was used with an added Dryden turbulence model to represent the impact of turbulence on the two controllers [7]. The tracking response of the controllers over a 20 second period is shown in Fig. 4.7 and the results for the roll RMS error during turbulence encounters are shown in Table 4.4. The FOPID shows advantages over the PID

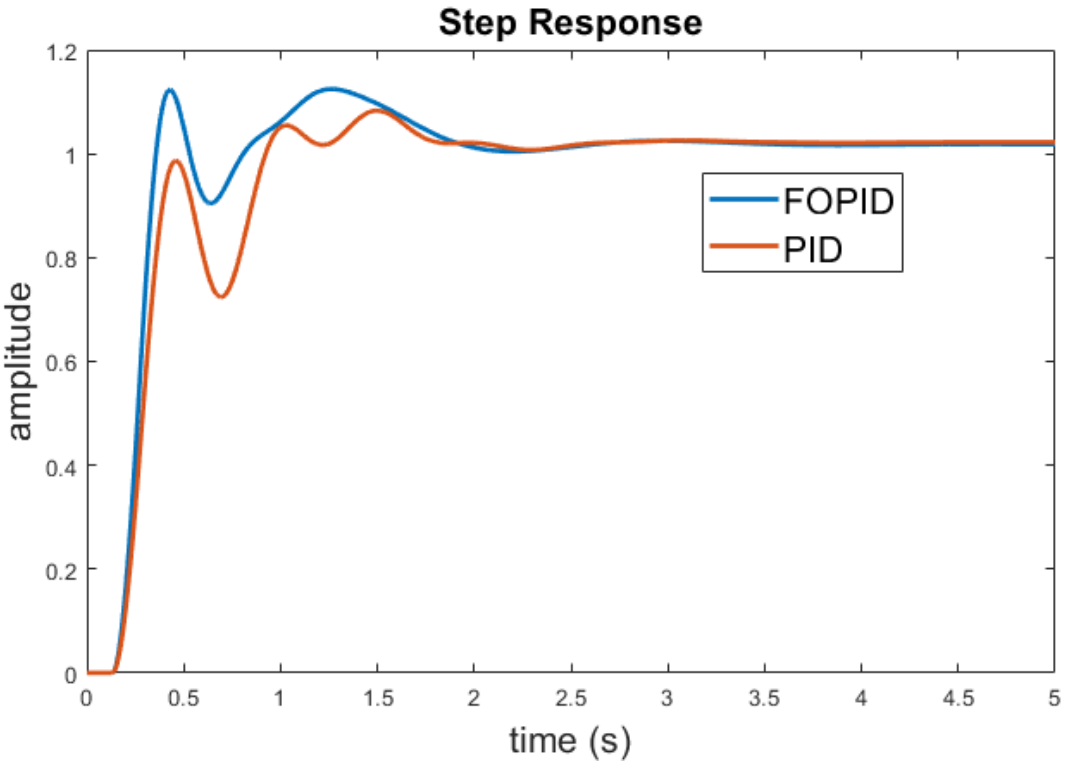

Figure 4.4: Step response.

controller in terms of both RMS error and max error. Note that the FOPID rejects turbulence better around the 10.5-14 rad/s frequency range with less max error. This is due to the lower DRP value of the FOPID controller resulting in greater turbulence rejection in that specific frequency range.

Table 4.4: RMS error for turbulence rejection

Gain	RMS (deg)	Max Error (deg)
FOPID	0.55	1.54
PID	0.64	1.99

4.6.2.2 Case 2: Improved Time Domain Performance using Overshoot and Settling Time

Case 2 puts emphasis on minimizing overshoot while keeping a 2% settling time below 5 seconds. This is to provide a good controller tracking performance while keeping steady state error at the minimum. The controller gains and specifications are shown in Table 4.5 and Table 4.6.

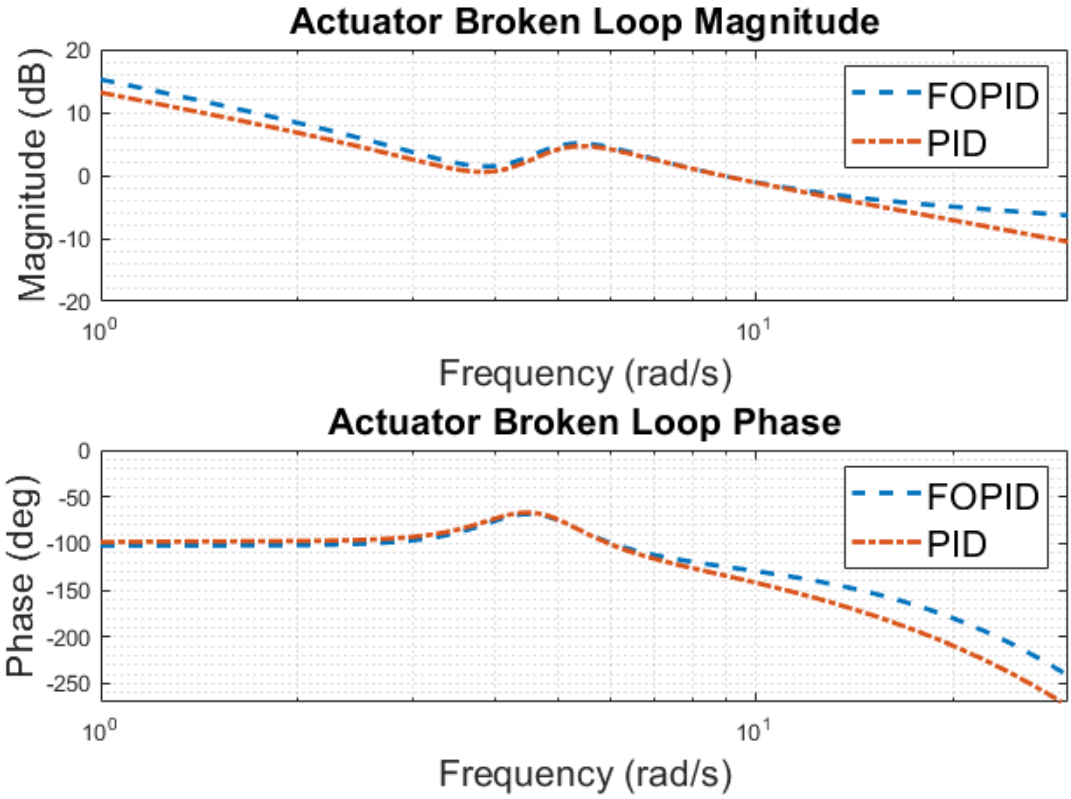

Figure 4.5: Gain and phase margins of the two controllers.

Table 4.5: Case 2 gain sets for PID and FOPID

Gain	K_p	K_d	K_i	μ	λ
FOPID	0.6018	0.0431	0	0.2636	0
PID	0.4537	0.0580	0.1985	0	0

Table 4.6: Case 2 controller specifications

Gain	**GM(dB)**	**PM(deg)**	ω_c**(rad/s)**	**O%**	**DRB(rad/s)**	**DRP(dB)**	**2%ts(s)**
FOPID	5.40	55.76	8.51	12.64	2.28	4.78	3.43
PID	5.51	46.88	8.28	19.27	1.84	5.37	5

The FOPID controller has significantly less overshoot than the PID controller and a much better 2% settling time of 3.43 seconds. The FOPID controller also does not need an integral gain since the fractional order derivative controller can be tuned to accomplish the mission tasks. This results

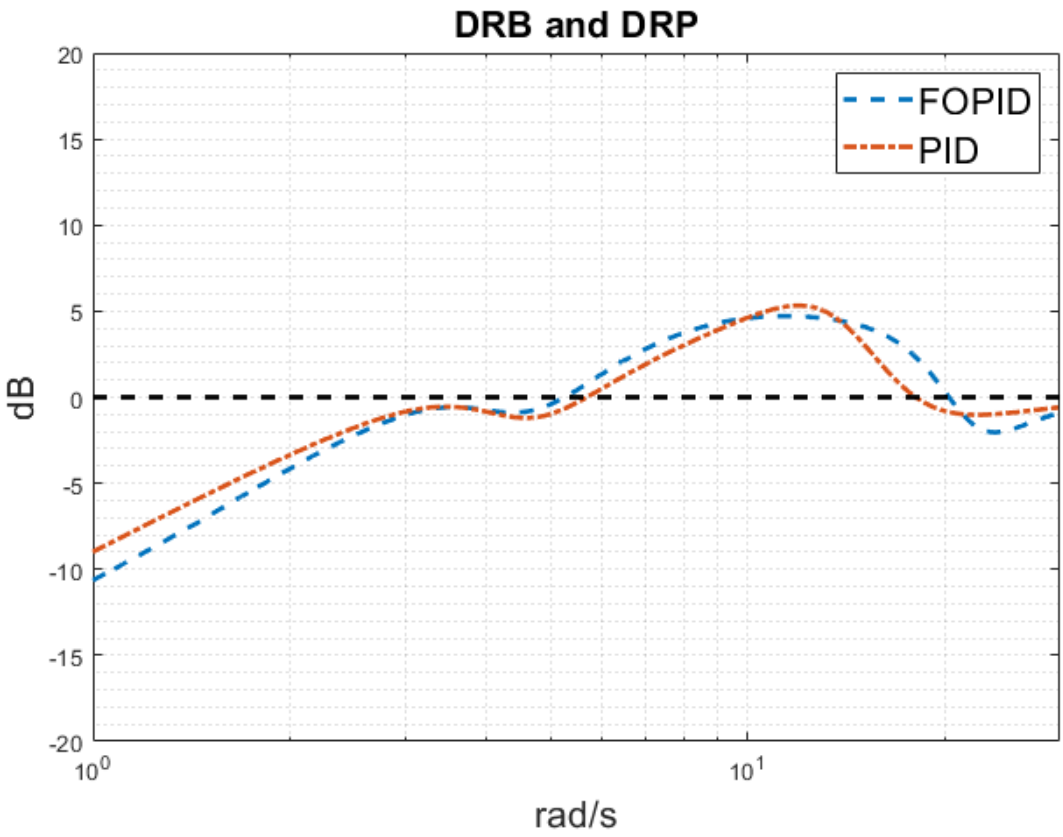

Figure 4.6: Disturbance rejection bandwidth and peak for the two controllers.

in less overshoot and a faster controller response. The broken loop and disturbance rejection loop plots are shown in Fig. 4.9 and Fig. 4.10.

The FOPID was able to accomplish case 2 requirements by simply changing the fractional derivative gain and not by adding a large I gain. This provides faster controller performance and subsequently better turbulence response. Fig. 4.8 and Fig. 4.10 show an increase in rise time and increase in DRB, which represents faster controller response.

4.6.2.3 Case 3: Cumulative Approach with Actuator RMS Minimization

Case 3 is a cumulative approach combing cases 1 and 2 with the addition of actuator RMS to minimize controller movements. The actuator RMS describes the distance that the servo fluctuates from the trim position. The optimized controller gains and acquired specifications are shown in Table 4.7 and Table 4.8. The step response is shown in Fig. 4.11. The FOPID controller again

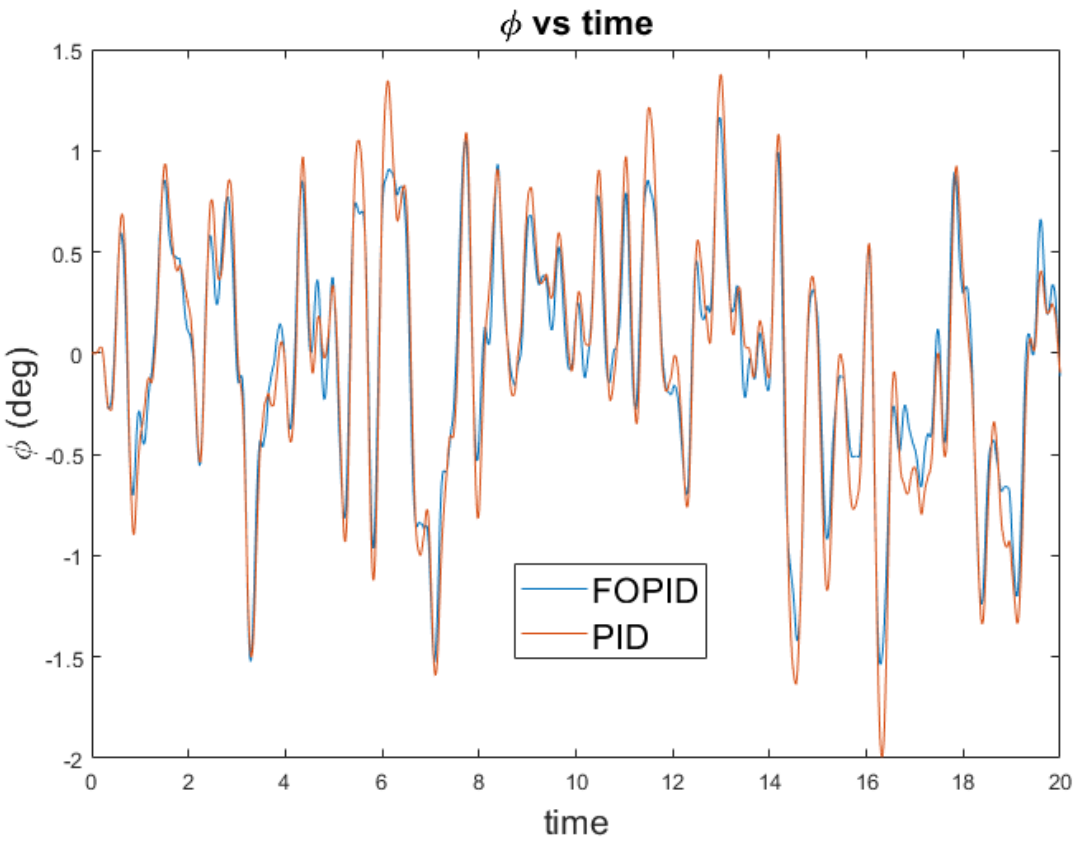

Figure 4.7: Turbulence rejection response for the two controllers.

has significantly less overshoot than the PID controller and a much better 2% settling time of 3.56 seconds. The broken loop and disturbance rejection loop plots are shown in Fig. 4.12 and Fig. 4.13. The FOPID has a higher DRB which aids in a faster return to trim. It is worth mentioning that the FOPID does sacrifice DRP which can result in larger overshoots from turbulence in the DRP frequency range (approximately 6 to 12 rad/s). These overshoots can be seen in the turbulence rejection plot shown in Fig. 4.14.

Table 4.7: Case 3 gain sets for PID and FOPID

Gain	K_p	K_d	K_i	μ	λ
FOPID	0.5671	0.0468	0.0004	0.1886	1.0519
PID	0.4537	0.0580	0.1985	0	0

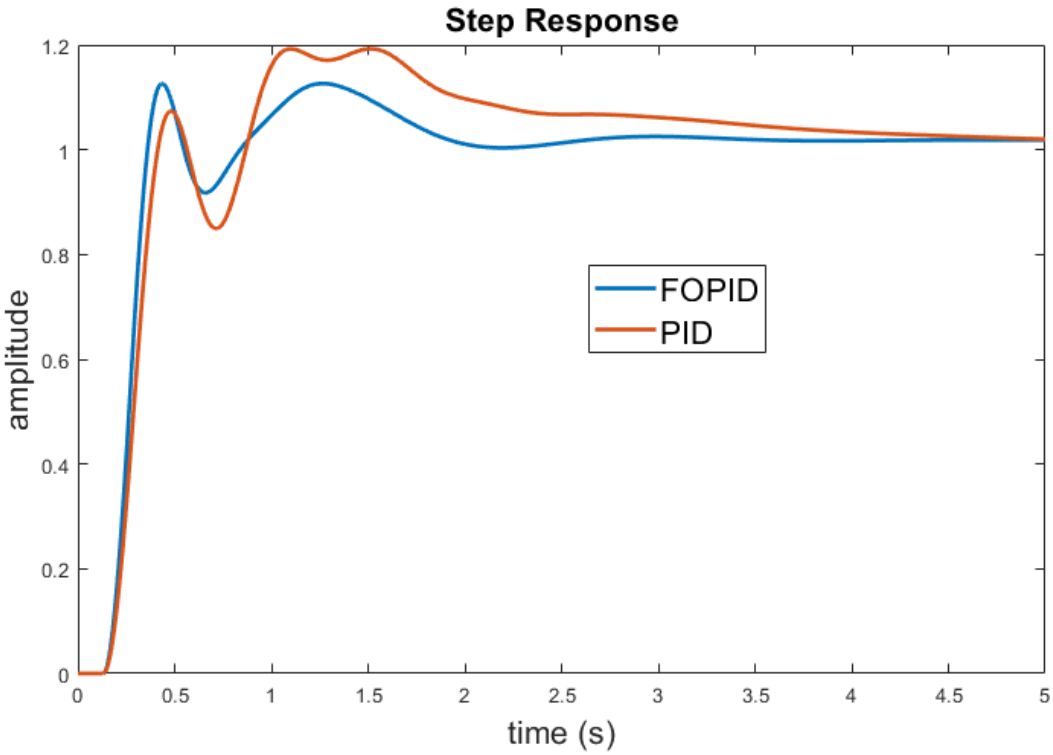

Figure 4.8: Step response for case 2.

Table 4.8: Case 3 controller specifications

Gain	GM(dB)	PM(deg)	ω_c(rad/s)	O%	DRB(rad/s)	DRP(dB)	2%ts(s)
FOPID	5.64	52.25	8.63	11.22	2.23	4.99	3.56
PID	5.23	54.68	8.39	22.52	1.49	4.19	5

4.7 Conclusion

In this chapter, a FOPID controller design method is proposed based on the open loop lateral dynamics of a small UAS. The proposed FOPID controller considers specifications from both time domain and frequency domain including overshoot, GM, PM, DRB, DRP, etc. The controller is validated in simulation using the identified aileron roll-rate model of the KHawk 55 UAS. The FOPID controller showed better performance in all cases, and showed more tuning flexibility with the additional control tuning variables μ and λ. This increase in tuning flexibility for a fractional controller should be helpful in creating more robust controllers for UAS that would otherwise use

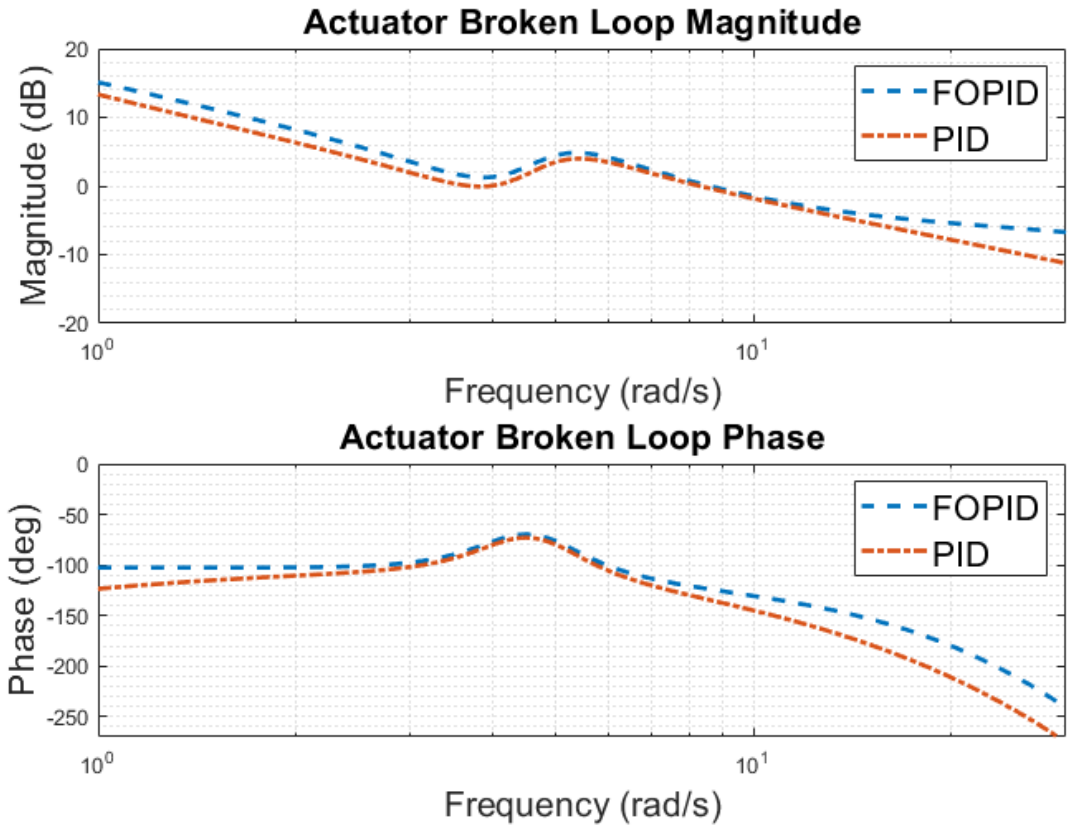

Figure 4.9: Gain and phase margins of the two controllers for case 2.

a simple integer order PID. Future works include fractional order turbulence modeling, fractional order aircraft dynamics modeling, and flight test validation.

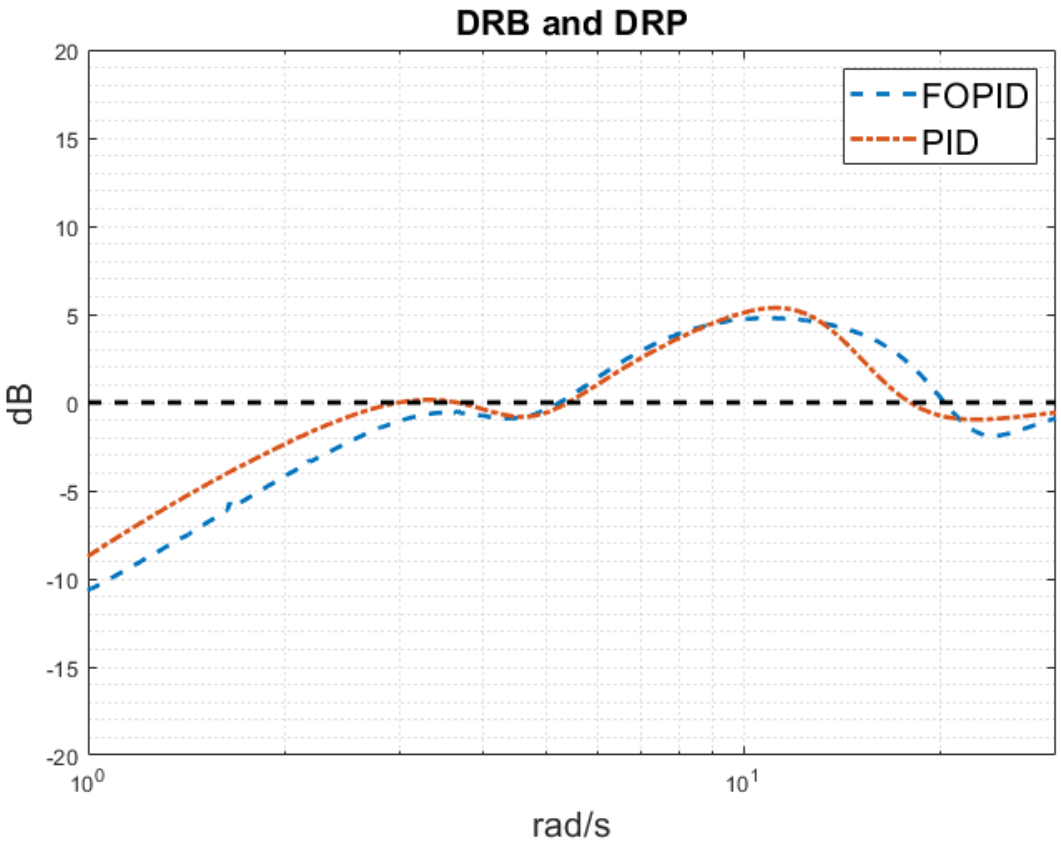

Figure 4.10: Disturbance rejection bandwidth and peak for the two controllers for case 2.

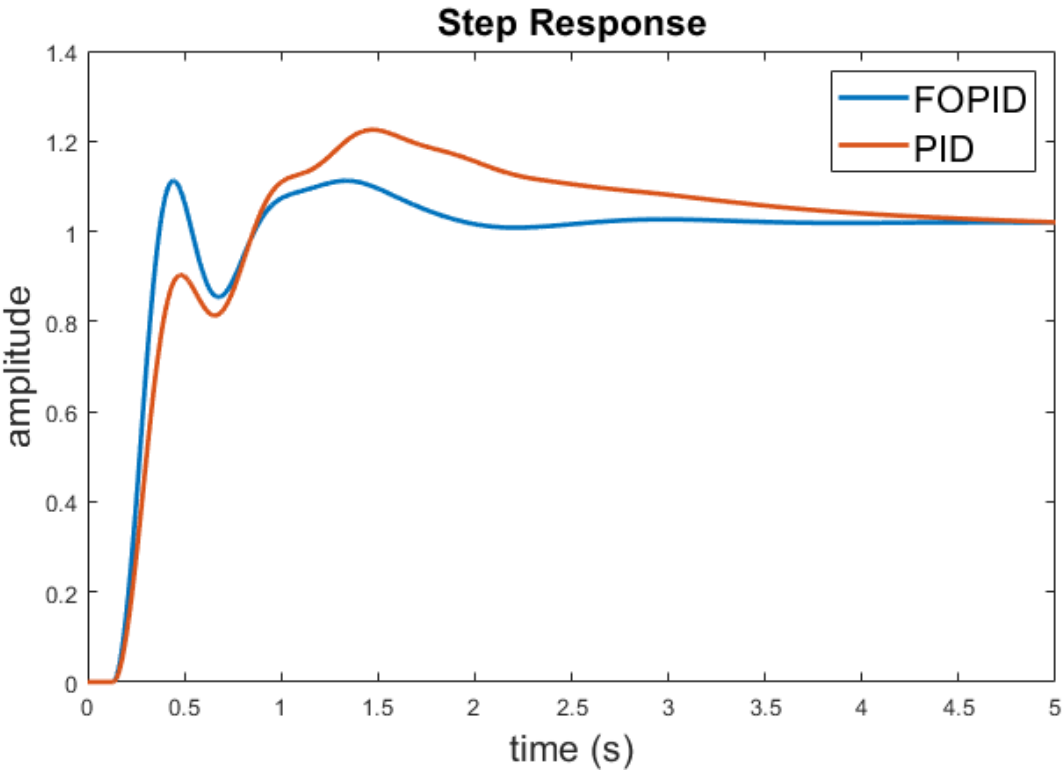

Figure 4.11: Step response for case 3.

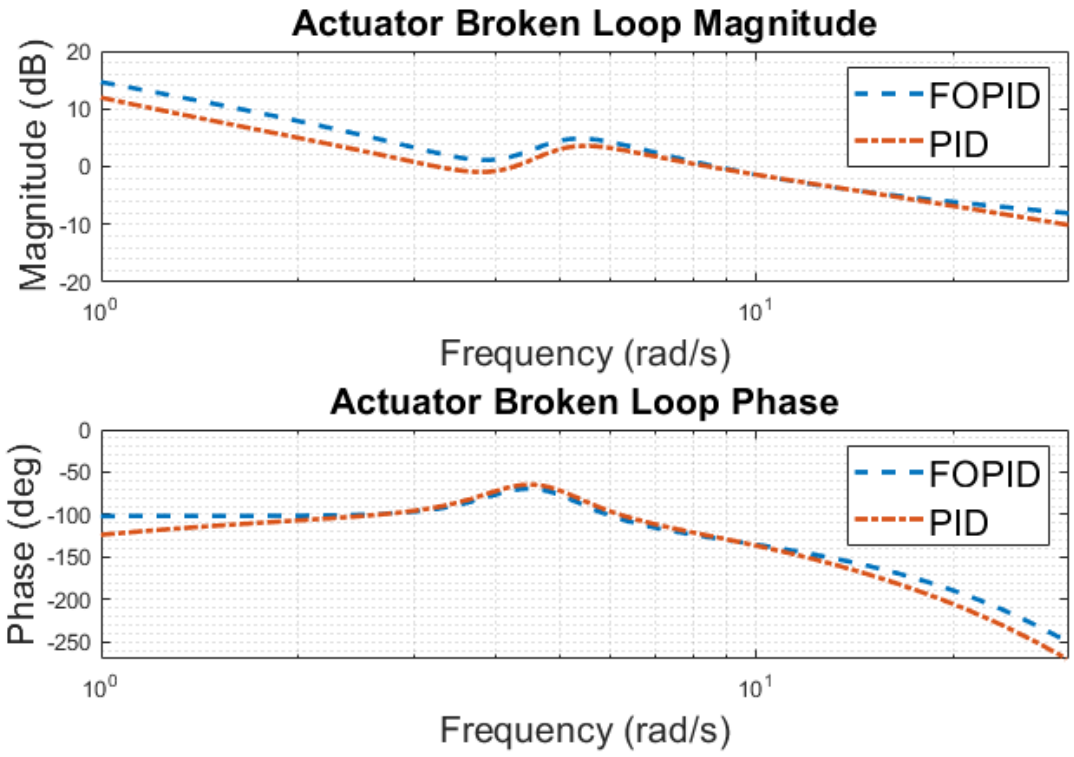

Figure 4.12: Gain and phase margins of the two controllers for case 3.

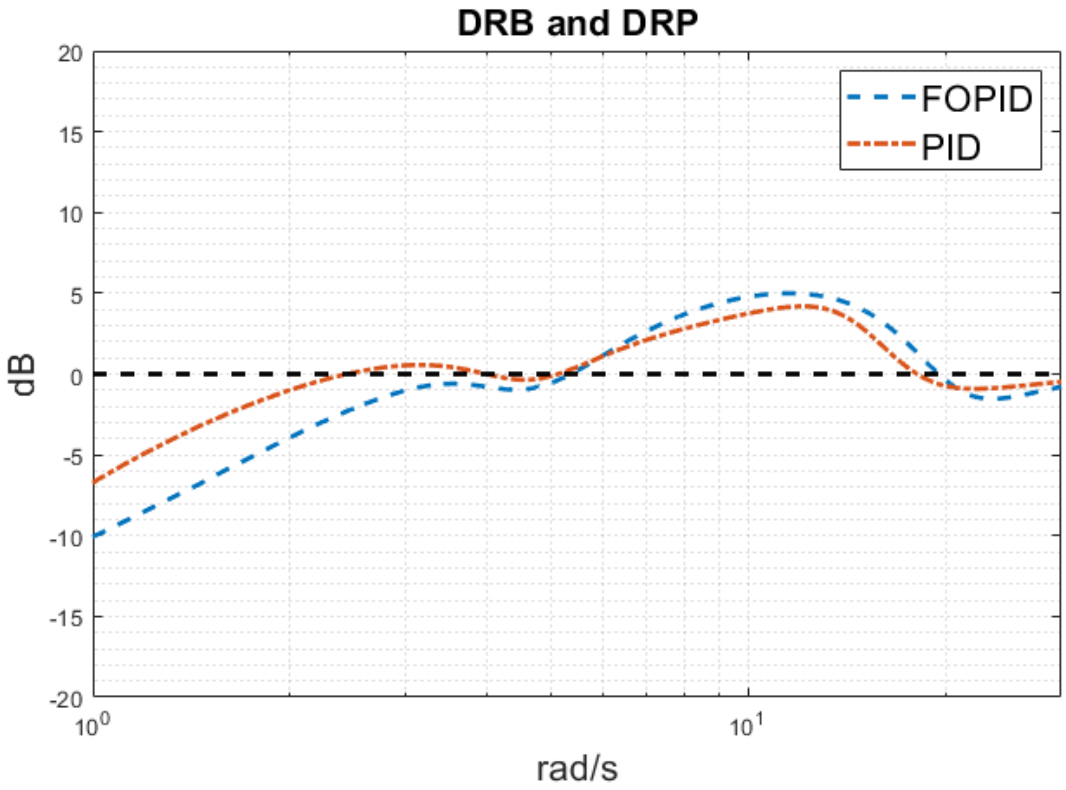

Figure 4.13: Disturbance rejection bandwidth and peak for the two controllers for case 3.

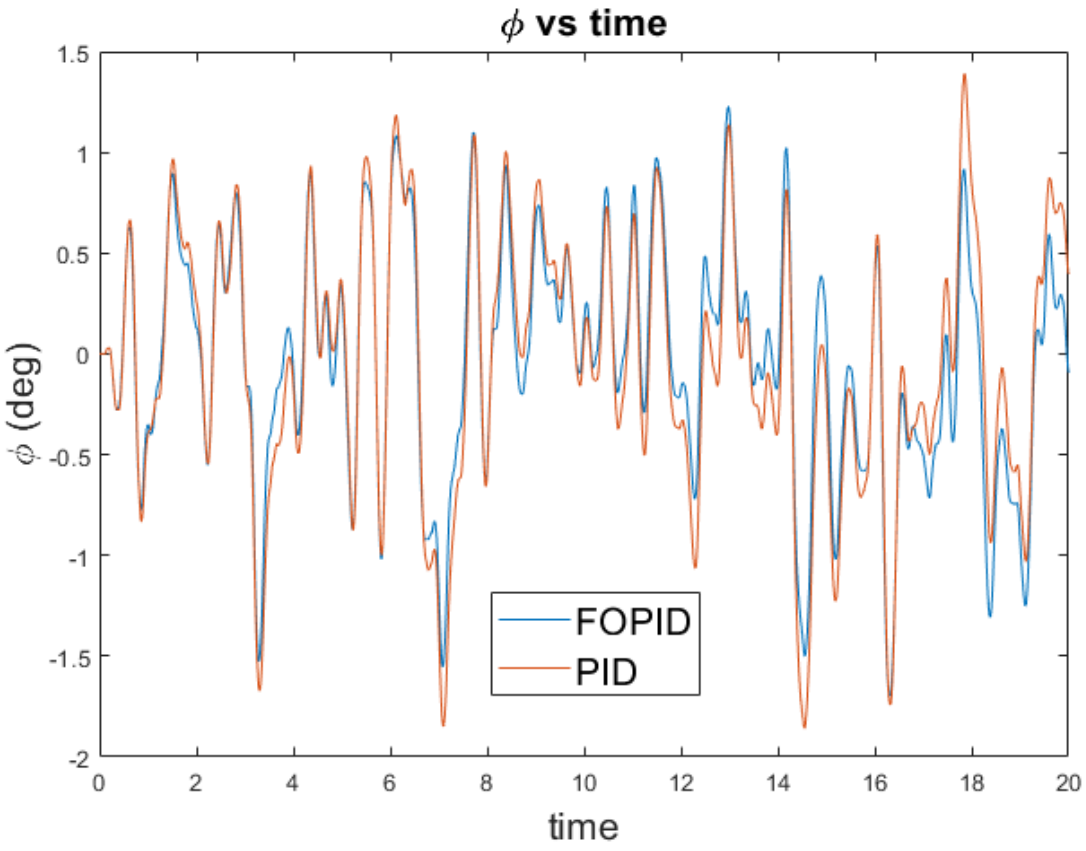

Figure 4.14: Turbulence rejection response for the two controllers for case 3.

Chapter 5

Complementary Filter based Flow Angle Estimation and Stall/Spin Detection

Abstract

Stall/spin is one of the biggest factors for aircraft crashes based on statistical accidents reports. Stalls will be more frequently encountered by unmanned aircraft systems since most of them fly at air speeds comparable to prevailing wind and gusts in the atmospheric boundary layer. However, it is very difficult to get an accurate prediction on when stall/spin will occur for unmanned aircraft because lift estimates or angle of attack measurements may not be available. This chapter provides a thorough flight test investigation of stall/spin detection techniques for a flying-wing UAS. Different types of stall data were collected through flight tests using a low-cost UAS platform, including flat stall, spin stall, vertical stall, etc. Several representative stall detection algorithms are used on the collected data including critical angle of attack estimation method, roll and yaw divergence methods. A new stall detection algorithm is proposed based on inertial angle of attack estimated without using flow angle sensors. Further analysis of collected stall data showed the effectiveness of the proposed methods for stall/spin detection and warning.

5.1 Introduction

Stall/spin is one of the most common factors that cause aircraft crashes. It is reported that stall/spin accounted for about 10 percent of all accidents, but 13.7 percent of accidents with casualties based

on a report by Aircraft Owner and Pilot Association (AOPA) using accident data from 1993 to 2001 involving fixed-wing aircraft weighing less than 12,500 pounds [50]. The accident percentage is even higher for the commercial jet fleet. Stall/departures including falling leaf and spin happened 38.9 percent among all the accidents based on fatal accident data of commercial jets from 1999 to 2008, collected by CAST/ICAO Taxonomy Team (CICTT) [51]. Stall/spin is also treated as the leading factor that causes Remote Controlled (RC) airplanes to crash since hobbyists can easily run into problems such as unstable Center of Gravity (CG), strong winds or gusts, too much elevator input, or aggressive flight maneuvers. Although no statistics have been published on detailed causes of accidents for Unmanned Aircraft Systems (UASs), stall/spin is probably the leading cause for crashes given the fact that many small UASs are similar to RC hobby level aircraft. The increasing UAS numbers in recent years makes the stall/spin detection and mitigation problem even more significant. In fact, it is predicted that 250,000 unmanned aircraft may use the U.S. national airspace every day by 2035.

There are several existing methods for stall/spin detection. The most widely used strategy for manned aircraft is to use an angle of attack (AOA) sensor, or AOA indicator for stall warning. However, most small UASs (< 55 lbs) do not have AOA sensor installed because limitations from space and weight. In addition, there exists no commercial off the shelf (COTS) UAS autopilot that includes AOA measurements in the flight control loop for stall detection and mitigation [6]. A multi-hole pitot tube can be used for measurements of angle of attack and angle of sideslip. Nevertheless, they are expensive and require accurate calibration. Other than the above flow measurement sensors, inertial and air speed sensors can be combined or integrated to estimate when a stall might occur [52; 53; 54]. However, further work is needed in this field for reliable prediction at or right after the stall so that certain mitigation techniques can be applied to recover the UAS quickly.

The main objectives of this chapter is to look into the characteristics of different types of stalls for UAS, to collect multiple sets of typical stall data using a flying-wing UAS platform, and to validate representative stall detection strategies. The major contributions of this chapter include a

detailed analysis of typical stall data for a flying-wing UAS, a thorough analysis of stall detection techniques for small UASs, and the introduction of a new stall detection technique based on inertial angle of attack estimated from inertial and air speed sensors.

The organization of this chapter can be summarized as follows. The problem of stall/spin detection and mitigation is formulated in Section 5.2. Different UAS stall types are explained in Section 5.3. Stall detection strategies are further presented in Section 5.4. Section 5.5 focuses on flight test results. Finally, conclusions are made in Section 5.6.

5.2 Stall/Spin Problem Formulation

A stall is a condition where the angle of attack increases beyond a critical value such that the flow separates from the wing and results in a drastic loss of lift. The angle at which this occurs is called the critical angle of attack [55]. The critical AOA for general aviation single-engine aircraft is usually around 16-18 degrees, while the critical AOA for UASs varies for different platforms. Fixed-wing aircraft stalls are usually followed by buffet, attitude changes, or spins. It is worth mentioning here that stall can happen even when the aircraft is flying faster than the published stall speed. In fact, stall can happen at any air speed and any attitude. For example, an RC aircraft can enter a stall easily if it is maneuvering with high load factors or is commanded to bank aggressively. Nevertheless, the max design lift and max takeoff weight for many RC aircraft is usually unknown. RC hobbyist and UAS researchers may have to figure this out by trial and error.

A summary of potential reasons that cause small UAS to stall includes:

1. bad trim: excessive up trim can potentially get a UAS into stall during flight,
2. aggressive flight maneuvers: aggressive turning with large a bank angle can cause a UAS to enter a stall,
3. strong wind or gusts: a UAS can enter stall while turning in strong prevailing wind or gusts,
4. center of gravity (CG) shifting: a rear heavy UAS is more vulnerable to stall than a well-balanced

one,

5. structure failures: structure failures that significantly affect the wing lift could make the aircraft stall as well.

Stall is usually detected by AOA indicators for manned aircraft. However, it is not feasible to install heavy AOA indicators or expensive multi-hole pitot tubes on most small UASs. On the other side, small UASs are usually equipped with GPS receiver for 3D position and ground velocity measurements, inertial measurement unit (IMU) for attitude, angular rate, and acceleration measurements, and pitot-tube for static and dynamic pressure measurements. Given inertial, GPS, static and dynamic pressure measurements, it is possible to design an estimation filter to locate the time when stall/spin happens and perform associated strategies for stall alleviation.

5.3 Types of UAS Stall/Spin Scenarios

Stalls for UASs can be divided into different categories based on specifications. Stalls can be categorized as power-on stalls or reduced power stalls based on throttle setting. Reduced power stalls, or power-off stalls may be caused by engine failures or speed controller failures for UAS.

Stalls can also be grouped into the following types based on when the stall occurs, including:

1. departure stalls, which can be treated as power-on stalls, and could be caused by strong wind or gusts during take-off,

2. arrival stalls, which can be treated as power-off stalls or reduced power stalls, and could be triggered with improper airspeed while approaching to land,

3. Accelerated stalls, which can happen with abrupt control maneuvers, steep turns, or strong gusts,

For UAS flight testing purposes, the following stall maneuvers are focused based on how stalls are generated. The detailed procedure for stall generation is also included for reference.

1. Turn Stall (Fig. 5.1)

- The plane is flown at a slow airspeed similar to the speed before turning final to land.
- The plane is commanded to turn at a high roll angle (e.g. > 45 deg.) while up elevator is given.
- Up elevator is applied until the plane stalls.

2. High AOA Stall (Fig. 5.2)

- Plane is flown straight and level. The stall can be performed as either a power-on or power-off stall,
- The plane is given elevator up command continuously until it enters stall,
- This stall can happen when the UAS's engine or speed controller fails. It can also happen during landing,

3. Vertical Stall (Fig. 5.3)

- The plane is flown at cruise speed or a faster speed during level flight.
- The plane is given up elevator until the plane is perpendicular to the ground.
- The throttle is shut off and the plane is allowed to stall.

In addition to different stall maneuvers, various stall types are analyzed based on aircraft responses after the stall. Associated stall recovery strategies are also included here.

1. Spin Stall (Fig. 5.4)

- Aircraft begins to roll once it is stalled. The aircraft will continue to roll until laminar airflow is achieved over the wing.
- This stall can be performed as either a power-on or power-off stall.

- Aircraft can be recovered by nosing the plane down and allowing the plane to gain speed.

2. Flat Stall (Fig. 5.2)

   - For this mode, aircraft stalls without going into a spin and stalls flat with the wings level. This stall only happens to unmanned aircraft that is well tuned and aerodynamically clean.
   - Aircraft can be recovered by nosing the aircraft down and allowing the aircraft to gain speed.

3. Flat Spin

   - Aircraft stalls flat but begins to spin around its yaw axis. This can be caused by poor CG placement.
   - Once the aircraft has entered the flat spin, it may be difficult to recover.

4. Deep Stall

   - Similar to the flat spin stall but without the spinning moment.
   - Recovery may be difficult. The pilot can try to recover the aircraft by accelerating it out of the stall (assuming high power to mass ratio).

In consideration of the characteristics of most small UASs, the following stall types were flight tested using a KHawk 55 UAS platform, including turn stall, high AOA stall, vertical stall, spin stall, and flat stall. Detailed flight results are shown and discussed in later sections.

5.4 Stall/Spin Detection Strategy

Different approaches of stall detection strategies are compared in this section for a flying-wing aircraft with elevons, which can be treated as a combination of ailerons and elevators. It is worth mentioning that the movement of elevons on a flying-wing aircraft can affect the lift significantly,

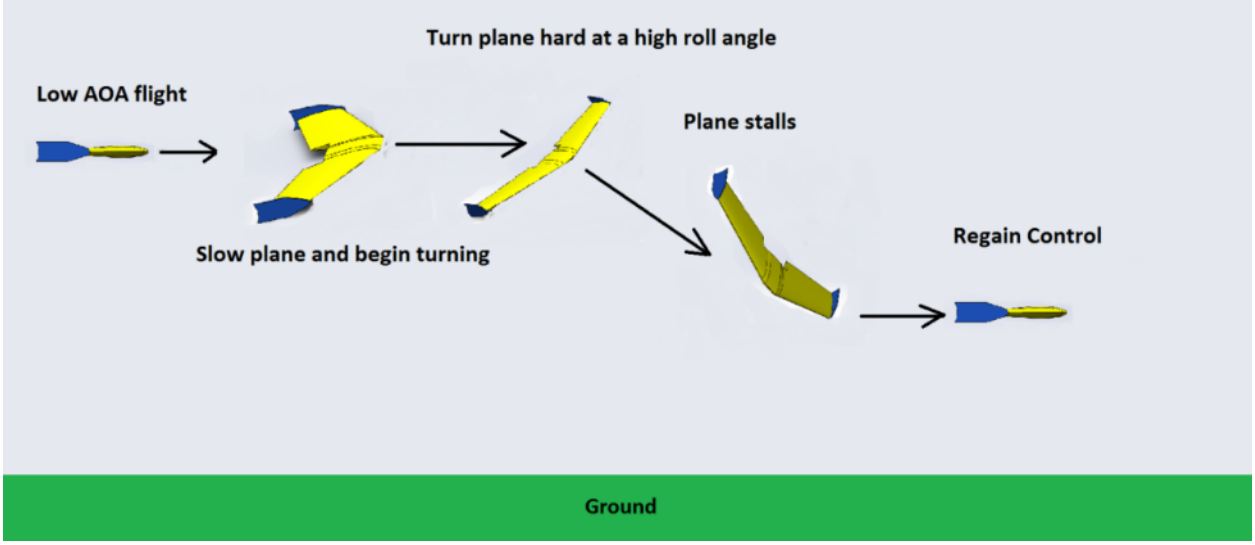

Figure 5.1: Turn stall.

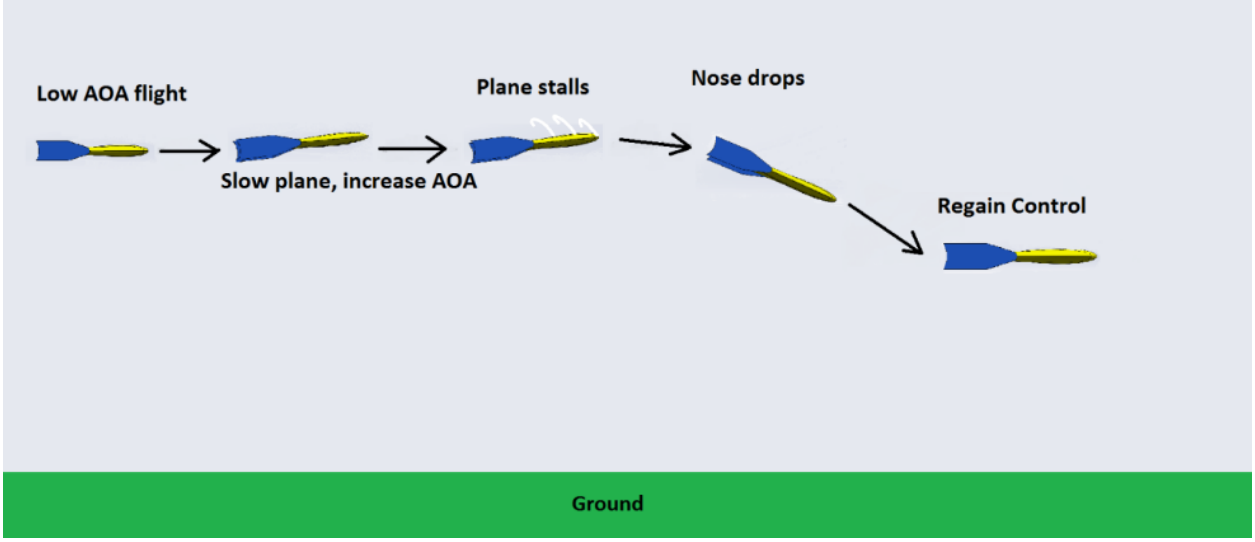

Figure 5.2: Flat stall.

while the movement of rear-installed elevators will not affect the wing lift that much for a conventional tailed aircraft. Three different stall detection methods are focused in this section based on critical AOA estimation, roll divergence, and yaw divergence.

5.4.1 Critical AOA Method

Although AOA can be measured by a flow angle sensor, most small UASs do not have onboard 5-hole pitot tube or vane sensors due to limitations from size, weight, and budget. Inertial AOA

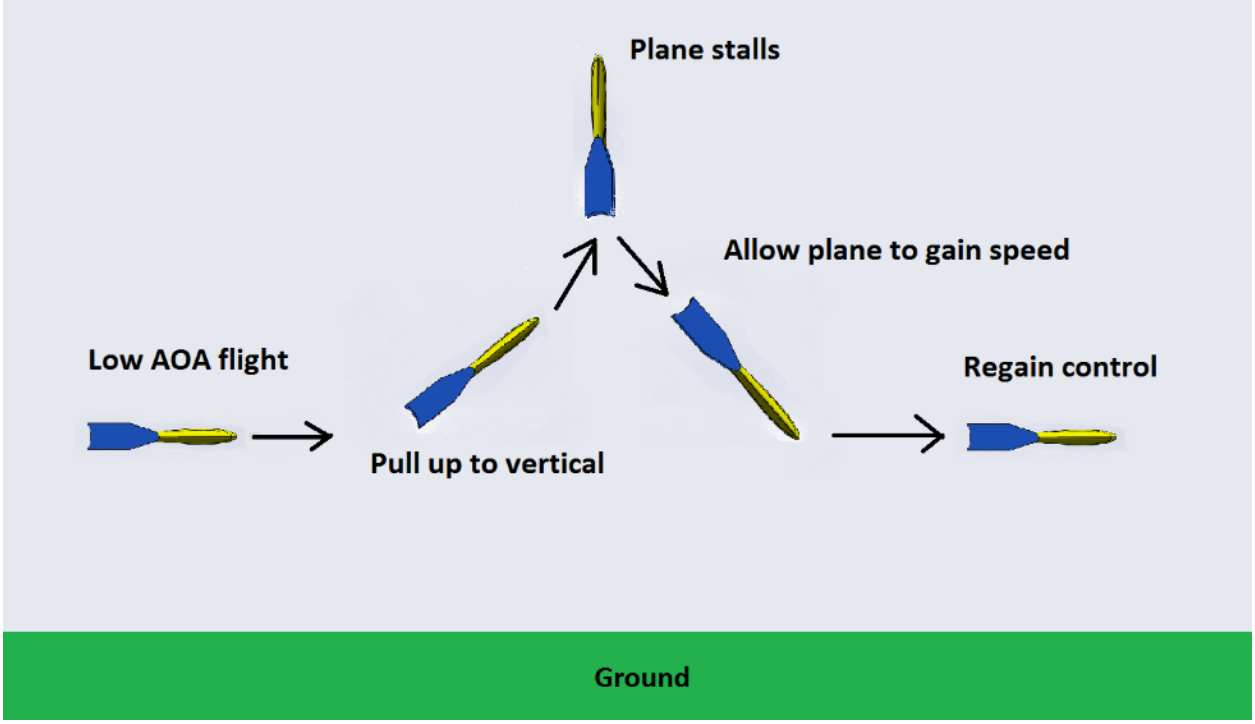

Figure 5.3: Vertical stall.

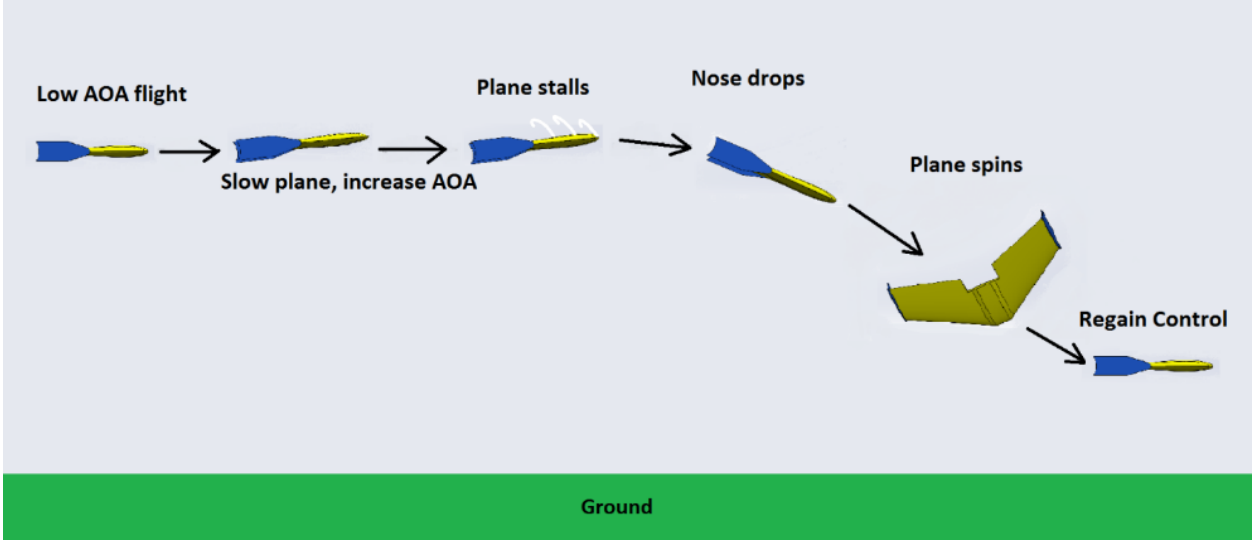

Figure 5.4: Spin stall.

can be used instead for stall detection purposes [56]. A second-order complementary filter is proposed in this chapter for the estimation of the inertial AOA, without using flow angle sensor measurements. The equations are listed as follows, including long term AOA estimate (low pass component) and short term AOA estimate (high pass component):

$$\alpha_{inertial} = \frac{s}{s^2 + 2\zeta\omega_n s + \omega_n^2}\dot{\alpha} + \frac{2\zeta\omega_n s + \omega_n^2}{s^2 + 2\zeta\omega_n s + \omega_n^2}\alpha_{long} \tag{5.1}$$

$$\alpha_{long} = \frac{\frac{-ma_{z_s}}{\bar{q}S} - C_{L_0} - C_{L_{\delta_e}}\delta_e - C_{L_q}q}{C_{L_\alpha}} \tag{5.2}$$

$$\dot{\alpha} = q + g\frac{cos\phi cos\theta\ cos\alpha + sin\theta sin\alpha - a_{z_s}/g}{V_a} \tag{5.3}$$

The diagram for the complementary filter is given in Fig. 5.5. The long term AOA estimate is based from the estimation of lift after removing effects generated by elevator command and pitch rate. In this chapter, the sideslip angle is assumed to be negligible for Eq. 5.2. The short term AOA estimate is based on the integration of pitch rate after compensating for acceleration and rotations, which also assumes small perturbations around steady wings-level flight. The short-term and long-term estimates are combined using a second-order complementary filter to get the final estimation of inertial AOA.

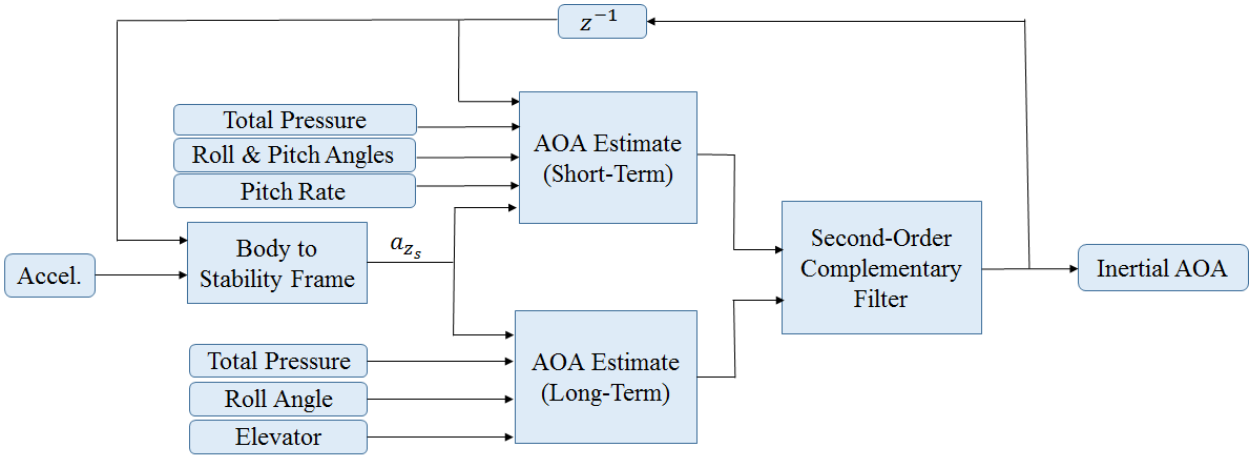

Figure 5.5: Diagram for inertial AOA complementary filter.

To estimate the long-term AOA, four major lift coefficients need to be identified for the lift equation. Because a flying wing aircraft uses elevons and rotates quickly about its y axis, both $C_{L_{\delta_e}}$ and C_{L_q} needed. The lift coefficient can be approximated with a combination of nominal acceleration and the total pressure, named as $\overline{C_L}$. This inertially calculated $\overline{C_L}$ equals C_L during

UAS routine flights, assuming that the sideslip angle is close to zero and the elevator input is below the natural frequency of the short period mode. The identification of the lift coefficients can be done by performing a least squares analysis on flight data involving elevator flight maneuvers when the aircraft is "chirped" up and down at selected frequencies below the natural frequency of the aircraft. The detailed equations are listed as the following:

$$C_L = C_{L_0} + C_{L_\alpha}\alpha + C_{L_q}q + C_{L_{\delta_e}}\delta_e \tag{5.4}$$

$$L \approx -ma_{z_s} = \bar{q}SC_L \tag{5.5}$$

$$\overline{C_L} = \frac{-ma_{z_s}}{\bar{q}S} \tag{5.6}$$

$$a_{z_s} = -a_x sin\alpha + a_z cos\alpha \tag{5.7}$$

5.4.2 Roll Divergence Method

The derivative of roll rate can be used as an indication of stall/spin since it is an indication of rolling moment [52; 53; 54]. The derivative of roll rate follows the linear trend around the normal operating trim points since all the coefficients are generally linear. The nonlinear part can be a good indication of a stall. The above approach works well for spin stalls. However, it may not work with flat stalls or any other stall that does not include a spin.

$$I_{xx}\dot{p} = L_p p + L_{\delta_a}\delta_a + L_\beta\beta + L_r r \tag{5.8}$$

5.4.3 Yaw Divergence Method

The derivative of yaw rate can be similarly used as another indicator of stall/spin [52; 53; 54]. This approach has the similar limitations with roll divergence.

$$I_{zz}\dot{r} = N_r r + N_{\delta_a}\delta_a + N_p p + N_\beta \beta \tag{5.9}$$

5.5 UAV Flight Validations

5.5.1 Flight Data Collection

Multiple sets of flight data were collected for identification of lift coefficients and for data collection of different stall maneuvers. The flight test procedure for stall/spin data collection using a KHawk 55 UAS is summarized as the following:

1. launch the KHawk 55 UAS with a bungee chord,
2. RC pilot quickly checks the trim of the UAS,
3. RC pilot flies the aircraft to around 100 meters altitude above ground level,
4. RC pilot starts to perform certain maneuvers for different types of stalls once the aircraft is stable,
5. ground observer takes all the videos during the whole flight test period for validation purpose.

Two representative stall data sets are shown in this chapter, stall data collected using an Eagle Tree pitot-tube (no measured AOA) and stall data collected using an Aeroprobe 5-hole pitot tube (measured AOA). Multiple types of stall data were generated for each flight.

5.5.1.1 Elevator Doublet Data

The flight data used for the lift coefficient identification are shown in Fig. 5.6. The elevators were actuated up and down manually at approximately 0.33 Hz, 0.5 Hz, and 1 Hz, which caused the

pitch angle of the aircraft to vary between -30 and 30 degrees. The elevator doublet maneuvers were performed at the aircraft's cruise speed and six out of the eight elevator doublet sets were used for the identification of lift coefficients. The control commands were saved on the ground control station at 20 Hz. All the data were manually synced based on take-off, landing, and other peak values. Fig. 5.7 shows one set of the elevator doublet data at 0.5 Hz.

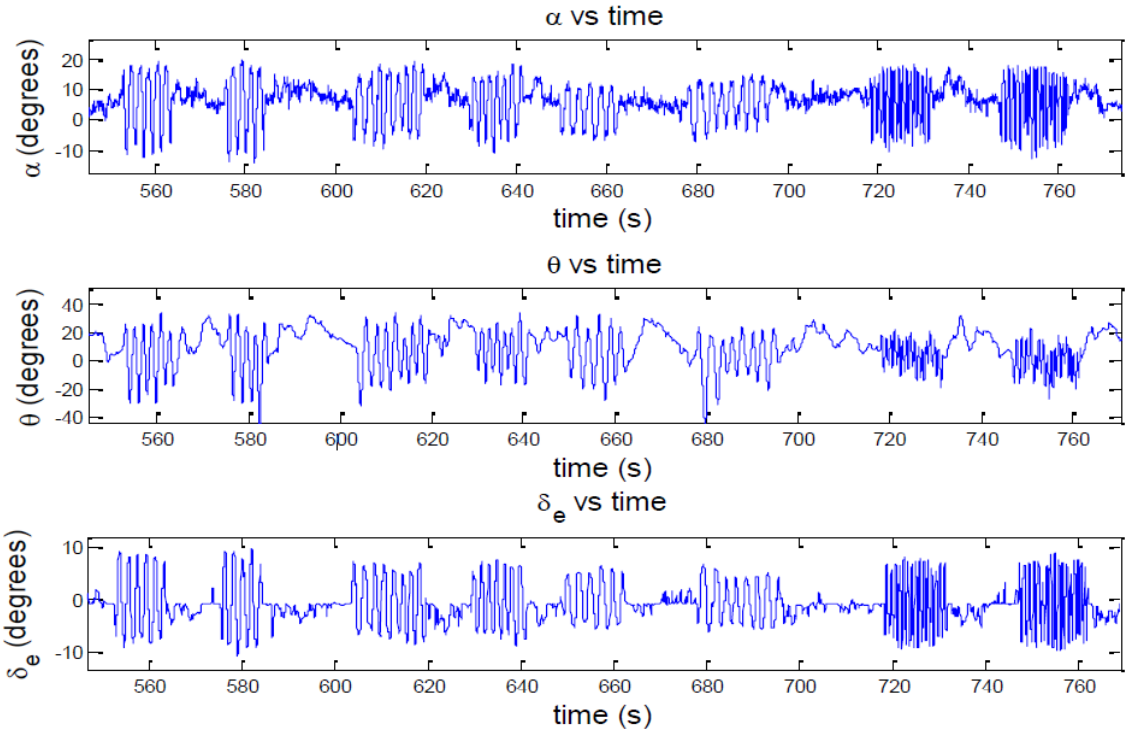

Figure 5.6: Elevon doublet flight data at multiple frequencies.

5.5.1.2 Stall Data

Stall data collected using the 5-hole pitot-tube is shown in Fig. 5.8. This data set was used for both critical AOA based and divergence based stall detection. Seven successful stalls can be observed in Fig. 5.8, which are accompanied by large drops in pitch (up to 50 degrees).

The airspeed and attitude measurements from the flight data using the EagleTree pitot-tube is shown in Fig. 5.9 and Fig. 5.10. Different stall types are labeled in Fig. 5.9. It can be observed that all stalls occurred under 10 m/s except for the turn stall. The lowest airspeed recorded was 3

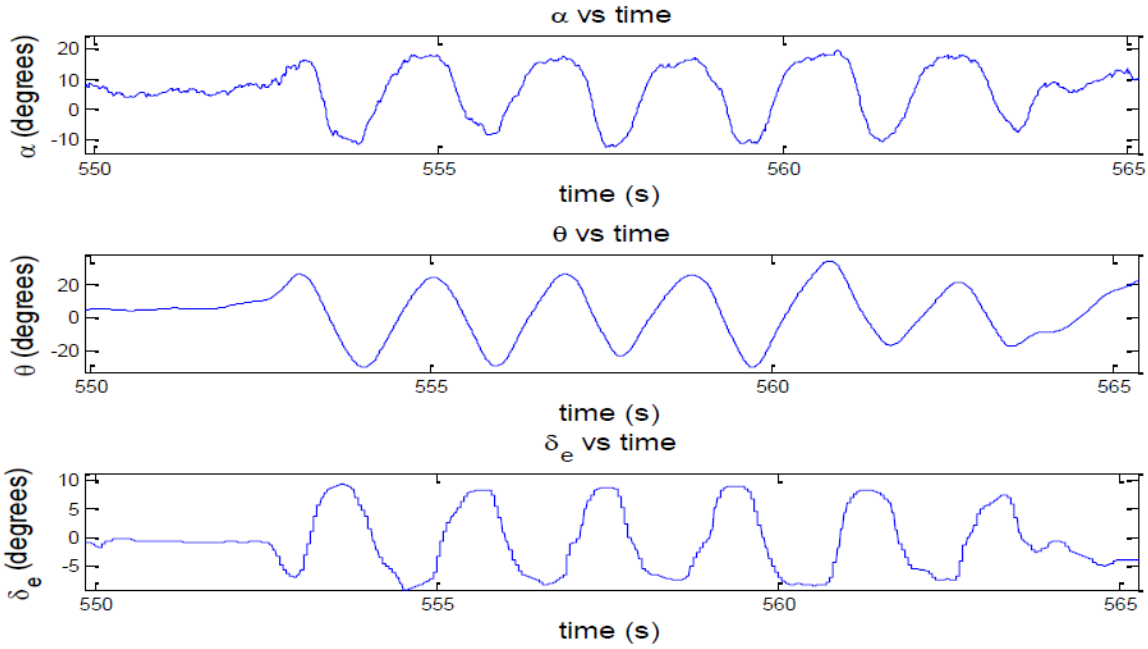

Figure 5.7: Elevon doublet flight data at 0.5 Hz.

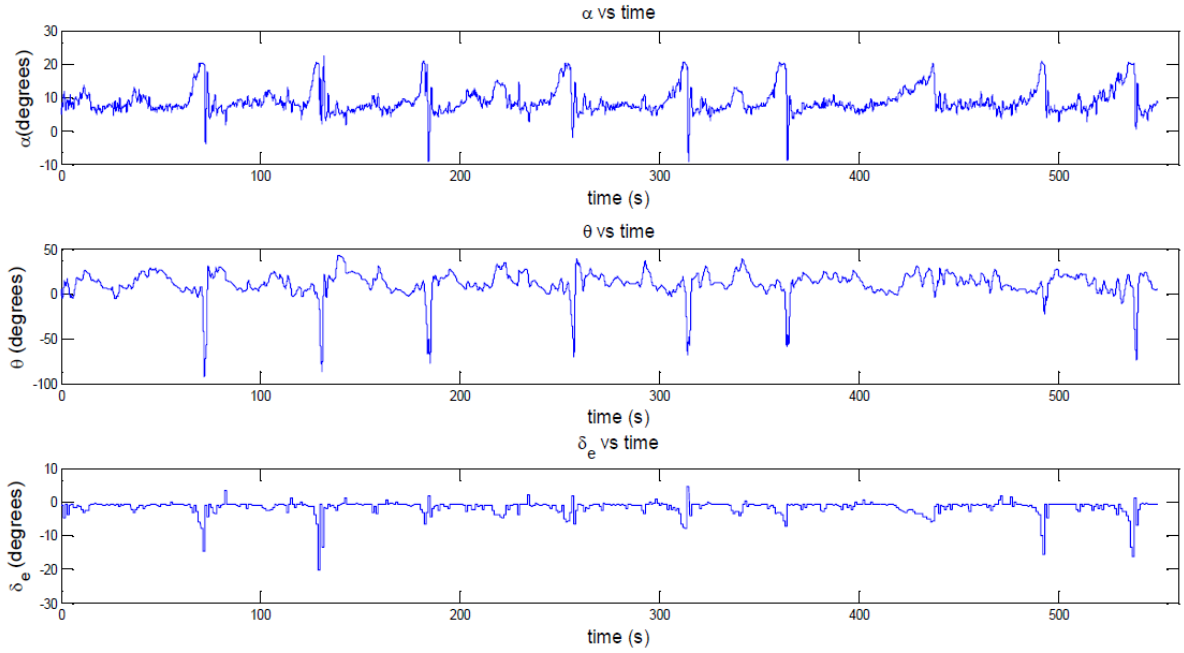

Figure 5.8: Stall data from 5-hole Pitot tube flight.

m/s for the vertical stall. Most stalls occurred around 8.5 m/s. The turn stall occurred at around 11 m/s. Additionally, not all power on/off stalls produce spins.

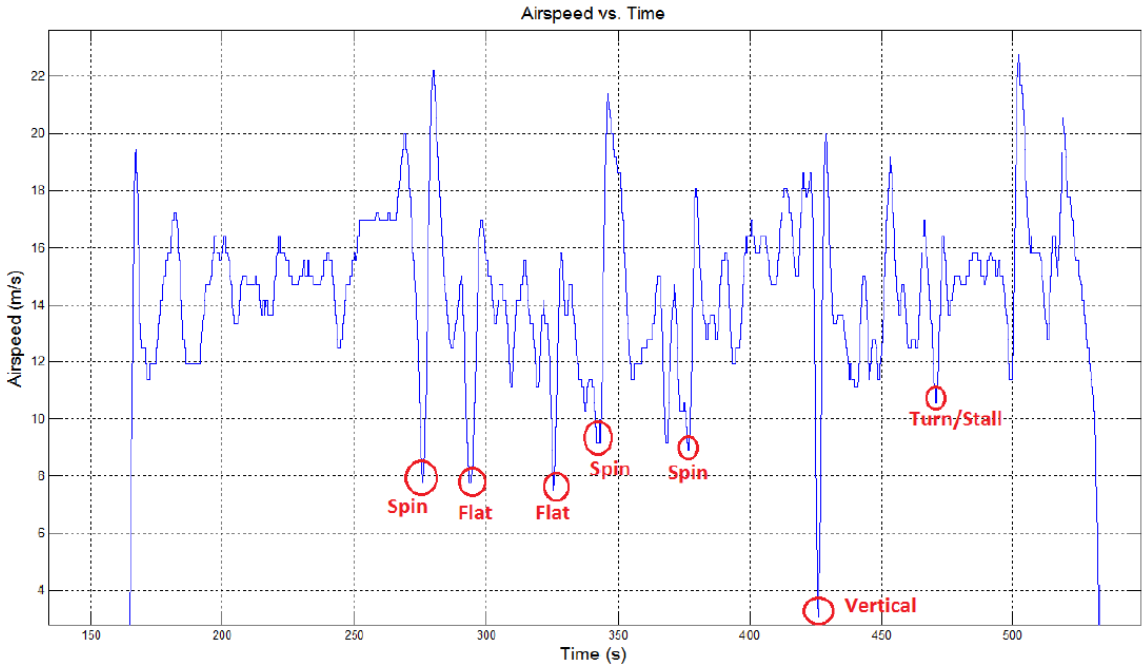

Figure 5.9: Stall data from EagleTree flight.

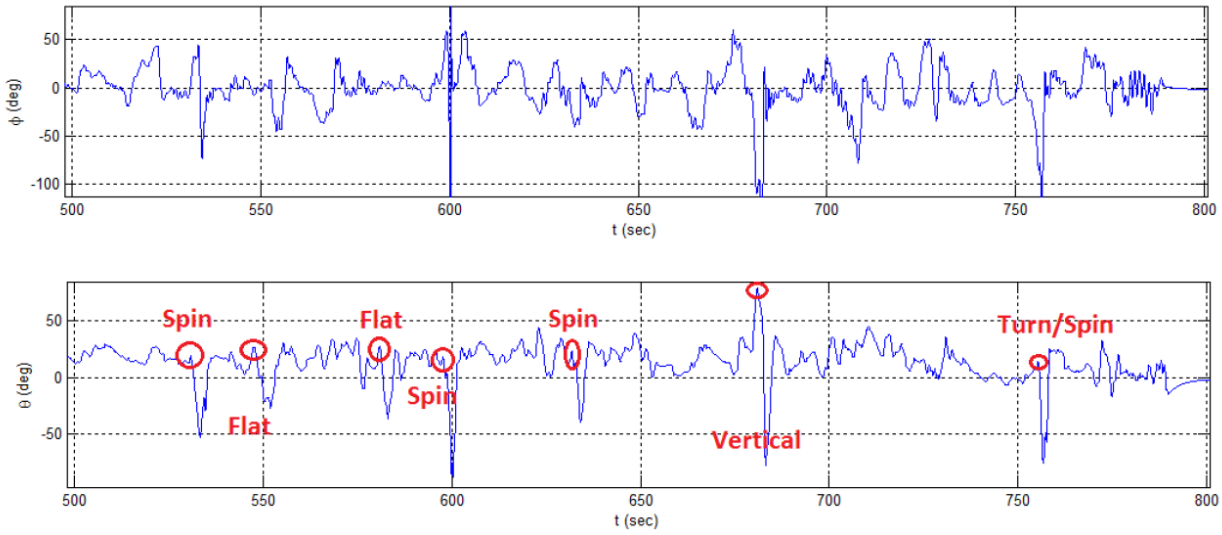

Figure 5.10: Roll and pitch angles for the EagleTree flight data set.

5.5.2 Flight Data for Lift Coefficient Identification

Aircraft stability and control derivatives can be estimated using flight test data with or without flow angle measurements [57]. In this chapter, lift coefficients derivatives are identified using the least squares method. Fig. 5.11 shows the relationship between $\overline{C_L}$ and AOA during elevator chirp

maneuvers with red being a positive deflection (1 to 7 degrees), blue being a negative deflection (-7 to 1 degrees), and green being no deflection (0 degree). The data used to calculate $\overline{C_L}$ and the lift coefficients were filtered through a low pass filter to eliminate high frequency noise. $\overline{C_L}$ as estimated from accelerometer and dynamic pressure readings. It is worth mentioning that the C_L curve will go up or down when the elevator is deflected at different angles. Positive elevator creates positive camber which raises the C_L curve and negative elevator creates negative camber which drops the C_L curve. Therefore, elevator effect has to be considered when calculating lift coefficients for a flying wing aircraft. Fig. 5.11 also shows the linear relationship between C_L and AOA after removing gyro rate and elevator effect, which provides a validation for the proposed method. The linearized portion of lift coefficient ($C_{L_{0+\alpha}}$) is shown in Fig. 5.11.

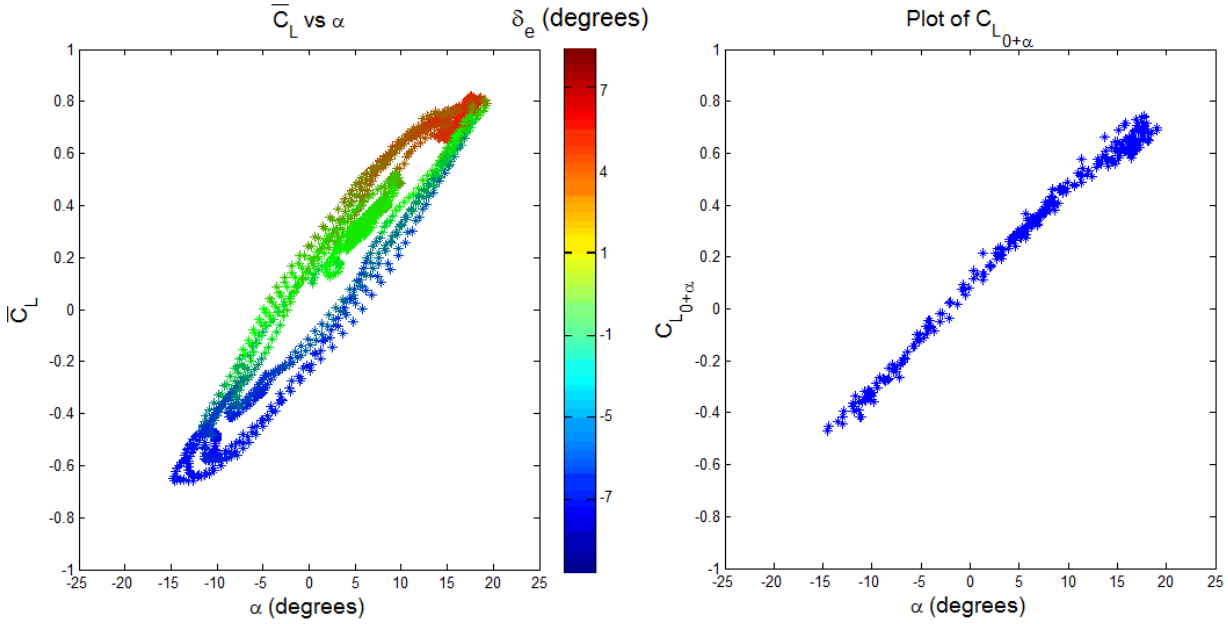

Figure 5.11: $\overline{C_L}$ vs AOA (left) and $C_{L_{0+\alpha}}$ vs AOA (right).

The lift coefficients can be identified from the elevator doublet data set using least squares method. The identified parameters for the KHawk 55 UAS are:

$$C_{L_0} = 0.0563,\ C_{L_\alpha} = 1.8789\ rad^{-1},\ C_{L_{\delta_e}} = 0.8297\ rad^{-1},\ C_{L_q} = 0.1796\ s/rad \tag{5.10}$$

$$C_{L_{0+\alpha}} = C_{L_0} + C_{L_\alpha} = \overline{C_L} - C_{L_{\delta_e}} \delta_e - C_{l_q} q \tag{5.11}$$

After the identification of lift coefficients, C_L curve can be calculated to show the relationship between C_L and AOA at different elevator deflection angles, assuming zero pitch rate. The results are shown in Fig. 5.12 to depict the large effect the elevator deflection has on the lift coefficient for a flying wing aircraft.

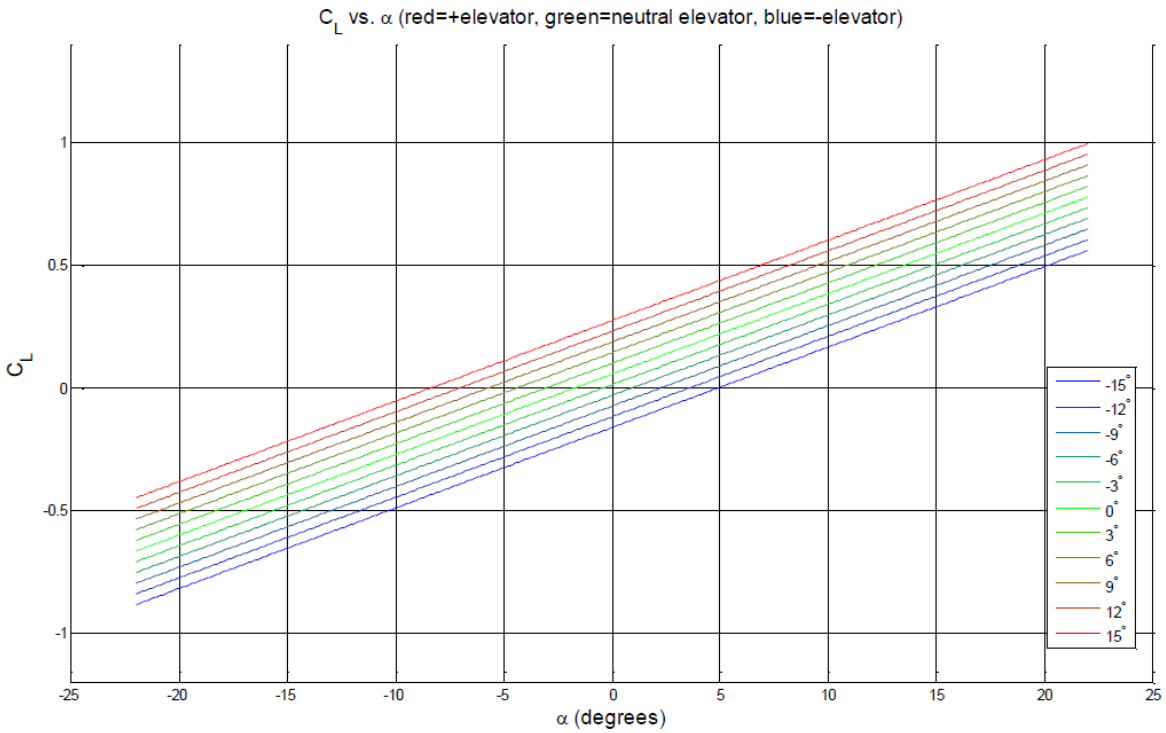

Figure 5.12: C_L vs AOA based on elevator deflection.

5.5.3 Inertial AOA Estimation

The identified lift coefficients will be used in the complementary filter for the estimation of inertial AOA, after combining control commands and inertial/pressure measurements. The initial value for AOA was chosen as zero, which then converges to the estimated alpha using the IMU and elevator data. The ω_n and ζ used in the complementary filter were selected as 10 rad/sec. and 0.7071. The ω_n was selected based on offline tuning using the 5-hole pitot-tube measurements as the ground

truth. The complementary filter is tuned in a way such that the filter generates little phase delays since AOA may be used for flight control purposes. Fig. 5.13 shows the estimated AOA and the true value measured by a 5-hole pitot-tube for 0.5 Hz elevator doublet data.

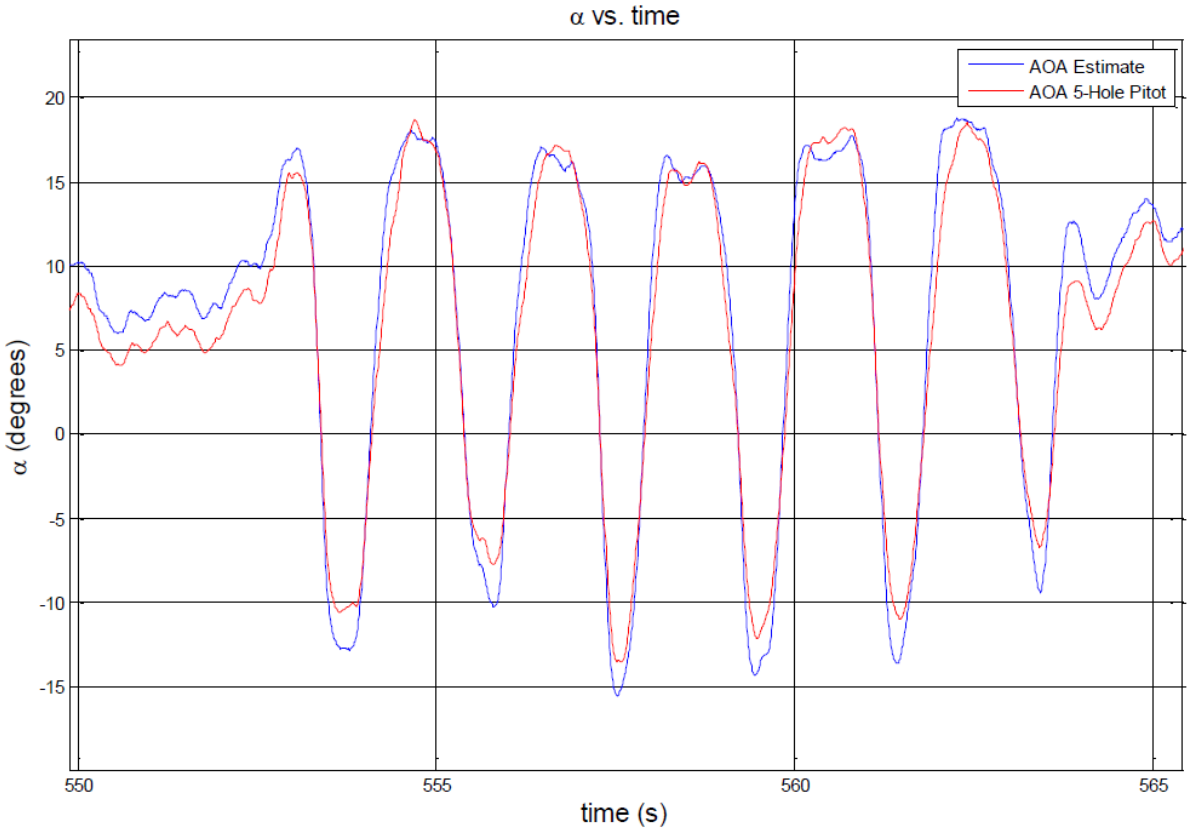

Figure 5.13: AOA estimation results using 0.5 Hz elevator doublet data.

5.5.4 Inertial AOA Based Stall Detection

Fig. 5.14 shows the comparison of the estimated inertial AOA and the measured AOA from 5-hole pitot tube during three stall maneuvers. The large spike in the second stall is caused by an airspeed measurement failure because the 5-hole pitot-tube saturated after entering the stall. An incorrect airspeed of 9.5 m/s was used by the complementary filter when the 5-hole pitot-tube stopped working. Fig. 5.15 shows a close up of the first stall. A large drop in AOA around 72 seconds can be observed which is due to a large drop in a_{z_s} the same time. This is the moment when the aircraft entered a stall after exceeding 19 degrees AOA.

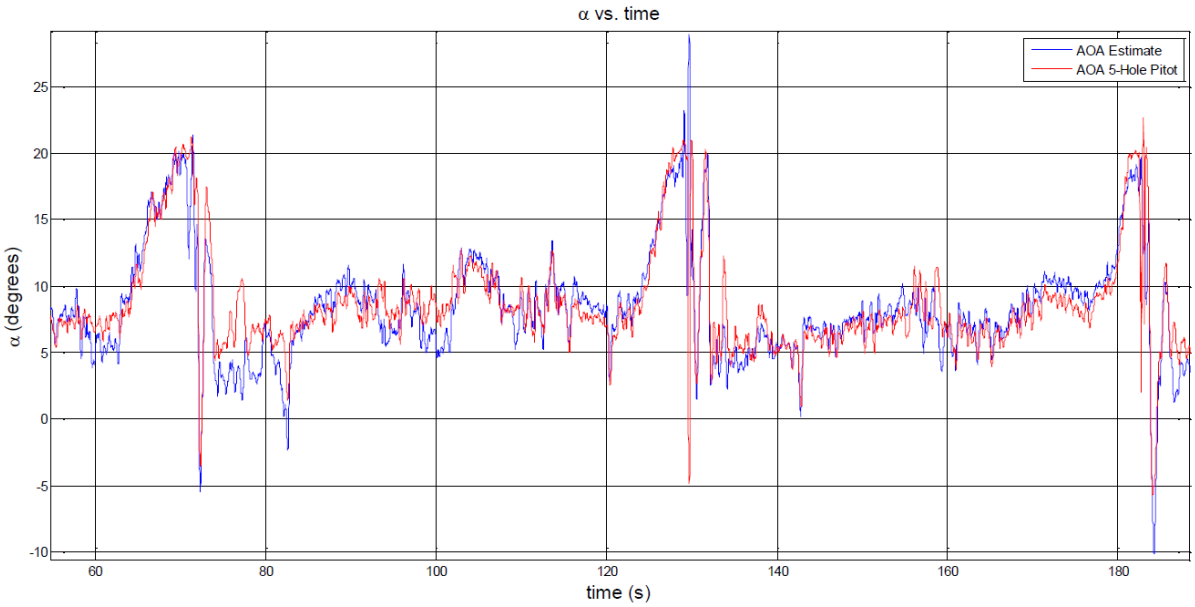

Figure 5.14: Inertial AOA vs measured AOA during Stalls.

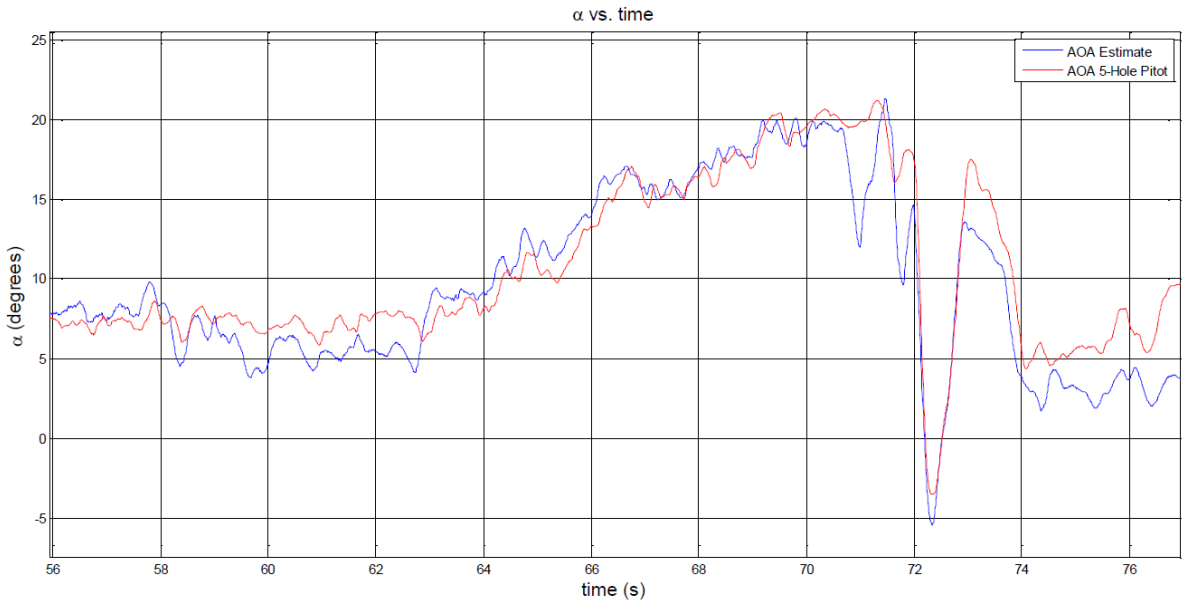

Figure 5.15: Inertial AOA vs measured AOA during a Stall.

In addition to the three high AOA stalls, the proposed algorithm is also tested on a turn stall. Fig. 5.16 shows the measured and estimated AOA from a turn stall performed by the KHawk 55 UAS. The turn stall was performed at a bank angle of approximately 30-45 degrees. A large drop in AOA can be observed at the 19 degree threshold around 538 seconds. Buffeting can be observed

from the large variations in the AOA estimate before stall and is attributable to the variations in accelerations. The above result showed that the complementary filter still generates reasonable estimate of the AOA even at aggressive bank angles.

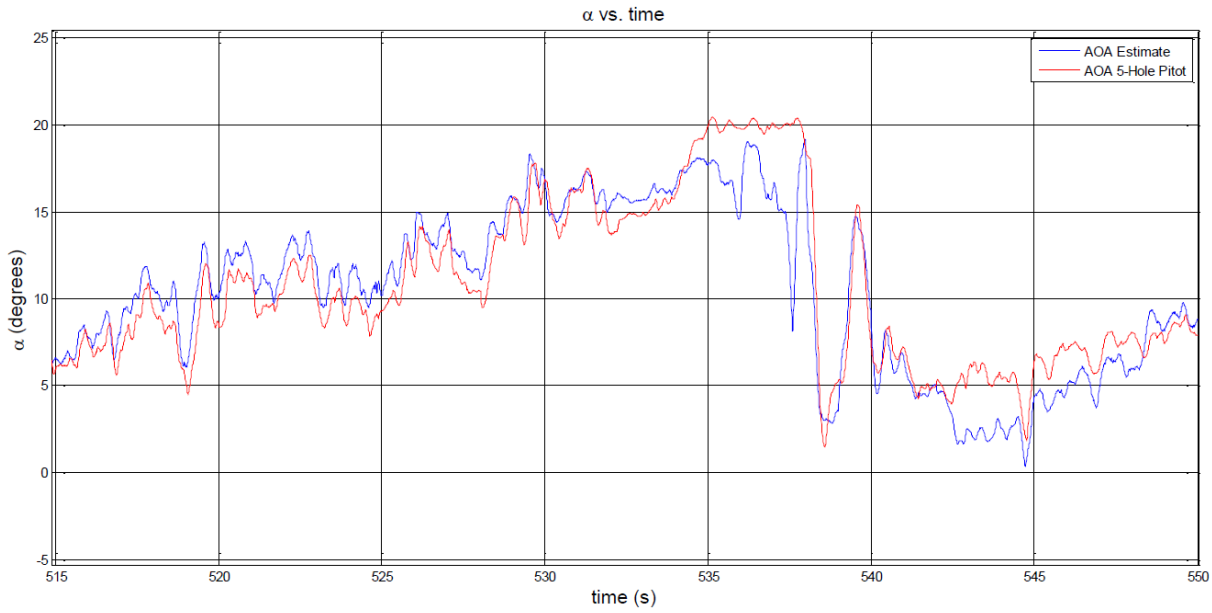

Figure 5.16: Inertial AOA vs measured AOA during a turn stall.

As mentioned earlier, one method to determine whether or not the aircraft is to enter a stall is to set a threshold for the AOA, called critical AOA. This way once the critical AOA is reached, a warning will be sent to either the pilot or controller that a stall is imminent. The critical AOA for KHawk 55 UAS is approximately 19 degrees, based on collected stall data. Fig. 5.17 shows the identified stalls with red dots depicting estimated AOA exceeding 19 degrees. The measured AOA is overlaid for comparison. A potential use for an AOA threshold would be to design an AOA limiter to limit the AOA of the aircraft so that it does not exceed the maximum AOA.

5.5.5 Divergence Stall Detection Results

Roll and yaw divergence analysis was also looked into using flight test data. The detailed results for the Eagle Tree pitot-tube stall data is shown in Fig. 5.18 and Fig. 5.19. It can be noticed that flat stalls are not detectable using the divergence analysis while spin stalls can be easily distinguished

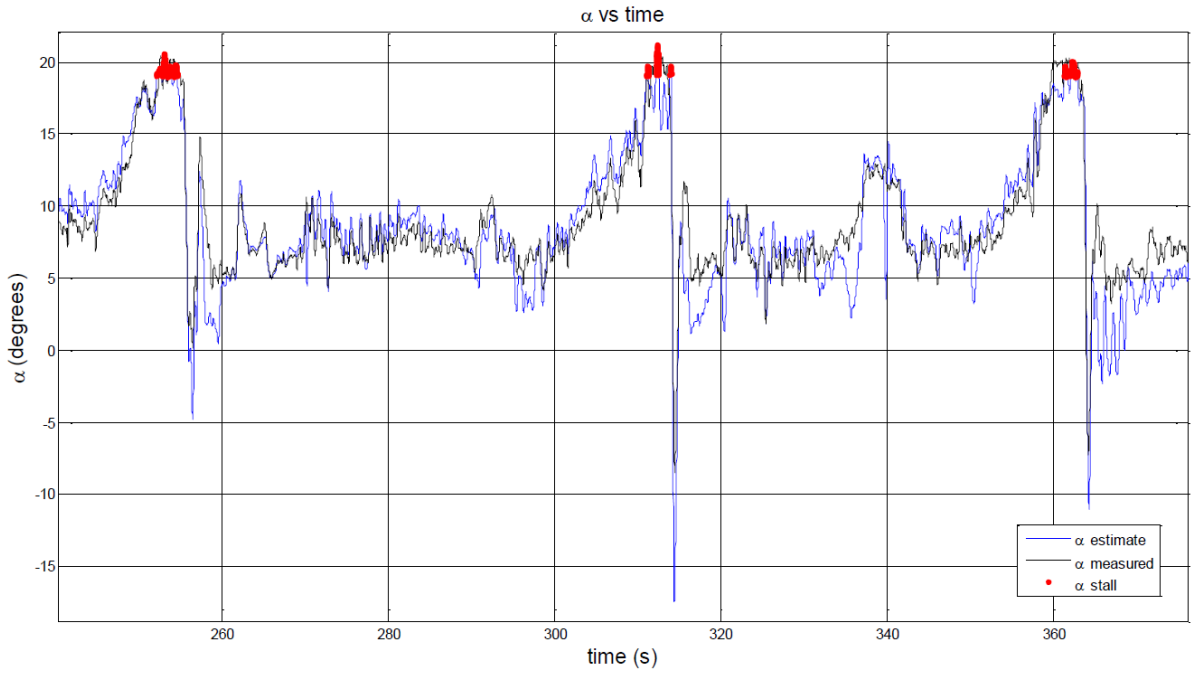

Figure 5.17: AOA estimate with 19 degree threshold.

from the nominal flight envelope.

The divergence analysis using the Aeroprobe 5-hole pitot-tube stall data is shown in Fig. 5.20 and Fig. 5.21. It can be observed that spin stall data tends to be near or past the parameter of bulk stable flight data using the roll/yaw divergence method. Flat stalls are not noticeable using the roll or yaw divergence method. Low AOA flight produced a very tight flight envelope data set. Spin stalls are very evident in comparison to low AOA data. The slower the rate the plane turns or yaws at, the sooner a spin could potentially be identified. In addition, the divergence analysis may not work well if the plane is highly aerobatic. The roll or yaw divergence method is most useful for confirming a spin stall.

In summary, the proposed algorithm can provide accurate estimation of AOA even during stalls, and inertial AOA is a good indicator for stall as shown by the data. This method successfully identified each stall that the pilot had identified. The divergence method only provided a mechanism for detecting spin stalls, but would not provide a reliable detection method for non-spin stalls. It may be more difficult to use the divergence method for spin detection since an aerobatic aircraft

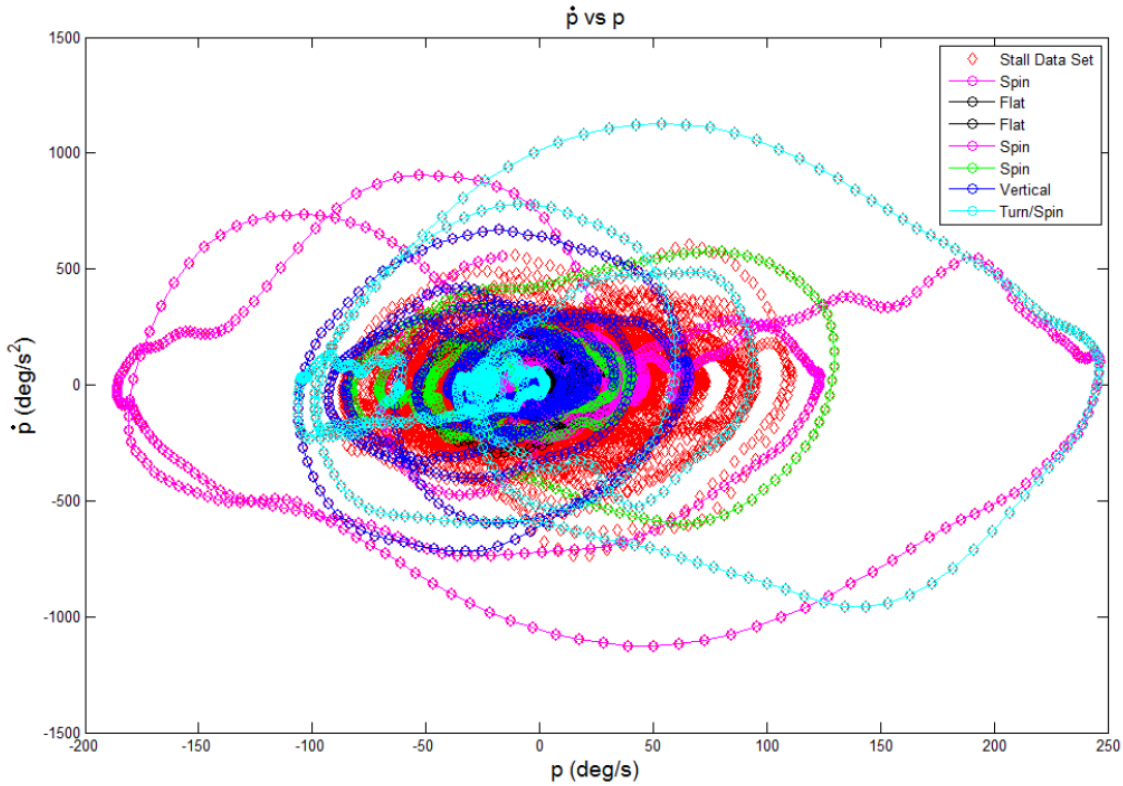

Figure 5.18: Roll divergence.

such as KHawk 55 UAS will naturally rotate faster.

5.6 Conclusions

This chapter provided a systematic approach for generating representative stalls using a small UAS and a detailed analysis of several representative stall detection algorithms. A new inertial AOA based stall detection algorithm is proposed and validated using collected flight data. It is observed that the inertial AOA estimation method can estimate the UAS stall accurately without using flow angle sensor measurements. Additionally, the divergence approach can easily identify spin stalls, but may not work for flat stalls. Future work will be focused on the validation of the proposed method on conventional tailed UAS, aerodynamic modeling of the aircraft's post stall behavior, and associated stall mitigation strategies such as AOA limiter controller design.

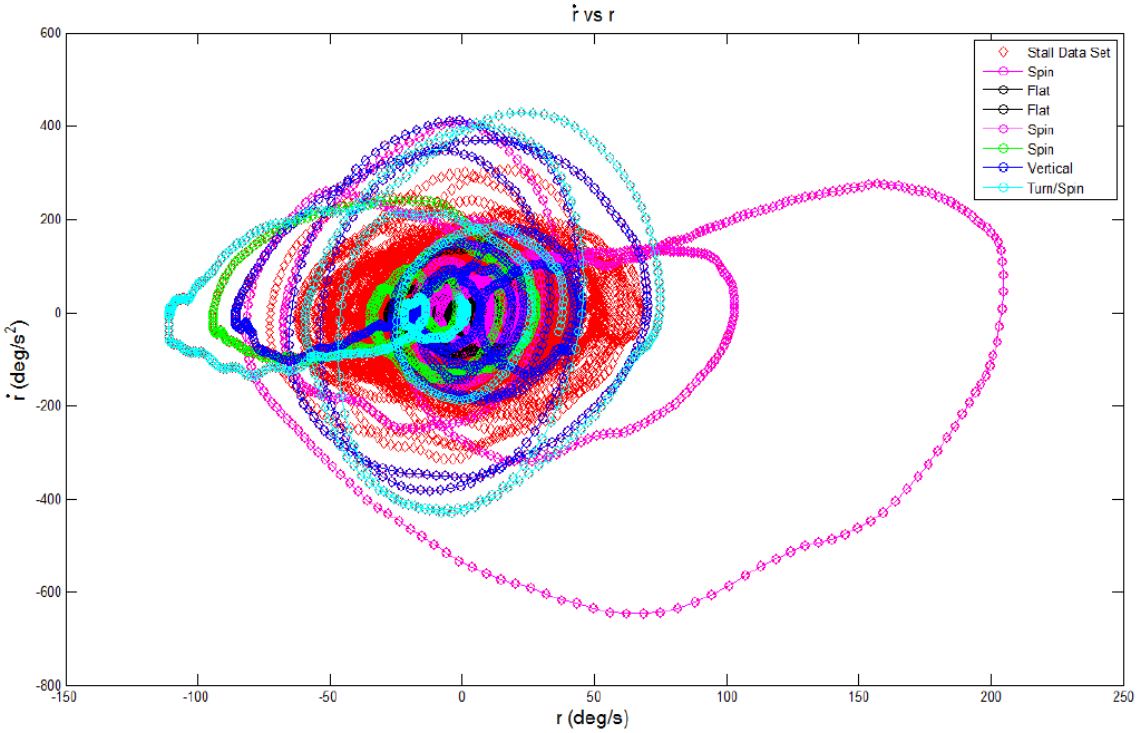

Figure 5.19: Yaw divergence.

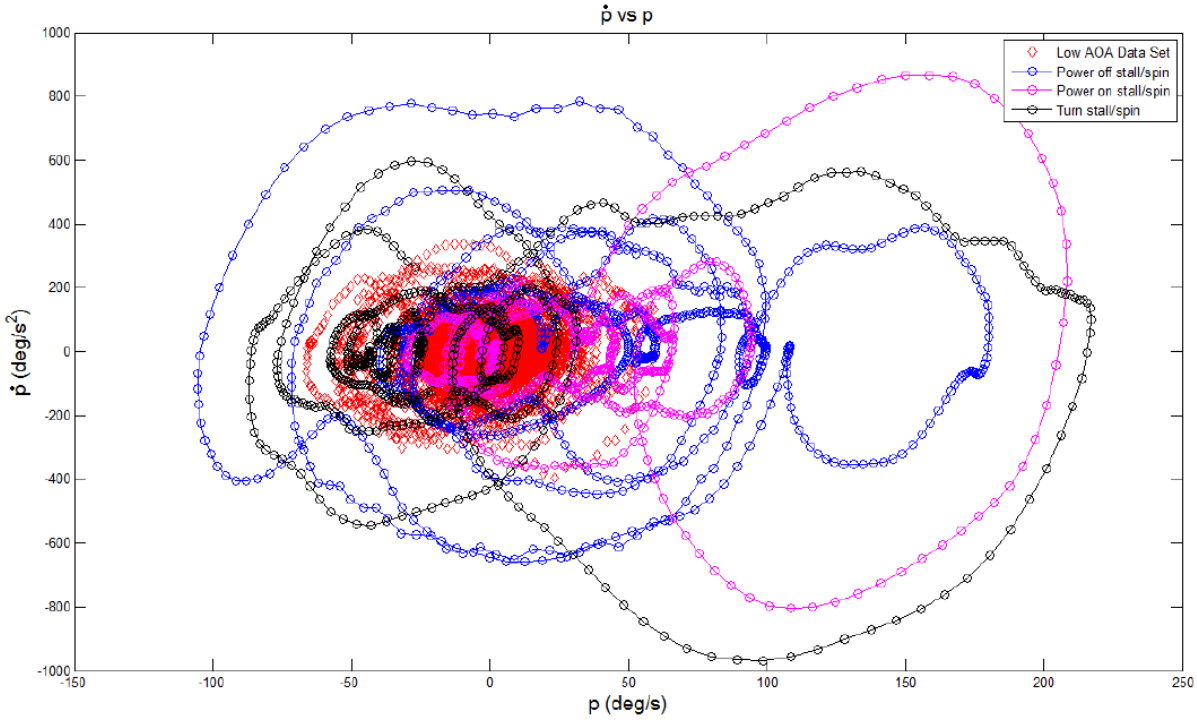

Figure 5.20: Roll divergence.

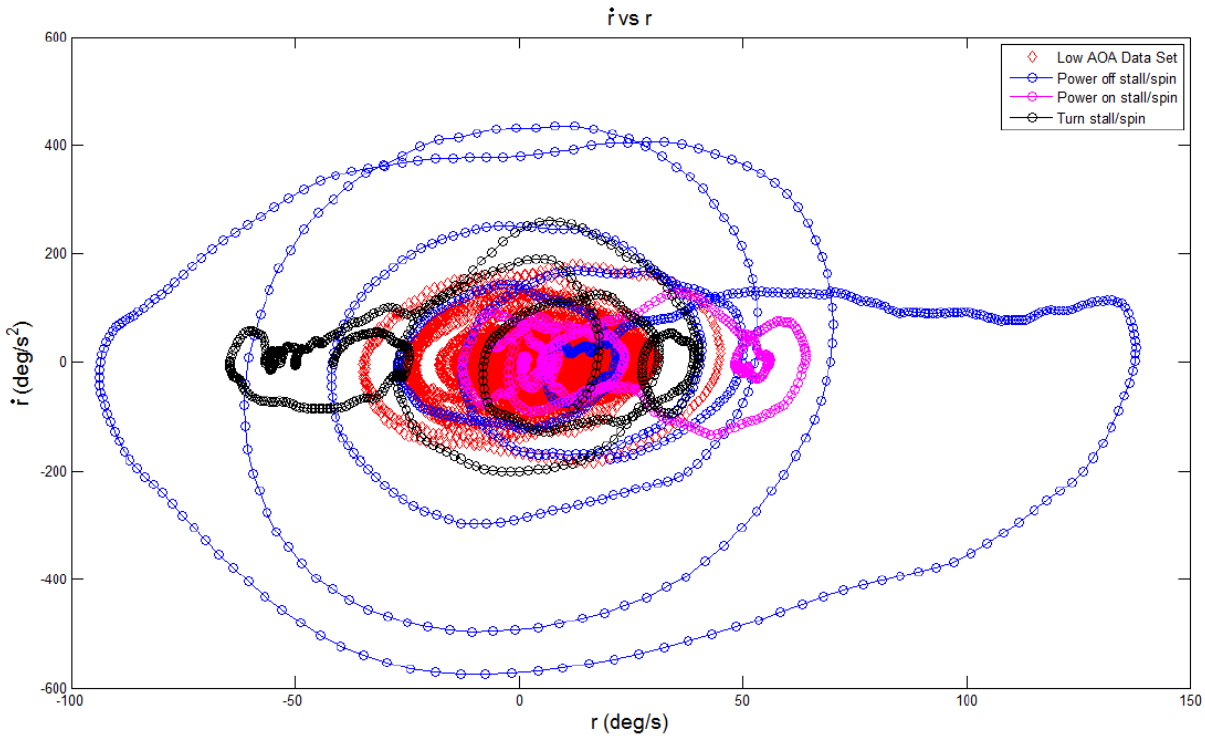

Figure 5.21: Yaw divergence.

Chapter 6

Fire Wind Sensing and Reconstruction Using KHawk UAS

Abstract

This chapter focuses on UAS based fire wind and turbulence sensing by flying a small flying-wing UAS equipped with a standard sensing suite and a 5-hole probe over a controlled burn fire. The UAS measured wind velocity is examined and compared to ground based weather station data. The turbulence kinetic energy (TKE) is also examined and shows higher levels of TKE for the controlled burn flight in comparison to previous calm-day flights.

6.1 Introduction

UAS have been widely used for many challenging military and civilian applications over the past decades, such as navigation through cities [10; 11], disaster monitoring [58], and fire monitoring [8; 59; 60; 61]. Smaller, cheaper, and more powerful avionics sensors and payloads [7], have been increasingly used on small UAS for these dangerous missions [6]. One good example is UAS based wildfire monitoring due to UAS's ability to fly to and assess dangerous places without directly endangering human life (such as a pilot). The amount of damage caused by uncontrolled forest fires including private and public property loss, loss of human life, and its impact on the environment [62; 63], is another obvious reason for the increased interest for any kind of technology that can be used to track and predict the fire spread direction and intensity.

UAS have been used in fire tracking and assessment based on aerial data from NIR, thermal infrared, and RGB cameras [59; 8; 64; 65]. Multiple UAS can be used in coordination with each other and fire fighters on the ground to monitor fire spread direction [66]. In addition, small

wind measurement devices such as a sonic anemometer [67] can also be attached to a small UAS for meteorological measurement such as mean wind direction and magnitude. These small wind devices can also be fitted with temperature, humidity, and pressure sensors for additional data acquisition. Small UAS could also potentially be used for the purpose of fire extinguishing with the use of fire-extinguishing balls [68] that could be dropped from a drone and extinguish a circle of grass measuring one square meter.

To successfully engage in any of the UAS fire missions stated above, an understanding of the turbulent environment is necessary for the development of a robust controller that can safely fly the UAS during fire generated turbulence encounters. While the use of UAS to investigate wildfires for their destructive nature and directional flow has risen in popularity, literature regarding controller design for the unique environments that fires create are relatively few. Furthermore, literature regarding the specific type of turbulence experienced by UAS while flying over wildfires are also minimal. The only comparable literature is from the encounter of thermals by small UAS [69; 70; 71; 72]. Research into the effect of thermals on UAS gliders generally focus on how the thermal energy can be exploited to generate lift and increase the potential energy of the UAS glider. Similarly, fires generate large amounts of energy which could be transferred to a UAS via fire generated thermals, but can also produce significant disturbances.

This chapter investigates the interaction between a small UAS and fire generated turbulence as it is flown above a prescribed grass fire. The UAS utilizes a conventional data acquisition suite (IMU, GPS, pitot tube) as well as cameras which can be used to visually confirm the interaction between the UAS and fire generated turbulence. The chapter will investigate the effects of the fire on the UAS such as the acceleration, attitude, and controller interaction, as well as the measurable transfer of energy to the UAS from the fire generated turbulence in the form of turbulent kinetic energy (TKE).

The chapter is organized as follows: Section 6.2 is the problem statement and UAS wind measurement methods. Section 6.3 focuses on the UAS fire flight data set. Section 6.4 is flight data analysis. Section 6.5 is the conclusion.

6.2 Problem Statement

The main objective of the controlled burn flight presented in this chapter is to estimate and rebuild the prevailing wind and turbulence information in a typical prescribed fire site through both ground weather station and aerial UAS observations. As the UAS is flown over the fire, measurements will be taken and logged using a standard UAS sensing suite (IMU, GPS, Pitot tube) in order to identify fire generated turbulence. Several methods will be used in this chapter for identifying turbulence generated from fire and will include:

1. Video confirmation. On-board video confirmation will be used to determine turbulence.

2. Accelerometer data. Turbulence can be identified from spikes in acceleration. The flight controllers of the UAS are usually pre-tuned in calm or light wind conditions with the objective to minimize the turbulence impact. Therefore, spikes in acceleration for UAS with closed-loop controller activated can potentially be used as a major indicator from turbulence.

3. Attitude data including orientation estimates and rotation rates from gyros. Spikes in $p/q/r$ and $\phi/\theta/\psi$ can be used to determine turbulence for open loop or closed loop flight control systems.

4. Simulation vs real data. Deviations from the theoretical dynamic model predictions can be compared to the real flight data during straight line flight.

5. Wind measurements. Wind measurements using a multi-hole pitot tube or sonic anemometer on-board the UAS can be used to determine spikes in turbulence and wind. Data is usually collected during UAS straight line flight or hover mode for most consistent results. Wind measurements from the ground can also be used for comparison. Metrics such as turbulent kinetic energy (TKE) can be derived from the direct wind measurements for turbulence detection under different weather conditions.

6.2.1 Wind Measurements from UAS

Wind measurements can be taken with a UAS with the aid of a multi-hole Pitot tube or with a sonic anemometer (sonic anemometers have been used on quadrotor UAS [67]). From the GPS, inertial, and air data measurements, the body frame velocity components can be calculated [7].

$$\begin{bmatrix} u \\ v \\ w \end{bmatrix} = V_a \begin{bmatrix} cos\alpha cos\beta \\ sin\beta \\ sin\alpha cos\beta \end{bmatrix} \tag{6.1}$$

The wind speed (w_n, w_e, w_d) is calculated by rotating the body frame air speed (u, v, w) into the north-east-down (NED) frame and subtracting it from the NED local frame ground speed (V_n, V_e, V_d). This is shown in the equation below [73].

$$\begin{bmatrix} w_n \\ w_e \\ w_d \end{bmatrix} = \begin{bmatrix} V_n \\ V_e \\ V_d \end{bmatrix} - R_b^n(\phi, \theta, \psi) \begin{bmatrix} u \\ v \\ w \end{bmatrix} \tag{6.2}$$

The NED ground speed is provided from the GPS receiver and can be further estimated/interpolated using an Extended Kalman filter [32]. The body to NED rotation matrix $(R_b^n(\phi, \theta, \psi))$ is shown in the following equation [7; 73].

$$R_b^n(\phi, \theta, \psi) = \begin{bmatrix} cos\psi cos\theta & -sin\psi cos\phi + cos\psi sin\theta sin\phi & sin\psi sin\theta + cos\psi sin\theta cos\phi \\ sin\psi cos\theta & cos\psi cos\phi + sin\psi sin\theta sin\phi & -cos\psi sin\phi + sin\psi sin\theta cos\phi \\ -sin\theta & cos\theta sin\phi & cos\theta cos\phi \end{bmatrix} \tag{6.3}$$

6.2.2 Wind Models

6.2.2.1 Wind Shear Model (Prevailing Wind)

The weather station data can be collected using a sonic anemometer on the ground at the preset height ranging from 1-5 meters. For comparisons between ground prevailing wind measurement and UAS based estimates at higher altitudes, a wind shear model can be used. The magnitude of the ground weather station measurements usually needs to be scaled up to make it comparable to the wind velocities experienced by the UAS, due to boundary layer effect. This variation in wind speed is due to the frictional influence the ground has on the UAS. The equation for the empirical power law based wind shear model is shown below [73; 74].

$$V_{W_{shear}} = V_{w_{h_r}} \left(\frac{h}{h_r} \right)^{\gamma} \tag{6.4}$$

For nominal conditions, the Prandtl coefficient (γ) is approximately 1/7 [73], h is the altitude of the UAS, and h_r is the reference altitude the wind speed is measured at (the altitude of the weather station).

6.2.2.2 TKE Calculations

The TKE is calculated as the variance of the wind from the mean ($\bar{w}_n$, $\bar{w}_e$, $\bar{w}_d$) [75; 76; 77; 78; 79]. This is useful as it can determine either immediate turbulent changes to wind speed or persistent turbulence over time. First, the deviation from the mean wind (w'_n, w'_e, w'_d) must be calculated, which is illustrated in Fig. 6.1 (using downward wind as an example) and shown in equation 6.5.

$$w'_{n_i} = w_{n_i} - \bar{w}_{n_i}, \quad w'_{e_i} = w_{e_i} - \bar{w}_{e_i}, \quad w'_{d_i} = w_{d_i} - \bar{w}_{d_i} \tag{6.5}$$

The instantaneous TKE is calculated as the sum of the variance of each wind component divided by 2. This version of the TKE is useful for determining a large burst of turbulence that could be

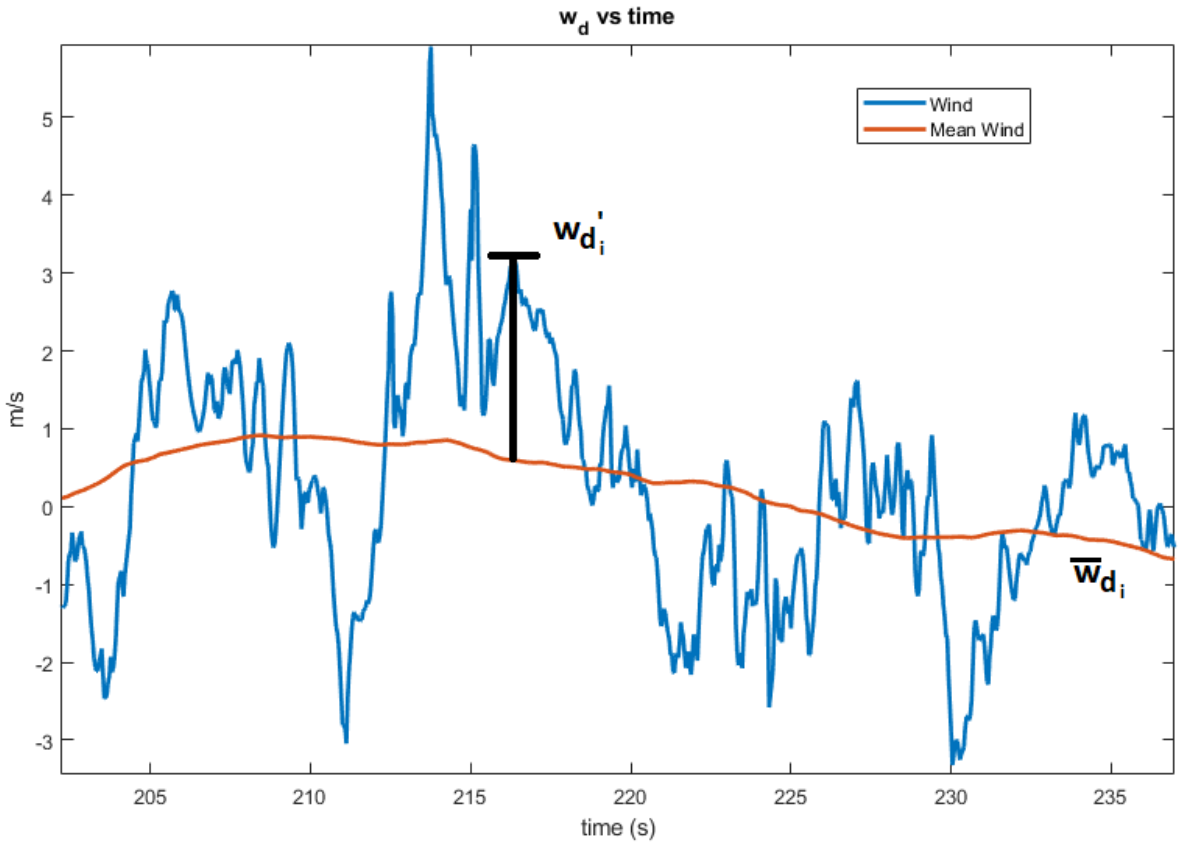

Figure 6.1: Illustration showing downward mean wind and measured downward wind.

encountered while flying near a hazardous area (vicinity of a fire or smoke generated from a fire).

$$TKE = \frac{1}{2}({w'_{n_i}}^2 + {w'_{e_i}}^2 + {w'_{d_i}}^2) \tag{6.6}$$

The cumulative TKE ($\overline{TKE}$) is calculated in a similar manner to the TKE, but instead sums the variance of each wind component. This is shown in the two equations below.

$$\overline{{w'_n}^2} = \frac{1}{N}\sum_{i=1}^{N} {w'_{n_i}}^2 \tag{6.7}$$

$$\overline{TKE} = \frac{1}{2}(\overline{{w'_n}^2} + \overline{{w'_e}^2} + \overline{{w'_d}^2}) \tag{6.8}$$

This version of TKE is useful to determine the turbulence over longer periods of time such as

straight line flight, and can be compared to flight lines at other turbulence levels.

6.3 UAS Fire Flight Data Set

This section focuses on descriptions of the UAS fire flight data set including both flight mission description, collected UAS data set, and initial turbulence detection investigations.

6.3.1 Fire Experiment Description

The data collected in this chapter were acquired from a controlled burn performed by the Kansas Biological Survey (KBS). The controlled burns were created by setting fire to prairie fields consisting of tall grass and prairie flora that were relatively dry. This created a quick and fast moving fire (up to 0.4 m/s for fire rate of spread along the direction of prevailing wind) that created smoke plumes rising several hundred meters and would at times completely engulf the UAS while flying over the fire.

The controlled burn investigated in this chapter occurred on October 8, 2019, at the Anderson County Prairie Preserve, and lasted approximately from 11:38 A.M. to 12:21 P.M.. The prairie field has a size of 530 m X 250 m. The ambient temperature during the fire burning is around 73°F, with a humidity around 44%, and an average wind velocity of 6.26 m/s from the south at about 1.9 m above the ground. In other words, the wind is traveling from the south to north. The controlled burn is set following a ring fire pattern, with two groups starting the fire at the center of the north boundary and moving separately clockwise and anticlockwise along the fire field. The goal for UAS flight is to collect the wind and fire data during the most intense duration of the controlled burn as the fire progresses. The KHawk Thermal Vision UAS was flown over this controlled burn at Anderson County Prairie Reserve and an illustration of the east-west flight path taken by the UAS is shown in Fig. 6.2.

The flight path is created to best track the fire as it progresses and collect as many turbulence encounters during the straight line flight. Straight line flight is the best method for collecting

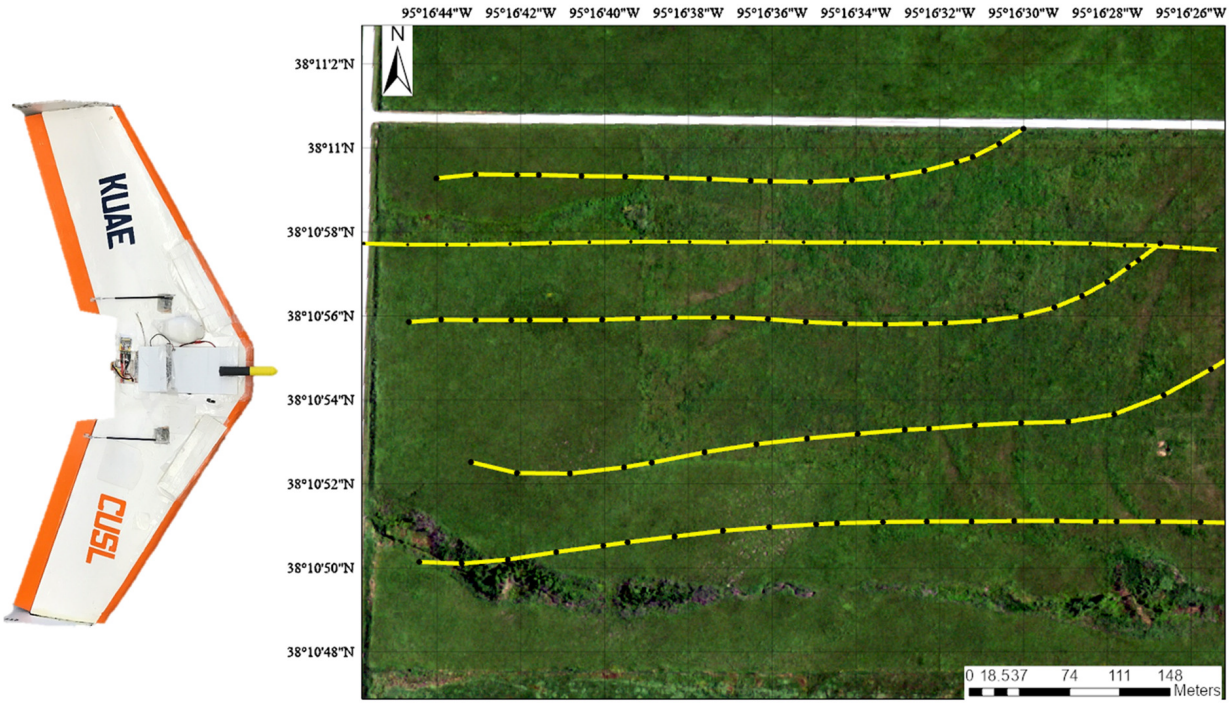

Figure 6.2: Illustration of KHawk Thermal Vision UAS flight path [1].

turbulence data due to inaccuracy in wind measurements during UAS turning. Straight line flight also gives the best chance to compare simulated flight data from controller inputs to real flight data. Note that the KHawk Thermal Vision UAS flew autonomously during the flight. Two UAS flights were performed with each flight lasting 12-15 minutes. The first flight started about 6 minutes after the fire start, which is less turbulent since the fire was mostlly constrained to the north boundary of the field. The second flight started about 30 minutes after the fire start, which has much stronger turbulent encounters with the fire line spreading everywhere in the field.

6.3.2 UAS Fire Flight Data Set

The following airborne data sets have been collected during the flight tests, including:

- 5-hole Pitot tube data from Aeroprobe, $[V, \alpha, \beta]$ in 100 Hz.
- GPS raw data $[V_n, V_e, V_d]$, $[x, y, z]$ in 5 Hz from Ublox GPS receiver.
- Inertial data $[p, q, r]$, $[a_x, a_y, a_z]$ in 25 Hz from Pixhawk Cube autopilot.

- Estimated UAS states $[\phi, \theta, \psi]$, $[V_n, V_e, V_d]$ in 25 Hz from Ardupilot software on-board Pixhawk.
- Thermal images in 1 Hz from FLIR Vue Pro camera.
- NIR video in 29.97 Hz from modified GoPro camera.

6.3.3 Initial Investigation on UAS Turbulence Encounter

The initial investigation was performed using the on-board GoPro footage and accelerometer data to determine the time stamp of the UAS turbulence encounters. Two flight tests were performed for the KHawk Thermal Vision UAS over the controlled burn, with the second flight experiencing the majority of fire generated turbulence. The second flight will be examined in this chapter. The time stamps for turbulence encounters manually determined from the GoPro footage are shown in the Table 6.1. For comparison, Fig. 6.3 shows the accelerometer measurements with the turbulence intervals marked in red, and limits the acceleration data to only straight-line flight with max roll angle variations less than 15 degrees which further helps to visualize the turbulence.

Table 6.1: Turbulence encounters during flight

Encounter #	**Time Stamp (seconds)**
1	109
2	115
3	354
4	364
5	461
6	510
7	530
8	627

Limiting the acceleration data to only straight-line flight eliminates large variations in acceleration from aircraft turns which can be as large as 3 g's or greater. The accelerations in the z-direction are most noticeable in terms of magnitude and strength. Since the autopilot is active during flight, some of the accelerations are from autopilot corrections during the flight. Fig. 6.4 shows a close

up encounter of turbulence at approximately 510 seconds. The elevator (δ_e) is active attempting to correct for the turbulence, but large spikes in acceleration up to approximately $\pm$ 1.5 g's are evident from turbulence. Note: the elevator deflection for turns is generally over 1 degree.

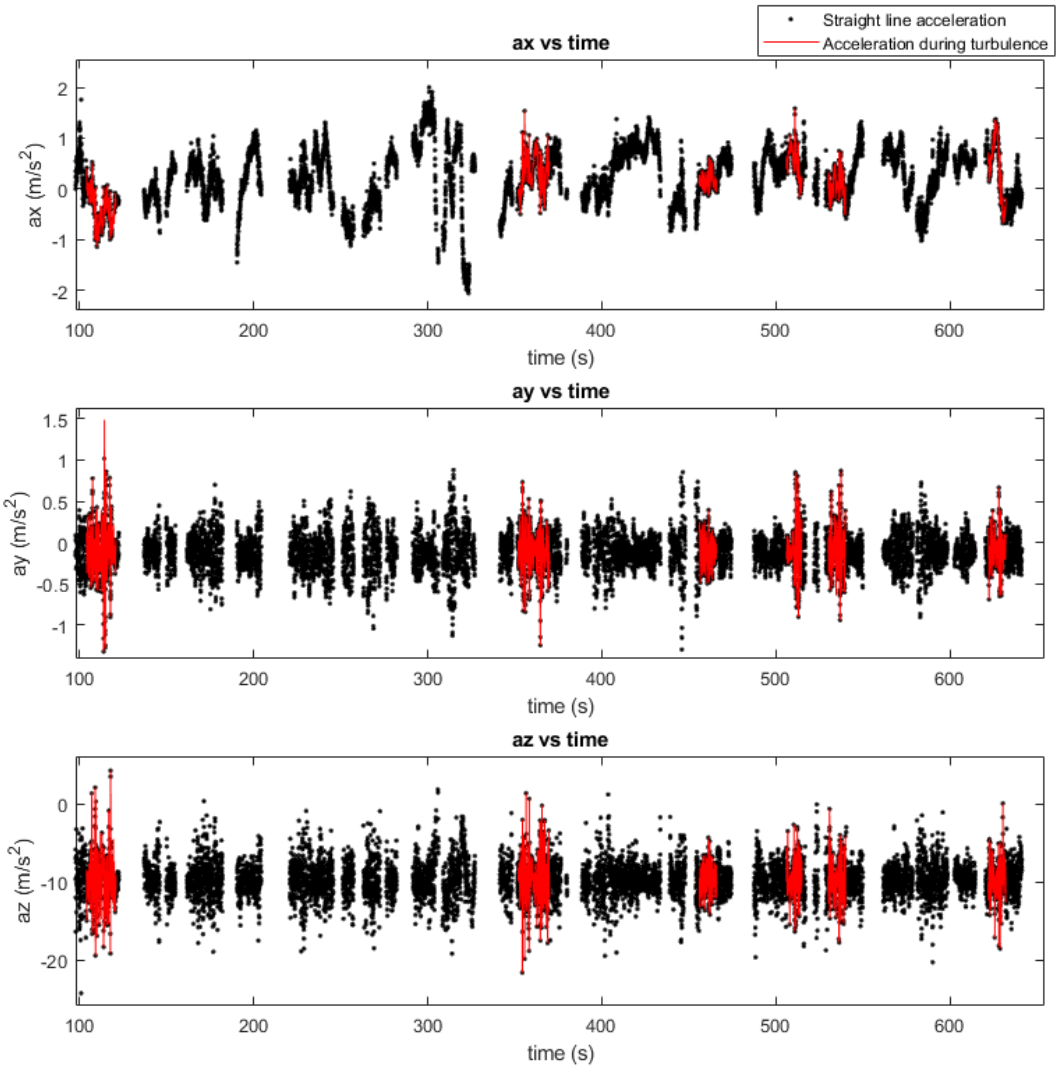

Figure 6.3: Straight line acceleration during flight 2.

6.4 Flight Data Analysis

In this section, wind velocity measurement data from the UAS and the ground weather station will be used for prevailing wind comparison as well as TKE calculations.

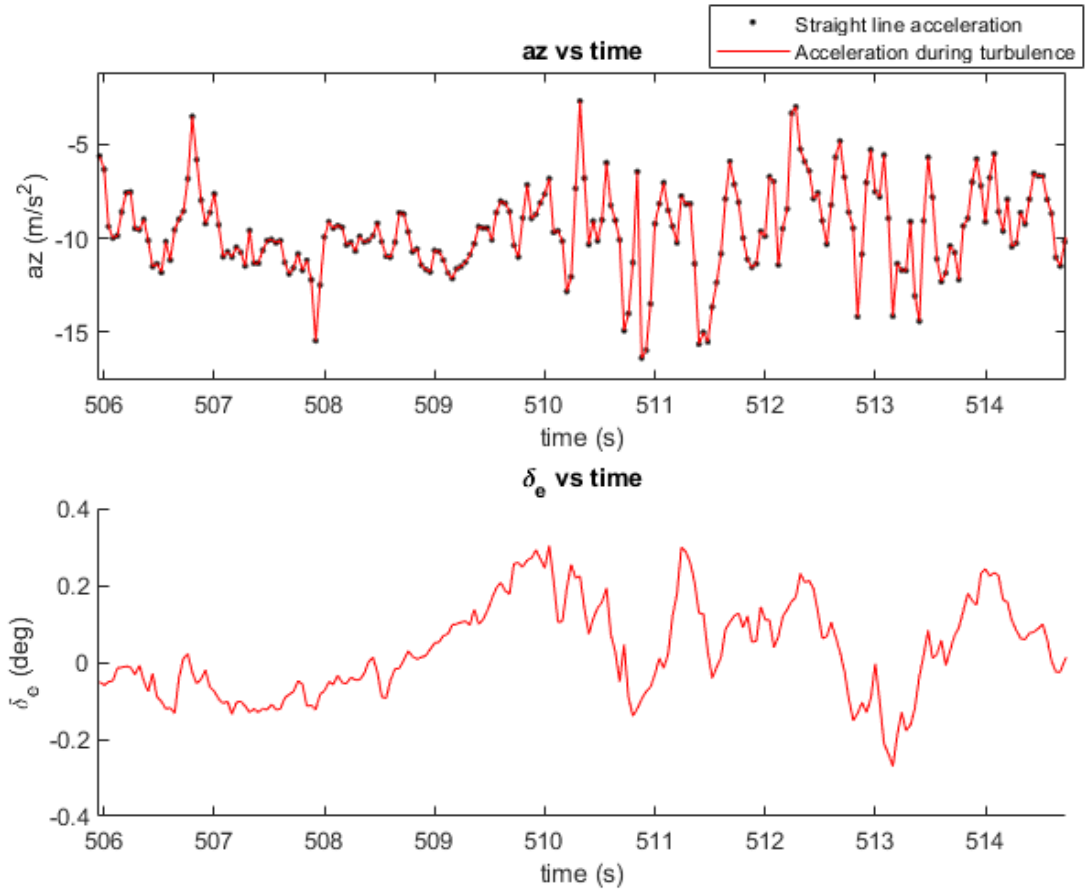

Figure 6.4: Straight line acceleration during flight 2 at 506 seconds (time stamp 6).

6.4.1 Wind Data Analysis

The wind data analysis section consists of comparisons between the KHawk Thermal Vision UAS and the sonic anemometer wind station data collected during the controlled burn flight on October 8, 2019. An additional flight from a calm day at Clinton RC airport on October 3, 2019 will be used for comparison. The weather station data was collected at 100 Hz while the UAS inertial data was taken at 25 Hz.

6.4.1.1 Wind Data Comparison between UAS and Weather Station

The wind data is first calculated using the methods described in section 1.2.1. The KHawk Thermal Vision UAS wind data is then plotted in comparison to the weather station data extrapolated using the wind shear model and a 20 second moving average filter shown in Fig. 6.5. The data presented

in Fig. 6.5 show basic agreement between the mean wind measurements collected by the KHawk Thermal Vision UAS and the weather station. The wind is mostly traveling to the north with small variations in the east and downward direction. An additional check can be performed by creating a quiver plot of the wind speed shown in Fig. 6.6. The quiver plot shows good agreement between the KHawk Thermal Vision UAS and weather station with variations in the direction of the wind changing more dramatically during turns and while the UAS is further away from the weather station.

6.4.1.2 TKE Analysis

TKE analysis consists of both data from a former calm flight and a fire turbulent flight, while focusing on straight line portions of the flight. Instantaneous TKE will first be investigated between the KHawk Thermal Vision UAS and the weather station data for the majority of the flight. The mean wind is calculated after a moving average filter of 20 seconds for both KHawk Thermal Vision UAS and weather station, shown in Fig. 6.7. The obtained mean wind is used in later TKE calculations. The TKE for both the KHawk Thermal Vision UAS and weather station is shown in Fig. 6.8 and includes the distance from the weather station for comparison.

Spikes can be seen in TKE from the KHawk Thermal Vision UAS in relation to the time stamps shown Table 6.1. The weather station TKE is likely larger due to the position of the weather station during the fire. The weather station was positioned on a flat grassland around hay bails and near the fire line. This positioning of the weather station is likely the reason for the large TKE and considerable turbulence evident in Fig. 6.5. To better visualize the TKE, cumulative TKE averaged over a 10 second interval was chosen to compare the TKE to the weather station data with the max TKE being calculated over the 10 seconds. The 10 second intervals were positioned relative to the time stamps shown in Table 6.1 with the majority of the turbulence centered at the 5 second mark. The same calculations were made for straight line flight during a calm day for the purpose of comparison. The results are shown in Fig. 6.9 and Fig. 6.10. The calm flight shows lower levels of weather station TKE and is more comparable to the KHawk Thermal Vision UAS results in terms

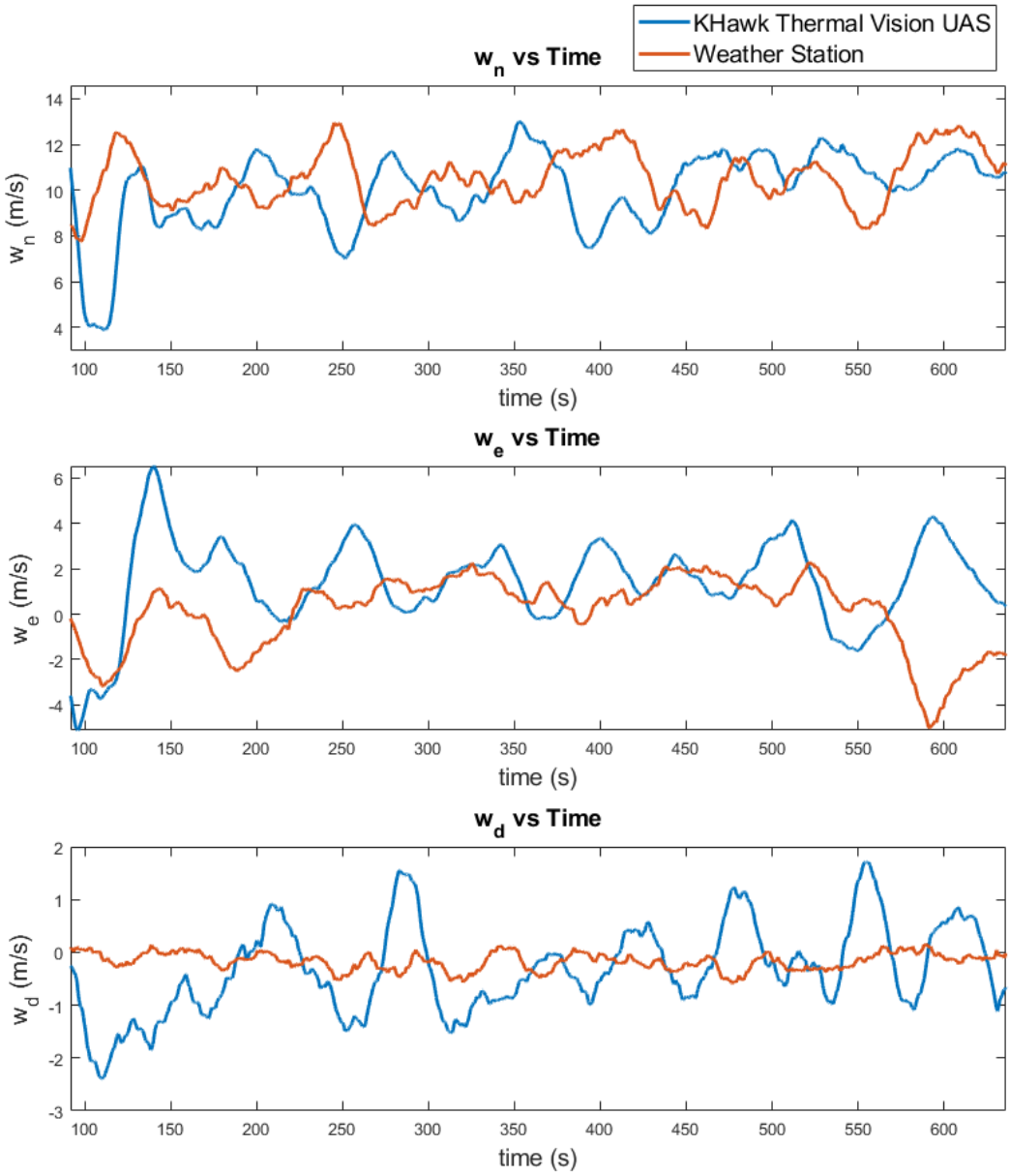

Figure 6.5: KHawk Thermal Vision UAS vs. weather station.

of magnitude. Both plots show similar trends for the KHawk Thermal Vision UAS and weather station TKE in terms of 10 second average and max values. This shows that comparable trends in turbulence can be detected by a wind measuring UAS and weather station nearby. The 10 second average and max TKE for the turbulence flight is also approximately two and three times the size of the calm weather TKE. The mean and standard deviation values for the KHawk Thermal Vision

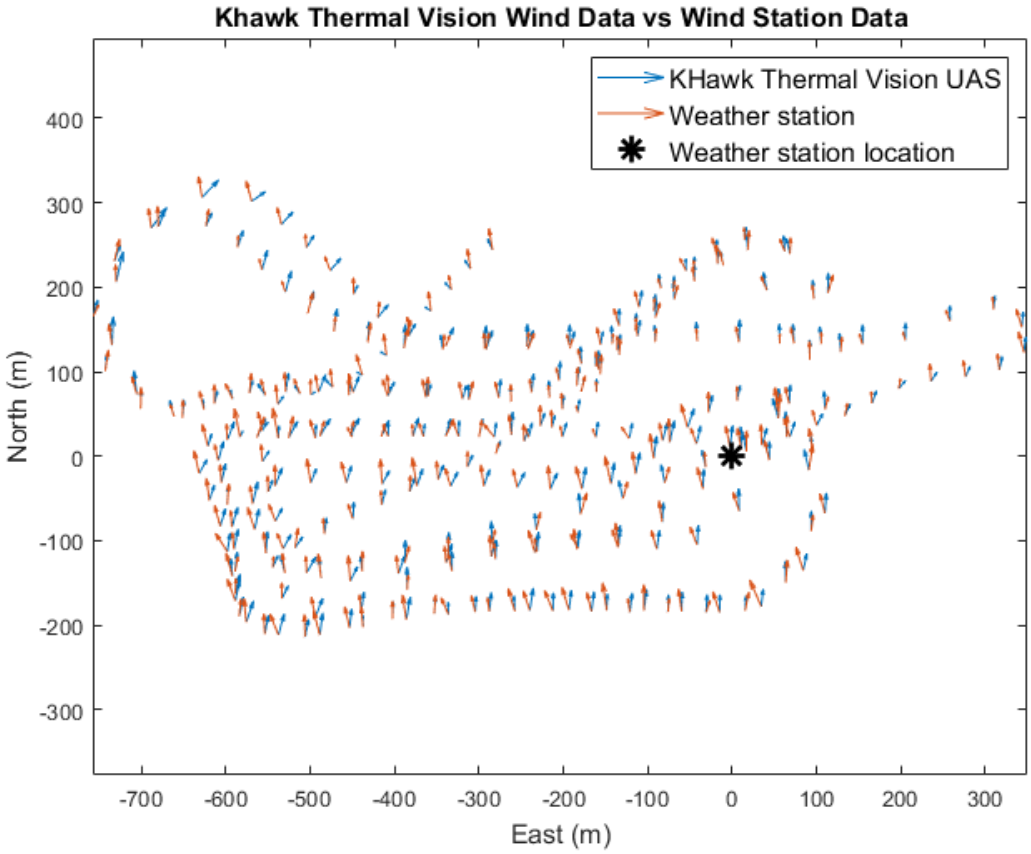

Figure 6.6: KHawk Thermal Vision UAS vs. weather station quiver plot.

UAS and weather station TKE are shown Tables 6.2 and 6.3.

Table 6.2: TKE values for KHawk Thermal Vision UAS

Value	**Controlled Burn Flight** (m^2/s^2)	**Calm Flight** (m^2/s^2)
10 second mean	2.38	1.12
10 second stand. dev.	0.77	0.42
Max mean	11.23	3.69
Max stand. dev.	1.55	1.58

6.5 Conclusions

The data presented in this chapter show that a wind sensing UAS can detect turbulence through simulation and TKE. Good agreement was also shown between the KHawk Thermal Vision UAS

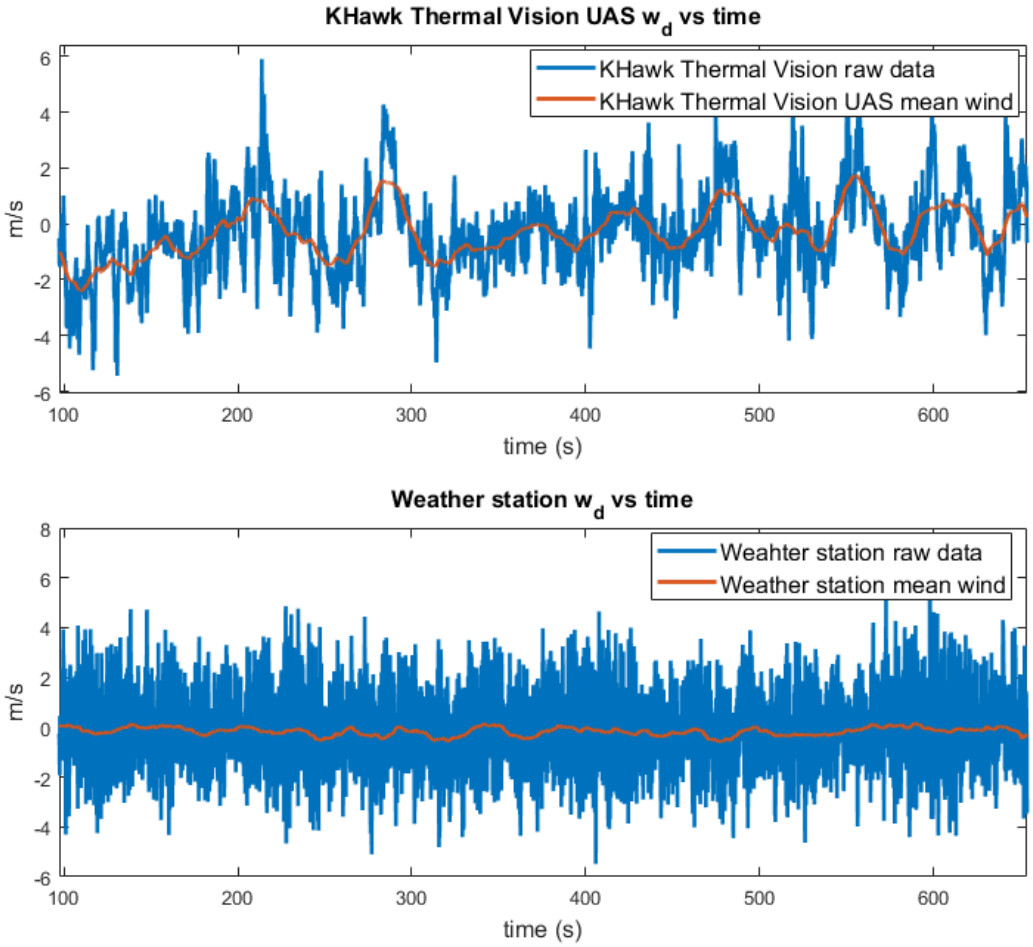

Figure 6.7: Raw data wind vs. mean wind during controlled burn flight.

Table 6.3: TKE values for weather station

Value	**Controlled Burn Flight** (m^2/s^2)	**Calm Flight** (m^2/s^2)
10 second mean	3.52	0.57
10 second stand. dev.	1.07	0.31
Max mean	18.77	2.56
Max stand. dev.	7.09	1.28

and weather station wind direction and wind magnitude for the controlled burn flight. The TKE was noticeable larger during the controlled burn flight in comparison to the calm flight, which could aid in on-board detection of turbulence while flying a wind sensing UAS through turbulent conditions. Further research should include more analysis of wind sensing data for flights with varying wind

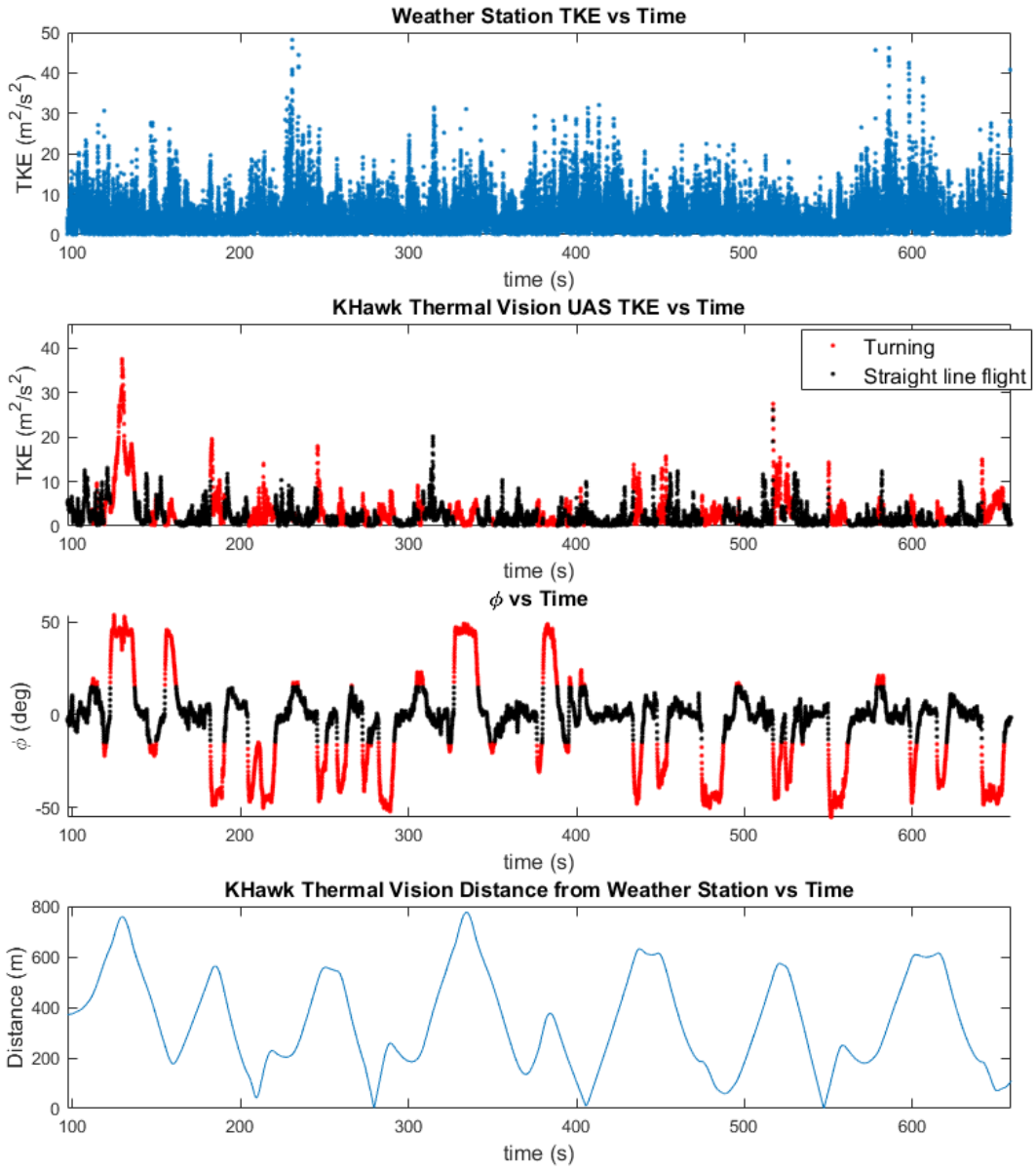

Figure 6.8: TKE vs time compared to roll angle and distance from weather station.

conditions (calm, windy, strong winds, and additional controlled burn flights) to better understand TKE variations based on weather conditions.

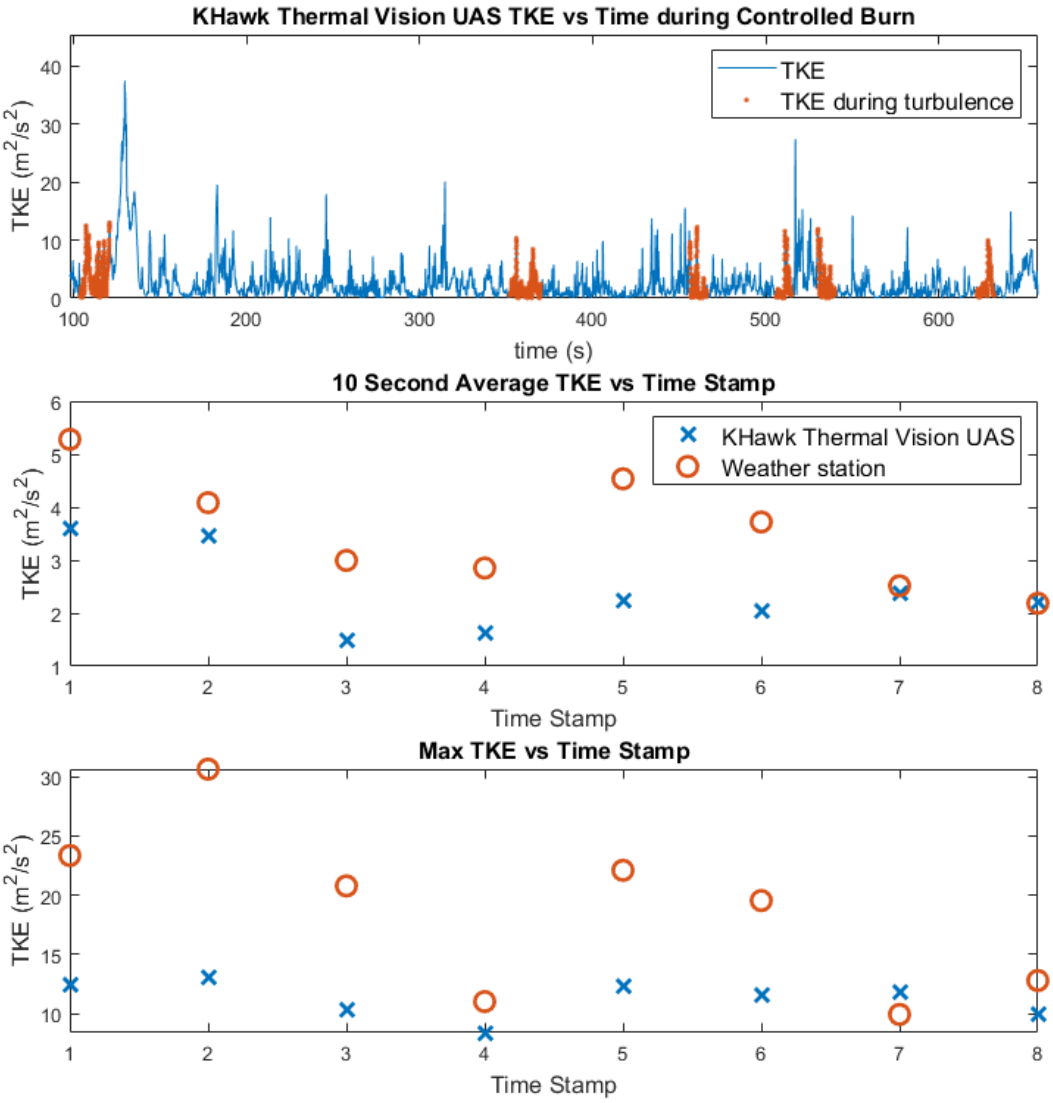

Figure 6.9: TKE vs time for 10 second intervals during the controlled burn flight (straight line flight).

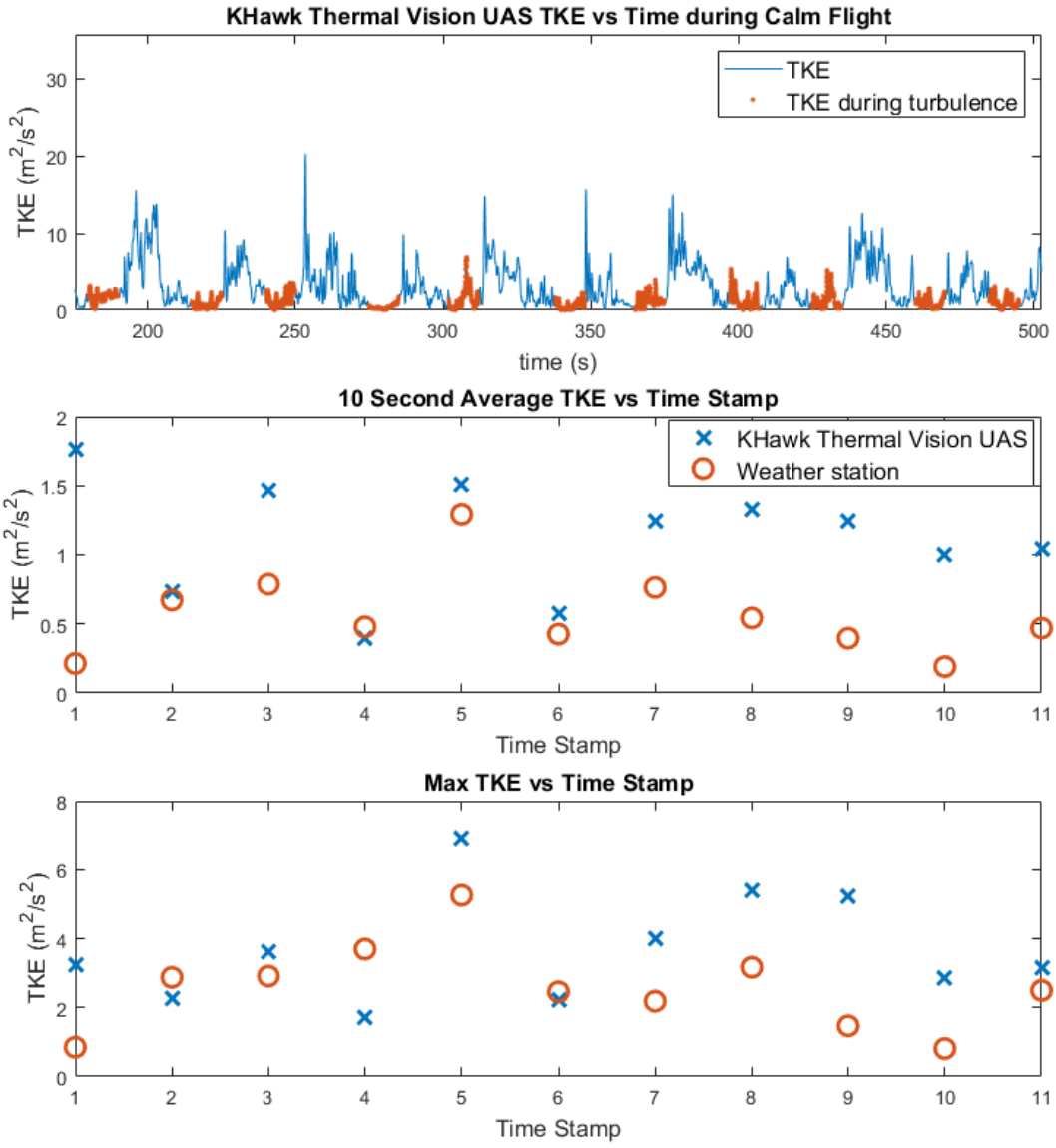

Figure 6.10: TKE vs time for 10 second intervals during the calm flight (straight line flight).

Chapter 7

Conclusions and Future Research Directions

7.1 Conclusions

In this dissertation, the KHawk UAS design, building, and testing procedure is first provided for a family of KHawk flying-wing UAS. The designed KHawk UAS show their effectiveness in different flight missions ranging from disaster remote sensing to aerodynamic research. A new coupled UAS system identification and flight controller design method is then proposed in Chapter 3 for the lateral loop of a typical flying-wing UAS. Good agreement between the dynamic model of the KHawk 55 UAS and the predicted controller specifications shows the success of the proposed method. The fractional order PID controller was further designed using a genetic algorithm for the purpose of robust controller design that can outperform a classical PID designed with the same genetic algorithm. The FOPID successfully outperformed the classical PID for turbulence rejection and allows for additional design space flexibility for controller design. Combining the integrated system identification and controller design method can provide researchers with an effective method for developing controllers for turbulence rejection. Furthermore, the complimentary filter provided accurate results for AOA estimation which can be used for the purpose of detecting stalls. In Chapter 6, measurements taken by the KHawk Thermal Vision UAS showed promising results for mean wind measurement and turbulence detection. Both the KHawk Thermal Vision UAS and weather station wind data showed similar trends in mean wind direction and TKE measurements. In summary, this dissertation provides new effective methods and algorithms for development of flying-wing UAS that can operate in challenging flow environments, including whole system design, robust roll tracking controller design, flow angle estimation, and turbulence detection.

7.2 Future Research Directions

Future research directions include:

- comprehensive simulation and flight investigations of controller specification range selection for other small UAS or for different wind conditions. Example specifications include gain margin, phase margin, cut-off frequency, etc.;
- flight test validation of the proposed FOPID controllers including roll tracking performance and comparison with conventional PID controller for turbulence rejection;
- implementation and integration of stall detection algorithm to open source flight controllers such as Pixhawk or Paparazzi autopilot for flight safety improvements;
- collection of more UAS data sets for fire turbulence encounter, and for potential estimation of UAS based Eddy dissipation rate (EDR).

Publications

Journals (first author)

- H. Flanagan, H. Chao, and YQ. Chen, "Lateral Fractional Order Controller Design and Tuning for a Flying-Wing UAS, " (in preparation).

- H. Flanagan, H. Chao, and J. Matt, "Coupled Lateral System Identification and Roll Controller Design for a Flying Wing UAS," (under review for Journal of Aircraft).

Journals (co-authored)

- P. Tian, H. Chao, H. Flanagan, S. Hagerott, and Y. Gu "Design and Evaluation of Flow Angle Estimation Filters," IEEE Transactions on Aerospace and Electronic Systems (TAES), vol. 55, issue. 1, pp. 371–383, Feb 2019.

- S. Gowravaram, H. Chao, A. Molthan, T. Zhao, P. Tian, H. Flanagan, L. Schultz, and J. Bell, Spectral Reflectance Estimation of UAS Multispectral Imagery Using Satellite Cross-Calibration Method, Photogrammetric Engineering & Remote Sensing (PE&RS), accepted, to appear 2021.

Conference (first author)

- H. Flanagan, H. Chao, and J. Matt, "Impact of Wind and Turbulence on a Small UAS while Flying through fire generated plumes,", Submitted under review, AIAA SCITech 2022.

- H. Flanagan, H. Chao, and YQ. Chen, "Lateral Fractional Order Controller Design and Tuning for a Flying-Wing UAS," International Conference on Unmanned Aerial Systems, Athens, Greece, Sep 2020.

- H. Flanagan, H. Chao, and S. Hagerott, “Model Based Roll Controller Tuning and Frequency Domain Analysis for a Flying-Wing UAS,” International Conference on Unmanned Aerial Systems, Atlanta, Georgia, USA, Jun 2019.

- H. Flanagan, H. Chao, and S. Hagerott, “Model Based Roll Controller Tuning and Analysis for Small UAS in Turbulence Environment,” International Conference on Unmanned Aerial Systems, Dallas, Texas, USA, Jun 2018.

Conference (co-author)

- S. Gowravaram, P. Tian, H. Flanagan, J. Goyer, and H. Chao, “UAS-based Multispectral Remote Sensing and NDVI Calculation for Post Disaster Assessment, ”International Conference on Unmanned Aerial Systems, Dallas, Texas, USA, Jun 2018.

- S. Gowravaram, H. Flanagan, P. Tian, and H. Chao, “Prescribed Fire Monitoring Using KHawk Unmanned Aircraft Systems,” AIAA Infotech Conference, Kissimmee, Florida, USA, Jan 2018.

- H. Chao, H. Flanagan, P. Tian, and S. Hagerott, “Flight Test Investigation of Stall/Spin Detection Techniques for a Flying Wing UAS,” AIAA Atmospheric Flight Mechanics Conference, Grapevine, Texas, USA, Jan 2017.

References

[1] S. Gowravaram, H. Chao, T. Zhao, S. Parson, X. Hu, M. Xin, H. Flanagan, and P. Tian, "Fire evolution mapping and rate of spread measurement using orthorectifed thermal imagery from a fixed-wing uas," *Sent to IJRS for review*, Sent 2021.

[2] H. Chao and Y. Chen, *Remote Sensing and Actuation Using Unmanned Vehicles*. Wiley IEEE Press, August 2012.

[3] H. Flanagan, *KHawk 55 Building Procedure*. CUSL, 2015.

[4] "Paparazzi UAV, wiki.paparazziuav.org/wiki/main_page," December 2018.

[5] "ArduPilot Dev Team, ardupilot.org/ardupilot/index.html," 2019.

[6] H. Chao, Y. Cao, and Y. Chen, "Autopilots for small unmanned aerial vehicles: a survey," *International Journal of Control, Automation, and Systems*, vol. 8, no. 1, pp. 36–44, 2010.

[7] W. R. Beard and T. W. McLain, *Small unmanned aircraft: Theory and practice*. Princeton university press, 2012.

[8] S. Gowravaram, H. Flanagan, P. Tian, and H. Chao, "Prescribed fire monitoring using KHawk unmanned aircraft system," AIAA, SciTech Forum, Kissimmee, Florida, 8-12 January, 2018.

[9] P. Bravo-Mosquera, L. Botero-Bolivar, D. Acevedo-Giraldo, and H. Ceron-Munoz, "Aerodynamic design analysis of a UAV for superficial research of volcanic environments," vol. 70, pp. 600–614, Aerospace Science and Technology, November 2017.

[10] A. Mohamed, R. Clothier, S. Watkins, R. Sabatini, and M. Abdulrahim, "Fixed-wing MAV attitude stability in atmospheric turbulence, part1: Suitability of conventional sensors," Progress in Aerospace Sciences, 3 July, 2014.

[11] A. Mohamed, S. Watkins, R. Clothier, M. Abdulrahim, K. Massey, and R. Sabatini, "Fixed-wing MAV attitude stability in atmospheric turbulence , part2: Investigating biologically-inspired sensors," Progress in Aerospace Sciences, 1 July, 2014.

[12] Anonymous, "Military standard, flying qualities of piloted airplanes," MIL-STD-1797B, April, 2012.

[13] D. H. Klyde, P. C. Shulze, D. G. Mitchell, and N. Alexandrov, "Development of a process to define unmanned aircraft system handling qualities," AIAA SciTech Forum, Kissimmee, Florida, 8-12 January, 2018.

[14] F. C. Sanders, M. Tischler, T. Berger, M. G. Berrios, and G. A, "System identification and multi-objective longitudinal control law design for a small fixed-wing UAV," AIAA Atmospheric Flight Mechanics Conference, January 2018.

[15] J. A. Holmberg, D. J. King, and J. R. Leonard, "Flying qualities specification and design standards for unmanned air vehicles," AIAA Atmospheric Flight Mechanics Conference and Exhibit, Honolulu, Hawaii, 18-21 August, 2008.

[16] T. M. Foster and W. J. Bowman, "Dynamic stability and handling qualities of small unmanned-aerial-vehicles," AIAA Aerospace Sciences Meeting and Exhibit, Reno, Nevada, 10-13 January 2005.

[17] A. Voß, "Open and closed loop gust loads analysis for a flying wing configuration with variable longitudinal stability," vol. 89, pp. 1–10, Aerospace Science and Technology, June 2019.

[18] M. B. Tischler, T. Berger, C. M. Ivler, M. H. Mansur, K. K. Cheung, and J. Y. Soong, *Practical Methods for Aircraft and Rotorcraft Flight Control Design, An Optimization-Based Approach*. AIAA Education Series, 2017.

[19] J. Roskam, *Airplane flight dynamics and automatic flight controls*. DARcorporation, 1995.

[20] B. L. Stevens, *Aircraft Control and Simulation*. Wiley-interscience, 2003.

[21] J. Matt, H. Flanagan, and H. Chao, "Evaluation and analysis of ardupilot automatic tuning algorithm for the roll tracking controller of a small uas," in *AIAA Scitech 2021 Forum*, 2021.

[22] R. Venkataraman and P. Seiler, "System identification for a small, rudderless, fixed-wing unmanned aircraft," vol. 56, pp. 1126–1134, Journal of Aircraft, May-June 2019.

[23] A. D. Dorobantu, A. Murch, B. Mettler, and G. Balas, "System identification for small, low-cost, fixed-wing unmanned aircraft," vol. 50, pp. 1117–1130, Journal of Aircraft, Jul-Aug 2013.

[24] S. Seher-Weiss and W. V. Gruenhagen, "Development of EC 135 turbulence models via system identification," vol. 23, pp. 43–52, Aerospace Science and Technology, December 2012.

[25] M. Tischler and R. K. Remple, *Aircraft and Rotorcraft System identification, Engineering Methods with Flight Test Examples*. AIAA Education Series, 2012.

[26] R. C. Nelson, *Flight Stability and Automatic Control*. WCB/McGraw-Hill, 1998.

[27] J. Etele, "Overview of wind gust modelling with application to autonomous low-level UAV control," Defence R&D Canada-Ottawa, Contract Report, November 2016.

[28] B. Etkin and L. D. Reid, *Dynamics of Flight, Stability and Control, Third Edition*. John Wiley & Sons, Inc, 1996.

[29] P. Woodrow, M. Tischler, G. Mendoza, S. G. Hagerott, and J. Hunter, "Low cost flight-test platform to demonstrate flight dynamics concepts using frequency-domain system identification methods," AIAA Atmospheric Flight Mechanics (AFM) Conference, 2013.

[30] CONDUIT, *CONtrol Designer's Unified InTerface*. Universities Space Research Association, Columbia, MD, 2016.

[31] P. Bravo-Mosquera, L. Botero-Bolivar, D. Acevedo-Giraldo, and H. Ceron-Munoz, "Aerodynamic design analysis of a UAV for superficial research of volcanic environments," *Aerospace Science and Technology*, vol. 70, pp. 600–614, 2017.

[32] "Ardupilot project." [https://ardupilot.org], 2020.

[33] C. Rice, Y. Gu, H. Chao, T. Larrabee, S. Gururajan, M. Napolitano, T. Mandal, and M. Rhudy, "Autonomous close formation flight control with fixed wing and quadrotor test beds," *International Journal of Aerospace Engineering*, vol. 2016, 2016.

[34] A. Mohamed, R. Clothier, S. Watkins, R. Sabatini, and M. Abdulrahim, "Fixed-wing MAV attitude stability in atmospheric turbulence, part1: Suitability of conventional sensors," *Progress in Aerospace Sciences*, vol. 70, pp. 69–82, 2014.

[35] A. Mohamed, S. Watkins, R. Clothier, M. Abdulrahim, K. Massey, and R. Sabatini, "Fixed-wing MAV attitude stability in atmospheric turbulence, part2: Investigating biologically-inspired sensors," *Progress in Aerospace Sciences*, vol. 71, pp. 1–13, 2014.

[36] H. Chao, Y. Luo, L. Di, and Y. Chen, "Roll-channel fractional order controller design for a small fexed-wing unmanned aerial vehicle," *Control Engineering Practice*, vol. 18, no. 7, pp. 761–772, 2010.

[37] J. Han, L. Di, C. Coopmans, and Y. Chen, "Fractional oder controller for pitch loop control of a VTOL UAV," in *Proceedings of the 2013 International Conference on Unmanned Aircraft Systems*, May 2013.

[38] P. Anatachaisilp, "Fractional order control of active magnetic bearing systems," Ph.D. Dissertation, University of Virginia, 2015.

[39] T. Berger, "Handling qualities requirements and control design for high-speed rotorcraft," Ph.D. Dissertation, Pennsylvania State University, 2019.

[40] T. Berger, C. Ivler, M. Berrios, M. Tischler, and D. Miller, "Disturbance rejection handling qualities criteria for rotorcraft," in *AHS 72nd Annual Forum*, 5 2016.

[41] C. Blanken, M. Tischler, J. Lusardi, and T. Berger, "Proposed revisions to aeronautical design

standard−33E (ADS−33E−PRF) toward ADS−33F−PRF," tech. rep., DEVCOM Aviation & Missile Center, U.S. Army, September 2019.

[42] H. P. Flanagan, S. G. Hagerott, and H. Chao, "Model based roll controller tuning and frequency domain analysis for a flying-wing UAS," in *Proceedings of the 2019 International Conference on Unmanned Aircraft Systems*, June 2019.

[43] A. Oustaloup, F. Levron, B. Mathieu, and F. M. Nanot, "Frequency band complex noninteger differentiator: Characterization and synthesis," *IEEE Transactions on Circuit and Systems - I, Fundamental Theory and Application*, vol. 14, no. 1, pp. 25–39, 2000.

[44] K. B. Oldham and J. Spanier, *The Fractional Calculus*. Academic Press, 1974.

[45] I. Podlubny, *Fractional Differential Equations*. Academic Press, 1999.

[46] A. Oustaloup, J. Sabatier, and P. Lanusse, "From fractal robustness to the crone control," *Fractional Calculus and Applied Analysis*, vol. 2, no. 1, pp. 1–30, 1999.

[47] H. P. Flanagan, S. G. Hagerott, and H. Chao, "Model based roll controller tuning and analysis for small UAS in turbulent environment," ICUAS Conference, 12-15, June 2018.

[48] MathWorks, *MATLAB 2019a*. Natick, Massachusets: MathWorks Inc, 2019.

[49] D. Xue, Y. Chen, and D. P. Atherton, *Linear Feedback Control, Analysis and Design with Matlab*. Advances in Design and Control SIAM, 2007.

[50] Aircraft Owner and Pilot Association (AOPA), "Stall/spin: Entry point for crash and burn," *AOPA Accident Analysis*, 2001.

[51] C. M. Belcastro and J. V. Foster, "Aircraft loss-of-control accident analysis," AIAA Guidance, Navigation, and Control Conference, 2013.

[52] A. M. Ragheb, O. D. Dantsker, and M. E. Selig, "Stall/spin flight testing with a subscale aerobatic aircraft," 31st AIAA Applied Aerodynamics Conference, 2013.

[53] R. A. Bunge, F. M. Savino, and I. M. Kroo, "Stall/spin flight test techniques with cots model aircraft and flight data systems," AIAA Atmospheric Flight Mechanics Conference, 2015.

[54] R. A. Bunge, F. M. Savino, and I. M. Kroo, "Approaches to automatic stall/spin detection based on small scale uav flight testing," AIAA Atmospheric Flight Mechanics Conference, 2015.

[55] B. L. Steven and F. L. Lewis, *Aircraft Control and Simulation*. Wiley-Interscience, 2013.

[56] P. Tian, H. Chao, Y. Gu, and H. S. G, "UAV flight test evaluation of fusion algorithms for estimation of angle of attack and sideslip angle," AIAA Guidance Navigation and Control Conference, 2016.

[57] E. A. Morelli, "Real-time aerodynamic parameter estimation without air flow angle measurements," *Journal of Aircraft*, vol. 49, no. 4, pp. 1064–1074, 2012.

[58] S. Gowravaram, P. Tian, H. Flanagan, P. Goyer, and H. Chao, "Uas-based multispectral remote sensing and ndvi calculation for post disaster assessment," International Conference on unmanned Aircraft Systems Dallas, Tx, 12-15 June, 2018.

[59] S. Gowravaram, H. Chao, H. Flanagan, and P. Tian, "Wildland fire monitoring and mapping using orthorectified near-infrared and thermal uas imagery," in *101th American Meteorological Society Annual Meeting, Special Symposium on Meteorological Observations and Instrumentation (Presentation)*, 2021.

[60] H. Flanagan, P. Tian, and H. Chao, "Wind and turbulence estimation during wildland fire using khawk fixed-wing uas," 101^th American Meteorological Society Annual Meeting, Special Symposium on Meteorological Observations and Instrumentation (Presentation), 2021.

[61] E. Beachly, C. Detweiler, S. Elbaum, D. Twidwell, and B. Duncan, "Uas-rx interface for mission planning, fire tracking, fire ignition, and real-time updating," AIAA Infotect at Aerospace Conference, AIAA Unmanned Unlimited Conference, Seattle, WA, 2015.

[62] D. Twidwell, C. R. Allen, C. Detweiler, J. Higgens, C. Laney, and E. Sebastian, "Smokey comes of age: unmanned aerial systems for fire management," *Frontiers in Ecology and the Environment*, vol. 14, no. 6, pp. 333–339, 2016.

[63] S. D. Roos, D. Turner, A. Lucieer, and D. M. J. S. Bowman, "Using digital surface models from uas imagery of fire damaged sphagnum peatlands for monitoring and hydrological restoration," *Drones*, vol. 2, no. 4, 2018.

[64] C. J. Moran, C. A. Seielstad, M. R. Cunningham, V. Hoff, R. A. Parsons, L. Queen, K. Sauerbrey, and T. Wallace, "Deriving fire behavior metrics from uas imagery," *Fire*, vol. 2, no. 2, June 22, 2019.

[65] L. Merino, F. Caballero, J. R. M. de dios, I. Maza, and A. Ollero, "An unmanned aircraft system for automatic forest fire monitoring and measurement," *Journal of Intelligent Robotic Systems*, vol. 65, no. 36, pp. 533–548, 2012.

[66] N. Homainejad and C. Rizos, "Application of multiple categories of unmanned aircraft systems (uas) in different airspaces for bushfire monitoring and response," in *International Conference on Unmanned Aerial Vehicles in Geomatics*, (Honolulu, HI), The International Archives of the Photogrammetry, Remote Sensing and Spatial Information Sciences, 2015.

[67] M. J. Brewer and C. B. Clements, "Meteorological profiling in the fire environment using uas," *Fire*, vol. 3, no. 36, 2020.

[68] B. Aydin, E. Selvi, J. Tao, and M. J. Starek, "Use of fire-extinguishing balls for a conceptual system of drone-assistedwildfire fighting," *Drones*, vol. 3, no. 17, 2019.

[69] M. J. Allen, *Guidance and Control of an Autonomous Soaring UAV*. NASA SP-255, 2007.

[70] D. J. Edwards, "Implementation details and flight test results of an autonomous soaring controller," in *AIAA Guidance, Navigation, and Control Conference*, (Honolulu, HI), AIAA, 2008.

[71] K. Andersson, I. Kaminer, K. Jones, V. Dobrokhodov, and D. J. Lee, "Cooperating uavs using thermal lift to extend endurance," in *AIAA Infotect at Aerospace Conference*, (Seattle, WA), AIAA Unmanned Unlimite4d Conference, 2015.

[72] K. Andersson, I. Kaminer, V. Dobrokhodov, and V. Cichella, "Thermal centering control for autonomous soaring: Stability analysis and flight test results," *Frontiers in Ecology and the Environment*, vol. 35, no. 3, pp. 963–975, 2012.

[73] P. Tian, *Sensing and Estimation of Airflow Angles and Atmospheric Winds for Small Unmanned Aerial Vehicles*. Ph.D. Dissertation, University of Kansas, 2020.

[74] L. R. Salazar, J. A. Cobano, and A. Ollero, "Small uas-based wind feature identification system part 1: Integration and validation," *Sensors*, vol. 17, no. 1, 2016.

[75] R. Calmer, G. C. Roberts, J. Preissler, K. J. Sanchez, S. Derrien, and C. O'Dowd, "Vertical wind velocity measurements using a five-hole probe with remotely piloted aircraft to study aerosol–cloud interactions," *Atmospheric Measurement Tech*, vol. 11, no. 5, pp. 2583–2599, 2018.

[76] S. B. Pope, *Turbulent Flows*. Cambridge University Press, 2000.

[77] E. O. Akinlabi, M. Waclawcyyx, J. P. Mellado, and S. P. Malinowski, "Estimating turbulence kinetic energy dissipation rates in the numerically simulated stratocumulus cloud-top mixing layer: Evaluation of different methods," *American Meteorological Society*, vol. 76, no. 5, pp. 1471–1488, 2019.

[78] H. Pitsch, "Turbulence, cefrc combustion summer school," RWTH Aachen University, 2014.

[79] M. Savli, "Turbulence intensity and turbulent kinetic energy (tke)," University of Ljubljana, 2012.